

ABSTRACT

Title of dissertation: MAGNETOHYDRODYNAMIC SIMULATIONS OF
BLACK HOLE ACCRETION

Mark J. Avara, Doctor of Philosophy, 2017

Dissertation directed by: Professors Jonathan McKinney and
Christopher S. Reynolds
University of Maryland, College Park

Black holes embody one of the few, simple, solutions to the Einstein field equations that describe our modern understanding of gravitation. In isolation they are small, dark, and elusive. However, when a gas cloud or star wanders too close, they light up our universe in a way no other cosmic object can. The processes of magnetohydrodynamics which describe the accretion inflow and outflows of plasma around black holes are highly coupled and nonlinear and so require numerical experiments for elucidation. These processes are at the heart of astrophysics since black holes, once they somehow reach super-massive status, influence the evolution of the largest structures in the universe. It has been my goal, with the body of work comprising this thesis, to explore the ways in which the influence of black holes on their surroundings differs from the predictions of standard accretion models. I have especially focused on how magnetization of the greater black hole environment can impact accretion systems.

MAGNETOHYDRODYNAMIC SIMULATIONS OF BLACK HOLE ACCRETION

by

Mark J. Avara

Dissertation submitted to the Faculty of the Graduate School of the
University of Maryland, College Park in partial fulfillment
of the requirements for the degree of
Doctor of Philosophy
2017

Advisory Committee:

Professor Jonathan McKinney, Advisor

Professor Christopher Reynolds, Chair

Professor David Levermore

Professor M. Coleman Miller

Professor Richard Mushotzky

Dr. Jeremy Schnittman

© Copyright by
Mark James Avara
2017

Preface

The body of this thesis contained in Chapters 2-5 are comprised of four papers I have written or substantially contributed to. Chapter 2 is published as [Avara, McKinney, and Reynolds \(2016\)](#) and I carried out the writing of the paper and the bulk of all work entailed in the research presented.

Chapter 3 is Morales, McKinney, and Avara (2017), currently in preparation for submission to Monthly Notices of the Royal Astronomical Society. While I will not be first author on that paper, the version presented in this thesis is presented in predominately my own words, and I have contributed substantially to the analysis. Many of the interpretations presented here are my own contribution, and I made all of the figures aside from Fig. 3.4.

Chapter 4 is published as [McKinney, Dai, and Avara \(2015b\)](#). The paper is included here in its published form, with only minor revisions. I aided in the interpretation of the results of this work and made some contributions to the written text.

Chapter 5 is published as [Avara, Reynolds, and Bogdanović \(2013\)](#). I carried out the writing of the paper and the bulk of all work entailed in this research as well, under the supervision of Prof. Christopher Reynolds with assistance by Dr. Tamara Bogdanović.

Dedication

For my parents, to whom I owe opportunity, support, and my thirst for knowledge.

‘I may not always have the answer, but I know where to look to find it.’

- James E. Avara

Acknowledgments

Without the generous support of many, I would not have reached my goal of obtaining a doctorate degree in astrophysics. The tireless dedication of my parents and many talented teachers, and the support and strength of friends and loved ones has been essential, and I am eternally grateful.

I would like to specifically thank some of the teachers that helped me achieve important milestones without which I would not have gotten here: Mrs. Allen, who brought joy to mathematics and learning in general, Mr. Wightman, who's portrayal of history and literature made me a better writer and deeper thinker, and who's recommendation help get me into TAMS. At TAMS I owe a growing appreciation and understanding of mathematics and the sciences to Neal Brand and Paul Braterman, especially, though many others had an impact on my scientific understanding as well. At MIT I thank those tireless in the art of teaching and physics, especially Max Tegmark, Peter Dourmashkin, and David Kaiser. It is there that I first learned what scientific research entails under the instruction of Herman Marshall.

Without the opportunity of attending graduate school at UMD this thesis would never have come to pass, and for that opportunity I thank those on the admissions committee, especially Lee Mundy, and those scientists who recommended me, including Belinda Wilkes, who generously offered me a place in her group when I was trying to get into a good graduate program.

It is at UMD that I have grown mature as a scientist, though there is still a long road ahead. I have been lucky to work under the wise tutelage of Christopher Reynolds and Jonathan McKinney. Working with two scientists of such depth of understanding and appreciation for their work has been a worthwhile challenge, and a true pleasure.

These are the shoulders I stand on, and I hope to make a contribution to science worthy of the time and devotion of those who have trained me.

I would also like to thank Manuela Campanelli for offering me an opportunity to continue research at RIT as a post-doc, and for being flexible during a difficult

time.

Finally, I especially owe so much to my parents. JoAnn Avara and James E. Avara helped me find my path, time after time, with support and love beyond what I could have asked for. I wish he'd grown up with the opportunities I've been given, but in place of that, both my parents, have helped me achieve my dreams.

Table of Contents

List of Tables	viii
List of Figures	ix
List of Abbreviations	xvii
1 Background and Motivation	1
1.1 Accretion in astrophysics	1
1.1.1 Observations of AGN and XRBs	3
1.1.2 Geometrically thin, radiatively efficient accretion	9
1.2 Magnetic fields in disks	11
1.2.1 Magnetorotational instability	12
1.2.2 Magnetic topology and field strength	14
1.3 Numerical methods	16
1.3.1 Finite volume approach	16
1.3.2 HARM	18
1.3.3 Radiative GRMHD	20
1.4 Outline - Description of chapters	21
2 Efficiency of Thin MADs	23
2.1 Introduction	23
2.2 Fully 3D GRMHD Thin MAD Model	25
2.2.1 Physical Model	26
2.2.2 Numerical Grid and Density Floors	31
2.2.3 Cooling	32
2.2.4 Diagnostics	33
2.3 Results and Discussion	36
2.3.1 Demonstration of flux accumulation to MAD state	41
2.3.2 Long-term evolution of MAD state	42
2.3.3 Radiative Efficiency	45
2.3.4 Jet Efficiency	46
2.3.5 Resolution	51

2.3.6	Power-law Fits for Radial Dependence	54
2.4	Summary and Conclusions	57
3	3D GRRMHD Simulations of a Thin Accretion Disk in the MAD state	59
3.1	Introduction	60
3.2	3D GRRMHD thin disk model	62
3.2.1	Numerical grid	64
3.2.2	Diagnostics	67
3.3	Results	68
3.3.1	Accretion rate	69
3.3.2	Scale Height	73
3.3.3	Efficiencies	74
3.3.4	Magnetic flux	75
3.3.5	Luminosities	76
3.3.6	Resolution effects	79
3.4	Discussion and Conclusions	81
4	Efficiency of Super-Eddington MADs	83
4.1	Introduction	83
4.2	Fully 3D GR Radiative MHD MAD Model	85
4.2.1	Opacities	85
4.2.2	Initial Conditions	87
4.2.3	Numerical Grid and Density Floors	88
4.2.4	Diagnostics	89
4.3	Results and Discussion	90
4.4	Summary	97
5	Role of Magnetic Field Strength and Numerical Resolution in Simulations of the Heat-flux Driven Buoyancy Instability	99
5.1	Introduction	100
5.2	MHD of Weakly Magnetized Plasmas	102
5.2.1	Background Equilibrium Conditions	104
5.2.2	Stability analysis	104
5.3	Numerical Setup	106
5.4	Plasma Behavior as a Function of Resolution and β	108
5.4.1	Plasma β	108
5.4.2	Grid Resolution	114
5.5	Dynamics and Persistence of Filaments	115
5.6	3-D Simulation	121
5.7	Discussion and Conclusions	122
6	Conclusions and a look forward	126

List of Tables

3.1	Grid resolution	64
3.2	Polar grid Parameters	67

List of Figures

1.1	This figure reproduced from Remillard and McClintock (2006) shows in red dots the instantaneous measure of hardness and luminosity of a hypothetical LMXRB. The disk spends most of its time in the quiescent state on the lower right corner. During an outburst it goes through disk states i-iv . The diagrams around the plot show the dominate components of the accretion/jet inflow/outflow during each accretion state.	7
2.1	Snapshots of the initially sub-MAD (MADfHR - left panel) and nearly-MAD (MADiHR - right panel) models at $t=0$, showing ρ in color (with legend) with magnetic field lines (black lines). In MADfHR there is no magnetic field initially present within the ISCO or on the horizon and the field is weak throughtout the disk. On the other hand, in MADiHR, a sufficient magnetic flux is present throughout the disk and on the horizon so that the disk will quickly become MAD out to large radius. The higher density surrounding the horizon in MADiHR at $t=0$ is the result of the density floor activated due to the presence of an initially strong magnetic field.	26
2.2	(Caption on next page.)	27

2.2	(Previous page.) Evolved snapshot of the MADfHR model at $t \approx 70,000r_g/c$ showing log of rest-mass density in color (with legend) in both the $z-x$ plane at $y=0$ (top-left panel) and $y-x$ plane at $z=0$ (top-right panel). Black lines with arrows trace field lines, where thicker black lines show where field is lightly mass-loaded. The bottom panel has 3 subpanels. The top subpanel shows the mass accretion rate through the BH (\dot{M}_H). The middle subpanel shows the magnetic flux threading the BH (Υ_H), normalized so that order unity is a dynamically-substantial amount of magnetic flux. The bottom subpanel shows the gas efficiency measured on the horizon ($\eta_{H,g}$) and jet efficiency measured at $r=50r_g$ (η_j). In this model, the disk initially has a weak large-scale poloidal magnetic field, which is transported by the MRI and other magnetic stresses toward the BH. Eventually, by $t \sim 55000r_g/c$, the magnetic flux saturates on the BH and cannot grow despite plentiful magnetic flux outside. The MAD state that develops consists of a highly non-axisymmetric clumpy thin disk with a weak ($\eta_j \sim 1\%$) jet.	28
2.3	(Previous page.) Plotted from left to right are snapshots from MADfHR at $t=[0,10000,16320,40000]r_g/c$. Black contours (with a single colored white) trace the same values on all snapshots and show the ϕ -averaged magnetic field. The contours demonstrate the transport of magnetic flux radially toward the horizon. All magnetic flux is initially threading the disk only, then accretes most rapidly through coronal processes along the surface of the disks where it piles up at these latitudes before it does in the mid-plane of the accretion flow. Reconnection near the horizon where the disk is very thin leads to magnetic loops (seen in middle panel) in the inner disk out to $\sim 20r_g$, where further reconnection and decoupling from the magnetically driven wind cause a drop in the effective disk viscosity. Ultimately the magnetic loops are also accreted and some flux originally threading the disk then threads only the horizon.	29
2.4	(Caption on next page.)	37

2.4	(Figure on previous page.) Time and ϕ -averaged quantities are plotted for MADfHR. The time average is taken over 55000-68000 r_g/c , during which time the horizon has reached a MAD saturation of flux. Rest mass gas flow is traced by black streamlines. The colored (green and blue) thick lines correspond to time-averages of quantities $Y = \{u^r, b^2/\rho\}$, respectively, at values $[Y]_t = \{0, 1\}$. While near the BH the flow has $[b^2/\rho]_t \gtrsim 1$ as averaged directly, the dense inflow has $[b^2/\rho]_t \lesssim 1$ at all other radii. The time and spatial variability of the jet causes the time- ϕ average to blend jet and disk material, so the average $[b^2/\rho]_t \gtrsim 1$ bleeds into the disk. Similarly, $[b^2]_t/[\rho]_t$ identifies a jet boundary in the opposite way, causing too much of the polar/jet region to appear to have $[b^2/\rho]_t \lesssim 1$. No particular average is correct, but our choice includes the part of the wind and disk that experiences extra acceleration through interaction with the jet. Streamlines nearest the polar axes are calculated using velocity structure five cells away from the axis for better visualization of the qualitative geometry of the jet flow. The flow exhibits equatorial asymmetry over many inflow times as found in thicker MAD simulations, likely a result of bulk flows associated with the very initial evolution of the disk. The red magnetic field line contours show how the magnetic flux threads the black hole and inner disk.	38
2.5	Time (from 30000-70000 r_g/c) and ϕ -averaged quantities are plotted for MADiHR. Identical layout as Fig. 2.4. The disk is magnetically arrested out to a transition radius of $\sim 35r_g$, which leads to a short inflow time-scale compared to the MADfHR disk at those radii, so the time-averaged velocity fields and other disk structure is smoother and more symmetric.	39
2.6	Evolved snapshot of the MADiHR model at $t \approx 70,000r_g/c$, with identical layout to Fig. 2.2. The MAD state is highly non-axisymmetric and clumpy with a weak ($\eta_j \sim 1\%$) jet. The rest-mass accretion rate and magnetic flux on the horizon reach the MAD state quickly, which was as desired so that we can study a quasi-steady MAD out to large radii over long time periods. The dimensionless magnetic flux Υ_H on the horizon is in agreement with our MADfHR model, showing a disk initial condition with a relatively stronger poloidal field strength still reaches the same MAD state near the BH.	40
2.7	(Caption on next page.)	43

- 2.7 (Figure on previous page.) Time-averaged quantities, averaged over $10000-70000r_g/c$, as a function of radius. From top to bottom, panels are: Total mass accretion rate (\dot{M}_0 , blue line), energy efficiency (η), specific angular momentum (j), magnetic flux (Ψ), and disk thickness (H/R , $n=1$ in Eq. 2.4, blue line). Plots for η and j show total gas+radiative (black solid), electromagnetic (green), matter (red), and radiation (black dashed) components. Remaining plots show their initial value (magenta dot-dash). The plot of Ψ shows the cumulative net vertical flux including BH and disk contributions (blue). The constancy of \dot{M} , η , j show where the flow has achieved inflow equilibrium. Ψ shows the MAD to non-MAD transition at $r \sim 35r_g$, while throughout the disk $H/R \approx 0.1$ (bound gas), as maintained by cooling. The primary result of this plot is the efficiency panel showing the radiative contribution of $\eta_r \sim 15\%$ with most of emission beyond the standard NT disk model coming from quite close to the photon orbit where the MAD state differs significantly in structure and behavior from the NT disk. 44
- 2.8 Shows temporal evolution of a few quantities for our MADiHR model. The disk scale height H/R is shown in the top panel. We show the temporally-smoothed H/R as plotted for radii R_{ISCO} (solid-black), $15r_g$ (short-dashed), $30r_g$ (dots), and $60r_g$ (long-dashed). The red line is the un-smoothed evolution at $15r_g$ to demonstrate the level of variability. The H/R value is regulated by cooling to be $H/R \sim 0.1$, which is what is achieved for radii just outside the ISCO and out to the inflow equilibrium radius of $r \sim 35r_g$. The middle panel shows the α_b viscosity parameter spatially-averaged over the disk at a radius $10r_g$. The relatively high $\alpha_b \sim 0.5$ is indicative of MADs, implying efficient transport of mass and angular momentum. The third panel shows the ratio of the total magnetic flux threading the BH to the total magnetic flux available at the start of the simulation inside the radius out to which the simulation ultimately reaches at least one inflow time. This shows that the horizon retains only a fraction of the flux available during the course of the simulation, so the quasi-steady state has a horizon-threading flux that has reached saturation. 47
- 2.9 Shows temporal evolution of same quantities as Figure 2.8 for our MADfHR model. The disk scale height H/R is shown in the top panel. We show the temporally-smoothed H/R as plotted for radii R_{ISCO} (solid-black), $15r_g$ (short-dashed), $30r_g$ (dots), and $60r_g$ (long-dashed). The red line is the un-smoothed evolution at $10r_g$ to demonstrate the level of variability and show the evolution of the under-resolved dense torus present at early times. $\alpha_b \sim 0.5$ averaged around $8r_g$ drops to low values during that time as expected. 48

2.10	Plotted as in the top frames of Fig. 2.6 is a snapshot of MADiHR at $t = 31568r_g/c$ when the disk experiences an extreme eruption of magnetic flux from the BH horizon. A large magnetic flux tube creates a low-density cavity in the disk before it is partially blended with disk material by the magnetic Rayleigh-Taylor instability. Such prominences occur frequently in the MAD state.	52
2.11	MRI quality factors indicating time- ϕ averaged resolution, viscosity of the disk, and vertical MRI half-wavelengths per disk scale height (S_d , blue line) are plotted as a function of radius. Q factors indicated the number of grid cells per critical MRI wavelength, averaged with weight $\sqrt{\rho b^2}$ (solid lines) and ρ (short dashed) across the disk where $b^2/\rho < 0.5$. The third panel shows the viscosity parameter α_b (solid line) and the effective viscosity calculated via the mass accretion rate (short dashed). The magnetic evolution of the disk is well resolved and leads to a high viscosity as measured by local stresses, α_b , and the rate of mass inflow $\alpha_{b,\text{eff}}$. The magenta dot-dash line represents the value of S_d at $t=0$ and the time-average is blue-solid.	55
2.12	Several quantities characterizing the accretion flow in MADiHR are plotted as a function of radius. The top panel shows the density profile ρ (solid), the internal gas energy u_g (dashed), and magnetic energy density u_b (dotted). The inner disk, that has reached the MAD state, has $u_g \sim u_b$ indicating equipartition is achieved even within the dense parts of the disk. The middle panel includes the disk radial velocity, azimuthal velocity, and Keplerian velocity (v_r , solid; v_ϕ , black-dashed; v_K , blue-dashed, respectively). The final panel shows the radial profiles of each component of the comoving magnetic field, $b_{r,\theta,\phi}$, in solid, dashed, and dotted lines respectively. The density is shallower than thicker disk solutions, the disk is fairly Keplerian, and the magnetic field falls off as expected for accretion disks.	56
3.1	Snapshot of our simulation RADHR at the time $t=40.000R_g/c$ where the top two panels represents the $X - Z$ at $y=0$ and $X - Y$ at $z = 0$ slices of the density with the red line showing where $b^2/\rho=1$ and the black lines with arrows trace field lines where thicker black lines show where field is lightly mass loaded. The top sub-panel shows the mass accretion rate at the horizon (red line) and the luminosity (green line). The middle sub-panel shows the magnetic flux in the horizon normalized so that order unity is a dynamically substantial amount of magnetic flux. The bottom sub-panels shows the accretion efficiencies in the horizon (red line), jet efficiency (green line) measured at $15R_g$ and radiation (blue line) measure at $50R_g$	70
3.2	(Caption on next page.)	71

3.2	(Figure on previous page.) Characteristic quantities as a function of radius, time-averaged over the period $t = [30,000-40,000]R_g/c$ for the simulation RADHR. Panels consecutively show, from top to bottom: the mass accretion rate (\dot{M}), energy efficiencies (η) for different parts of the stress-energy tensor, magnetic flux (Ψ), disk scale-height (H/R), and S_d . In efficiencies plot the black line corresponds to the total gas+radiative (black line), electromagnetic (green line), matter (red) and radiation (black dashed) components. The magenta lines in the plots of Ψ , H/R , and S_d correspond to their initial values. The thick lines show values for RADHR and the thin line MADiHR from (Avara et al., 2016) time-averaged as in that paper.	72
3.3	Red is for RADLR, black for RADHR. Top panel: Disk scale-height as function of time. The solid line corresponds to the values for $10R_g$ (lines for all radii are smoothed, with only the $10R_g$ line duplicated without smoothing in gray), the dotted and dashed lines correspond to the values of H/R at the horizon and $20R_g$ respectively. Middle: Magnetic α measured at $10R_g$ (full, un-smoothed RADHR data in gray). Bottom: Amount of magnetic flux on the horizon normalized by the amount of magnetic flux contained in the portion of the disk which reaches one inflow time by the end of the simulation, i.e. the total magnetic flux available for the inner disk and horizon.	77
3.4	Top: Electromagnetic luminosity per unit angle $(\partial_\theta L_{EM})/(\dot{M}_H c^2)$ with time- ϕ averaged magnetic flux (translucent gray lines); blue lines show the $b^2/\rho=1$ boundary; the green line shows the $u^r=0$ boundary; yellow is the surface where optical depth reaches unity to electron scattering, integrating inward from a large, but at least moderately evolved, radius. Bottom: lab-frame radiation flux and radiation luminosity.	78
3.5	Plot showing the efficiencies for the simulation RADHR (dot-dashed line), RADvHR (dashed line), RADLR (dotted line) and MADiHR (continuous line). Black: total, Red: PAKE, Green: EM, Cyan: Radiation.	79
4.1	The initial ($t = 0$) state consists of a weakly magnetized radially-extended vertically-Gaussian disk with $H/R \sim 0.2$ around a spinning ($a/M = 0.8$) BH. Rest-mass density is shown as color with legend, while green lines show magnetic field lines. Density values are made dimensionless using \dot{M}_{Edd} , length r_g , and time r_g/c . The initial disk is threaded by weak (but ordered) magnetic flux, capable of accumulating onto the BH and leading to the MAD state.	91

4.2	The evolved ($t = 31, 200r_g/c$) super-Eddington MAD state, with the figure split at $x = 0$ as two panels ($x < 0$ on left and $x > 0$ on right). Left panel shows radiation-frame radiation energy density (color, with legend), radiation velocity lines (black, fixed line width), and optical depth of unity away from each polar axis, $\tau_\theta = 1$ (cyan lines). Right panel shows fluid-frame rest-mass density (color, same legend), magnetic field lines (black, thicker lines for more magnetized gas), where magnetic energy is equal to rest-mass energy density (red lines), and same optical depth (cyan lines). The MAD state reaches a quasi-steady state out to $r \sim 20r_g$. Radiation advects inward within the equatorial disk, outward through the low-density jet channel, and outward along with the optically thick wind.	92
4.3	The time-averaged angle-integrated mass flux, efficiency, disk thickness, and magnetic flux. From top to bottom, panels are: Total mass accretion rate (\dot{M}_0) per unit \dot{M}_{Edd} out to where there is inflow and thermal equilibrium ($r \sim 20r_g$, beyond which the line is truncated), energy efficiency η (total: solid black line, electromagnetic: blue dashed, matter without rest-mass (i.e. kinetic+gravitational+thermal): dark red dotted, radiation (negative within $3r_g$): red long-dashed, radiative luminosity L : magenta dot-dashed), disk thickness H/R (evolved state: black solid, initial state: blue dashed), and magnetic flux (total on BH and threading disk: black solid, only threading disk: dark red dotted). The disk is magnetically compressed near the BH, and the thin disk generates a significant radiative flux that effectively releases starting at $r \sim 300r_g$. The initial disk with $H/R \approx 0.2$ has puffed up to $H/R \approx 0.3$ from $r \sim 20\text{--}70r_g$ after evolving for several thermal times. By $r \sim 400r_g$, the luminosity reaches $L \sim 50L_{\text{Edd}}$	93
4.4	The evolved ($t = 31, 200r_g/c$) super-Eddington MAD state at large radii showing the jet, wind, and photosphere. Shows fluid-frame rest-mass density (color, with legend), where magnetic energy equal to rest-mass energy density (red lines), radiative photosphere at $\tau_r = 1$ (black line), and the wide-angle wind component's magnetic field line, within which (toward the polar axis) the outflow has achieved more than a single flow time along the line extending $\sim 1000r_g$ (blue line). Quantities are ϕ -averaged. The jet extends to $r \sim 30,000r_g$ with Lorentz factor $\gamma \sim 5$ by $r \sim 10^3r_g$. The wind extends to $r \sim 3000r_g$, with most of the wind's trapped radiation having an opening angle of 30° at $r \sim 400r_g$. The disk at $R \gg 100r_g$ has not evolved much. Radiation within $r \lesssim 400r_g$ can more freely stream within the jet's low-density channel. By $t \sim 30,000r_g/c$, at $r \sim 400r_g$ within 15° around the polar axis, the outflow become conical and optically thin.	95
5.1	H2d128_7 and H2d128_9 at four times (in units of dynamical times, ω_{dyn}^{-1})	109
5.2	Horizontally averaged vertical heat flux as a function of time.	110

5.3	The contribution to kinetic energy from vertical motion spatially averaged across the entire anisotropically conducting region is shown as a function of time.	112
5.4	Evolution of energy components.	113
5.5	Horizontally averaged vertical heat flux plotted in the $\beta \sim 10^7$ column of Fig. 5.2 versus time in dynamical units.	115
5.6	H2d512_5 (upper) and H2d512_7 (lower) filaments. Stability of the filaments is demonstrated by plotting the three stability diagnostics of Eqn. (5.19) measured for each filament.	117
5.7	Black contours (dash-dot) represent filaments from H2d128_7PS; red (solid) represent those from H2d128_7. Contour levels are set the same as in Fig. 5.6.	118
5.8	A frame from the saturated state of H3d128_7PS.	122
5.9	Vertical Heat Flux integrated over the horizontal plane slicing through the center of the active domain in H3d128_7PS.	123

List of Abbreviations

BH	Black hole
MHD	Magnetohydrodynamics
GRRMHD	General relativistic - Radiation - MHD
AGN	Active galactic nucleus
XRB	X-ray binary
MRI	Magneto-rotational instability
HBI	Heat-flux driven buoyancy instability

Chapter 1: Background and Motivation

1.1 Accretion in astrophysics

Astrophysics, as a mature field of science, truly encompasses the full breadth of physical law, from quantum theory to the extremes of gravitation. It generously provides environments inaccessible in the laboratory but necessary in order to test many modern physical theories, and discover new ones. Although much about the formation and behavior of galaxies, stars, planets, and even black holes can be understood through the complex coupling of predominantly known laws of physics, it is by seeking an understanding of that complexity that we hope to use astronomical observations to gain knowledge of new physical theories.

Accretion is the process a gravitationally self-bound object undergoes, whether it be a gas cloud, a star, a galaxy, a large-scale cosmological structure, or other object, as it accumulates more mass by gravitational attraction of the gas, or plasma if it has become ionized. The accumulating mass generally carries with it angular momentum leading to rotation as it contracts toward the central accretor.

There are two fundamental modes of accretion, separated by whether the specific angular momentum of the accreting matter (the matter can be composed of dust grains, molecules, a mixture of elements or ionization fractions, etc., but will hereon be referred to simply as ‘gas’) defines a plunging or a circulating orbit. Neglecting gas pressure forces, etc., for sufficiently high angular momentum, matter in an accretion inflow will reach a minimum radius where the centrifugal force equals the gravitational attractive force before reaching the surface of the central mass. A gas flow with this specific angular momentum or more is thus centrifugally choked, and as gas streams on different crossing orbits interact they form a disk.

On the other hand, the lower angular momentum case describes Bondi accretion (Bondi, 1952), the zero angular momentum limit of which provides the simplest model for accretion of gas onto a point-like gravitating object. The Bondi accretion rate onto the central object, \dot{M} only depends on the mass of the central object and the sound speed of the surrounding gas reservoir, and is determined by a critical point condition. Because of the simplicity of the Bondi model for accretion from homogeneous and rotationally invariant non-self gravitating gas, it is widely used to estimate the growth rate of gravitationally bound structures, such as supermassive BHs (Sakurai et al., 2016; Inayoshi et al., 2016), below the resolving power of simulations of galaxies and stars.

The disadvantage of the Bondi model, especially in its application to compact objects like black holes and neutron stars, where the mass to surface radius ratio is very high, is that most of these systems in the universe are accreting gas with significant angular momentum. Therefore for accretion to occur, the system must transport angular momentum away from the gas. Any process that transports the angular momentum outward dissipates energy and the mode of accretion thereby branches again depending on whether the accreting gas is efficient or inefficient at radiating the released energy. The outward transport of angular momentum and the energy released by that process give rise to a variety of theoretical models of accretion which we believe apply to the zoo of seemingly different accreting systems astronomers observe. A second limitation of the Bondi model is that it fails to take into account radiative transport (McKinney et al., 2014).

The total energy liberated as matter falls from an effectively infinite radius to the central object is often written as a conversion of mass flux to energy flux

$$L = \eta \dot{M} c^2. \quad (1.1)$$

The power of stars originates from the fusion of hydrogen into helium, a process with $\eta \approx 0.007$. In contrast, as I will describe below, a maximally rotating accreting black hole (BH) can reach $\eta \approx 40\%$ even using classical accretion models! This extreme efficiency in liberating gravitational potential energy makes some accreting

BHs the most luminous objects in the universe in electromagnetic radiation.

With the advent of X-ray telescopes in the 1960's, the discovery of many highly energetic and luminous astronomical objects summoned a renewed interest in astrophysical manifestations of extreme solutions to Einstein's field equations. Because of their compact nature, non-rotating (Schwarzschild, 1916) and rotating (Kerr and Schild, 1965; see also Kerr and Schild, 2009) BHs, time-independent solutions to the field equations, can host a disk reaching far enough into the gravitational potential that the opportunity for conversion of gravitational potential energy to other forms is maximized. Accreting black holes, due to their high luminosity and compact extent (most energy is liberated close to the BH), are an obvious choice to explain the high efficiency of the unresolved massive objects in active galactic nuclei (AGN) and X-ray binaries (XRBs).

1.1.1 Observations of AGN and XRBs

The most luminous AGN are historically referred to as quasars, or quasi-stellar-objects. Seyfert (1943) was the first to characterize galaxies that contained stellar-like cores using their optical spectra, and soon after the detection of Seyfert galaxies NGC 1068 and NGC 1275 as radio sources in 1955, Woltjer (1959) tried to understand the physics of these unusual galactic centers. He used virial arguments to infer large central masses and constrained the unresolved nuclei to less than 100pc. Thus something was required to release a huge amount of energy in a tiny volume. It did not take long before BHs were suggested as the central accretor (e.g., Zeldovich, 1964).

Accreting supermassive BHs (SMBH), i.e., $> 10^6$ solar masses (M_\odot), are now believed to lie in the center of nearly all galaxies at low redshift. A major argument for this is that of Soltan (1982). Even assuming a moderate radiative efficiency of accretion of %10, the observed characteristics of typical quasars leads to a simple argument for the average accreted central mass per galaxy (for those on the bright end of the galaxy luminosity function, i.e., those capable of supporting a massive central object) of greater than $10^7 M_\odot$.

These massive AGN exhibit a continuum of emission across the electromagnetic spectrum, from radio to γ -rays (Peterson 1997). Observations of AGN across these wavelengths has led to unified models centered around the principle of accretion onto a central SMBH, where the variety of AGN spectra and morphologies observed are determined by only a few simple parameters. The first unified model centered around inclination of the disk to the line of sight, and a more modern picture typically includes spin of the central BH and the mass accretion rate. These newer additions to the unified model, including the most recent, large-scale magnetic field presence in the galactic environment of the AGN, couple the BH more to the history of accretion and the effective boundary condition that is the hosting galactic environment.

The mass accretion rate onto BHs is typically scaled by the so-called Eddington rate,

$$\dot{M}_E = \frac{L_E}{\eta c^2} \approx 1.4 \times 10^{18} (M/M_\odot) g s^{-1} \quad (1.2)$$

where a typical (radiation) efficiency factor of $\eta \approx 0.1$ is taken and L_E is the Eddington luminosity, the maximum luminosity allowed by spherically symmetric accretion of hydrogen gas. At this accretion rate, and assuming solar gas composition (i.e., metallicity), the outward radiation pressure equals the gravitational force acting on the accreting matter. Of course, a break of the symmetry of the system and other realities of BH accretion have called into question just how limiting L_E really is. Nevertheless, it is a useful parameter for characterizing different accretion modes.

Most broadly, there are Low-Luminosity AGN (LLAGN), where \dot{M}/\dot{M}_E is smallest, Seyfert galaxies, typically undergoing thin-disk accretion with intermediate \dot{M} , and quasars, the brightest sources which may exhibit accretion rates above \dot{M}_E . Quasars are active galaxies where the central source outshines the galaxy and they are typically high-redshift objects. Seyfert galaxies fall into two categories, Seyfert Is with a line of sight to the central accretion disk, and Seyfert IIs, where the central disk is obscured by the outermost part of the disk, known as the ‘dusty torus’. These AGN are further characterized by broad and narrow emission line regions, varying levels of absorption, presence or absence of highly collimated relativistic outflows

called jets, varying radio emission rates and morphologies potentially linked to jet power, and lower velocity outflows referred to as winds.

Though the process is far from fully understood, there is ample observational evidence (see [Fabian, 1994](#), for a review) that the high radiative output and especially the high-velocity outflows can influence the host galaxies or galaxy clusters of AGN. Powerful radio emission is detected to emanate from the narrow body and base of many jets, but they can be especially luminous at the ‘radio lobe’ structures where highly collimated relativistic jets shock and couple to the intra-cluster medium in some galaxy clusters.

In so-called ‘cool-core’ galaxy clusters, X-ray brightness measured from the central regions implies a cooling time-scale much shorter than what would be consistent with observations. Early explanations invoked conduction of heat into the cores from the large heat reservoir of the surrounding intra-cluster medium (ICM) ([Zakamska and Narayan, 2003](#), etc). However, without some sort of self-regulation of the conduction by turbulence or another process, a conduction-based explanation constitutes a fine-tuning problem.

Arguably a more natural explanation for this cooling flow problem is that the AGN that are clearly interacting with the ICM via their jets are heating it either by driving weak shocks, driving turbulence ([Yang and Reynolds, 2016](#)), or even by introducing cosmic rays ([Ruszkowski et al., 2016](#)). Clearly there are significant open questions in how AGN can use jets or winds to transport energy to their large-scale environment, but as we will show, there is still much work to be done in understanding how much energy an AGN can convert into outflows and what determines its typical accretion mode.

As already mentioned, the large variety of AGN observed is likely due in part to the different properties of the gas funneled to the central SMBHs by the surrounding galactic environments. Complementary to the study of AGN is their low-mass (a few to 10s of solar masses) counterpart, the XRB (see [Remillard and McClintock, 2006](#), for a review). In an XRB, a BH or neutron star accretes through Roche Lobe overflow (low mass XRB) or stellar wind (high mass XRB where the star is high

enough in mass that it undergoes significant mass-loss via. wind) from an orbiting companion that is thought to provide boundary conditions for the accreting system with fewer free parameters.

Near-Keplerian angular momentum in the material feeding onto the disk from the companion star likely means that these systems are always disk-like (see [Begelman, 2014](#)), and in most cases the spin of the BH is expected to be in near alignment with the disk and larger angular momentum of the binary ([Fragos et al., 2010](#)). On the other hand, SMBHs could be misaligned with the net angular momentum of the accreting gas clouds raining from the surrounding ISM, effectively introducing a free parameter to the system which has relatively little numerical exploration thus far.

For nearly all XRBs $\dot{M} \ll \dot{M}_E$ most of the time, and only approaches a significant fraction of \dot{M}_E during ‘outburst’ events. At present, only two systems are observed to likely exhibit super-Eddington states: SS 433, and GRS 1915. They spend most of their time in the ‘low’ or quiescent states where the disk is expected to be a radiatively inefficient accretion flow (RIAF). In such flows the density, and hence collisionality, is too low for most of the energy converted during accretion to radiate away. One type of analytic RIAF commonly applied to model the low/hard and quiescent states is the advection dominated accretion flow (ADAF; [Narayan and Yi, 1994](#); [Abramowicz et al., 1995](#)), where heat is advected across the event horizon with the gas rather than escaping the system. However, on timescales humans can observe, sections of the disks in low-mass XRBs (LMXRB) are believed to fall subject to an instability caused by varying hydrogen ionization levels, which causes periodic bursts in the accretion rate (see [Cannizzo, 1993](#), for a review). Many low-mass BH XRBs seem to at least roughly follow a specific type of cyclical behavior through one of the outburst events illustrated in [Figure 1.1](#).

Starting in a low state of accretion where $\dot{M} \ll \dot{M}_E$, XRBs are referred to as ‘quiescent’ if they are extremely faint, which may be the limiting case of the low/hard state. The accretion flow of a RIAF, is hot because the heat liberated by accretion processes is trapped in the low-density gas. This high temperature causes gas pressure to support a geometrically thick, optically thin disk. Thick disks are

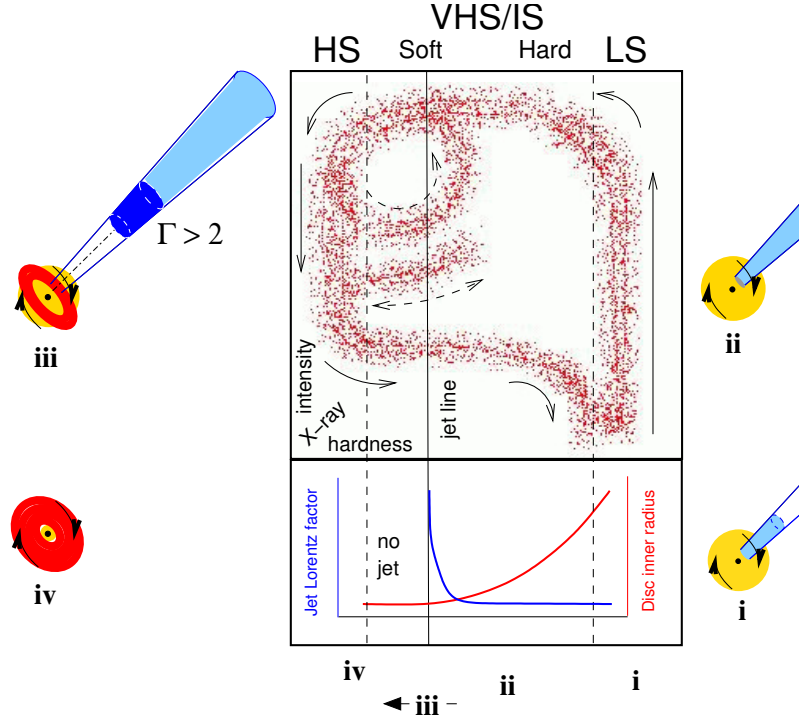


Figure 1.1: This figure reproduced from [Remillard and McClintock \(2006\)](#) shows in red dots the instantaneous measure of hardness and luminosity of a hypothetical LMXRB. The disk spends most of its time in the quiescent state on the lower right corner. During an outburst it goes through disk states **i-iv**. The diagrams around the plot show the dominate components of the accretion/jet inflow/outflow during each accretion state.

thought to be good at collimating outflows either driven by accretion processes in the inner disk or accelerated by the BZ process near the horizon. Power from the latter has long been thought to be amplified by the thick disk because it is effective at advecting poloidal magnetic flux with the flow, increasing flux ‘threading’ the horizon.

Most emission in the low state is attributed to non-thermal processes and is likely dominated by inverse Compton scattering of lower energy thermal photons by high-velocity electrons in a corona. This emission has a strong component that extends into the hard part of the X-ray spectrum, 10-100keV. That, along with low X-ray flux from any thermally dominated disk component in the soft X-ray band of 0.1-10keV leads to a naming convention of ‘low/hard’ for this disk state. Hardness is defined as the ratio of the hard spectral component to the soft.

During an outburst event as \dot{M} rises, the thermal and non-thermal components of the spectrum increase along with the overall luminosity of the system. The hardness of the spectrum remains roughly constant as the flux increases by as much as several orders of magnitude. The epitome of this is called the very high state, where there is, temporarily, a power-law component dominating across most of the X-ray and even up to γ -ray energies in the MeV. Physically, this is usually interpreted as a high- \dot{M} intermediate state leading towards geometrical collapse of the disk as it becomes radiative efficient, but there is still the presence of a hot corona. As the corona, or disk collapses, the jet usually is thought to disappear, i.e., radio emission associated with the jet drops significantly. The intermediate states between the very high state and the next state are broken into two, hard and soft, as the coronal spectral components give way to a thermal multi-temperature black body.

The multi-temperature accretion disk model is thought to be the closest state to the standard SS disk. It is thin, so is traditionally thought to not support a jet (though we shall demonstrate this could be incorrect) and most flux is in thermal components of the spectrum, which is ‘soft’ rather than hard. This high/soft state remains as \dot{M} drops. Once the accretion rate falls low enough there are two branches in the optical depth- \dot{M} parameter space, a very thin optically thick branch and the

ADAF branch. Through an unknown mechanism it is believed that the thin disk evaporates into the ADAF state. This returns the system to the low/hard state and the jet appears to return, along with the associated radio emission.

Since the transition from hard to soft states happens at very different total luminosities depending on the direction taken in the luminosity-hardness diagram, there seems to be some sort of hysteresis that implies the presence of another fundamental parameter of the system besides \dot{M} and spin. Just as the magnetic field can help to explain the complexities beyond the simplest AGN unified models, there are several ways in which magnetic fields could play a role in explaining the hysteresis (Begelman and Armitage, 2014) and other complicated behavior of XRBs.

Even during the high soft state there is often a strong non-thermal component and the interplay between large-scale magnetic field and the corona of disks has become the subject of increasing numerical investigation. How much material is strongly magnetized? How does magnetization effect the presence of a corona in the thin-disk state? How does it affect the presence of a jet? These are questions intimately tied into our understanding of the states of XRBs that we investigate in this thesis.

There is a rich complexity of variability phenomena associated with the study of XRBs that can also be used to gain insight into these accreting systems, but I do not summarize it here because it is not the focus on any of the Chapters that follow.

1.1.2 Geometrically thin, radiatively efficient accretion

The accretion mode associated with the high-soft state in XRB outbursts is most simply modeled using the so-called α -disk model attributed to Shakura and Sunyaev (1973). In their model they assume that energy dissipated by the disk is radiated locally as a blackbody, and angular momentum transport is mediated by an anomalously parameterized torque of the form

$$\nu_T = \alpha c_s H, \tag{1.3}$$

where c_s is the sound speed and H is the scale height of the disk. Reasoning that any hydrodynamic stress can be scaled using the total pressure P , as αP , Shakura and Sunyaev arrived at the above formula starting with a simplified form of the stress energy tensor in a Keplerian disk. However, one can arrive at the same equation considering a simple physical description: consider momentum transport through turbulent eddies communicating angular momentum between radii within the disk. A natural scale for the eddies is the height of the disk with a natural bulk motion moving with the speed of sound.

The anomalous viscosity model of SS was generalized to the Kerr space-time of a spinning BH by Novikov and Thorne (1973a) (NT73). As a simplified picture, consider the potential energy $U = GMm/r$ of a mass m at radius r in a disk surrounding a central mass M . The rate of energy conversion, from the Virial theorem, is

$$L \approx \frac{1}{2} \frac{dU}{dt} = \frac{GM}{2r} \frac{dm}{dt} = \frac{GM\dot{M}}{2r}. \quad (1.4)$$

This combined with Eqn. 1.1 shows that $\eta \propto M/r$. This is a measure of compactness of the system at its terminal radius, which for a BH is naturally given by the innermost stable circular orbit (ISCO), inside of which gas plunges into the horizon and there is no further dissipation (in these idealized models) of energy. The total energy available from a mass falling from infinite radius to the ISCO is

$$\frac{U}{2} = \frac{GMm}{2 \cdot 3R_s} = \frac{GMm}{12GM/c^2} \approx 0.08mc^2, \quad (1.5)$$

where R_s is the Schwarzschild radius. This gives an approximation to the actual value for a non-spinning BH in NT73 that is surprisingly close to the expected value.

While the SS or NT thin disk, parameterized by a constant average viscosity parameter at all radii, α , is an extraordinarily simple picture of accretion when the disk material is able to efficiently radiate dissipated energy, that simplicity has made it valuable when applied to constraining observations.

The fundamental physical assumptions in the standard disk model are the form of the viscosity, zero stress inside the ISCO, a near-Keplerian rotation profile, and lack of any wind or deviation from black body radiation of energy from the disk,

radiation of dissipated energy locally to where its dissipated, and a shared axis between the BH and the disk angular momenta. Also, there is an inherent assumption of locality in the sense that different disk radii are only causally connected through the viscous torque in the disk. It should be noted also that the NT and SS solutions reveal the disk is radiation-pressure dominated close to the BH.

The focus of the next two chapters in this thesis concern the relaxation of several of these assumptions while remaining in the optically thick, geometrically thin accretion flow mode. Our primary concern will be with the effects of large-scale and dynamically relevant magnetic fields.

1.2 Magnetic fields in disks

The simple models for accretion discussed so far have assumed only the unmagnetized fluid equations for conservation of mass, angular momentum, and energy. Before considering the effects of magnetic fields of varying strengths and topology on accretion disks around BHs, first consider the equations of ideal MHD in conservative form,

$$\frac{\partial \rho}{\partial t} + \nabla \cdot [\rho \mathbf{v}] = 0, \quad (1.6)$$

$$\frac{\partial \rho \mathbf{v}}{\partial t} + \nabla \cdot [\rho \mathbf{v} \mathbf{v} - \mathbf{B} \mathbf{B} + \mathbf{P}^*] = 0, \quad (1.7)$$

$$\frac{\partial E}{\partial t} + \nabla \cdot [(E + P^*) \mathbf{v} - \mathbf{B}(\mathbf{B} \cdot \mathbf{v})] = 0, \quad (1.8)$$

$$\frac{\partial \mathbf{B}}{\partial t} - \nabla \times (\mathbf{v} \times \mathbf{B}) = 0, \quad (1.9)$$

where \mathbf{P}^* is a diagonal tensor with components $P^* = P + B^2/2$ (P is the gas thermal pressure component), E is the total energy density

$$E = \frac{P}{\gamma - 1} + \frac{1}{2} \rho v^2 + \frac{B^2}{2}, \quad (1.10)$$

and $B^2 = \mathbf{B} \cdot \mathbf{B}$. In the units chosen, the magnetic permeability $\mu = 1$.

Closure is provided by the equation of state for an ideal gas, $P = (\gamma - 1)e$ (where γ is the ratio of specific heats, and e is the internal energy density). Equa-

tions 1.6, 1.7, and 1.8 are the non-relativistic conservation equations for rest mass, momentum, and energy, respectively with no external sources in Minkowski (i.e., flat) space-time, for simplicity. We could add to these equations some source terms on the right hand side, and will use numerical solutions of those more complex forms of the equations of magnetohydrodynamics (MHD) in the chapters representing the work of my thesis below. For relativistic accretion flows around BHs it is also necessary to formulate the equations of MHD in a covariant way. For now, let us continue with the simplified form.

1.2.1 Magnetorotational instability

In a landmark invocation of a property of rotational shearing flows first explored in the context of Taylor-Couette flows by Velikhov (1959) and later again by Chandrasekhar (1961), Balbus and Hawley (1991) showed that a weak-field MHD instability, the magneto-rotational instability (MRI), can drive vigorous turbulence in accretion disks. Thus, the MRI provides a natural process for self-consistent angular momentum transport. Turbulence was thought to be necessary to transport angular momentum because shear viscosity of the gas alone in disks would provide torques many orders of magnitude too small to explain observations, if the empirically determined $\alpha \sim 0.1$ is typical.

The MRI manifests in its simplest form for a vertical (z) (poloidal) magnetic field with a radial (r) perturbation, where there is shear in the ϕ direction, such as that found in a differentially rotating accretion disk.

Using a standard perturbation analysis on the linearized MHD equations in a locally co-rotating frame in a disk with a Keplerian radial profile for $v_\phi(r)$, one reduces the linearized conservation equations to get the linear dispersion relation for perturbation $\vec{k} = k\hat{z}$ with frequency ω ,

$$\frac{\omega^2}{\Omega^2} = q^2 + \frac{1}{2} \left(1 \pm \sqrt{1 + 16q^2} \right), \quad (1.11)$$

where the reduced wavenumber $q = kv_A/\Omega$, and $v_A = B/\sqrt{4\pi\rho}$ is the Alfvén speed. k must not be smaller than $\sim 1/H$, otherwise the perturbation would not fit within

the disk, but otherwise, for small allowed q , the growth rate is set by the imaginary component of ω for the minus version of Eqn. 1.11, which is $\text{Im}(\omega) \simeq \sqrt{3}q\Omega$. The maximum growth rate (fastest growing and therefore dominating MRI mode) is with $q = \sqrt{15/16}$, where one e-folding happens at the frequency $(3/4)\Omega$. This means the MRI can amplify the magnetic field on a sub-orbital timescale! If the magnetic field becomes strong, the Alfvén velocity increases and when $q \geq \sqrt{3}$ this mode is stable. If all modes that fit within the scale-height H of the disk are stable, then the MRI is quenched and some other process must drive accretion.

Physically one can understand the MRI using the following Gedanken experiment: consider two parcels of gas at adjacent radially locations, connected by the radially perturbed magnetic field oriented in the z direction as above. You can think of the field as a spring connecting the two masses (Gammie, 2004). As the gas mass m_2 at the outer radius falls behind gas mass m_1 with a faster rotational velocity, the magnetic field connecting them deforms further in the ‘S’-like shape sinusoidal shape of the perturbation, storing a bit of energy itself in magnetic tension, while also transferring a bit of angular momentum and kinetic energy from m_1 to m_2 . With less angular momentum m_1 falls to a lower orbit and m_2 similarly moves outward to a larger orbit, thereby further stretching the connecting field. Of course, if the field is too strong, the magnetic tension will resist the initial radial displacement altogether.

The non-linear saturation of the MRI and the transition to turbulence has a rich history of exploration (Balbus and Hawley, 1991, 1998a; Hawley et al., 1995; Stone et al., 1996; Pessah et al., 2007; Sorathia et al., 2010, 2012). With the discovery of the MRI, simulations of accretion disks could be achieved with fully self-consistent angular momentum transport!

As you can see, even the inclusion of weak (plasma β parameter, ratio of magnetic to thermal pressure, is $\ll 1$) magnetic fields represents a significant departure from the idealized thin disk framework. Though the MRI does supply self-consistency to the idea of high α angular momentum transport, the magnetodynamo action of the saturated-state MRI continually produces magnetic patches

which can be transported to the surface of the disk by convection and drive a disk wind. The nature of the magnetic field can also further enhance the asymmetry of stresses within the disk.

As simulations of BH accretion, typically using a pseudo-Newtonian approximation to the gravitational potential, developed from 2D to 3D, and from shearing box to vertically stratified shearing box, to semi-global and ultimately to fully global simulations, a wealth of non-linear behavior has been uncovered which may explain the variability and complex spectral energy distributions seen in real systems. Even with the sub-sample of arguments presented so far in this thesis, it is clear that including the event horizon of the BH as a realistic inner boundary, and including the full influence of the Kerr space-time is absolutely key in understanding the highest energy emission and most rapid variability from BH systems.

I have discussed the MRI in the context of weak magnetic fields, but there is no *a priori* reason the field should be weak! If the poloidal magnetic field is strong enough for the smallest unstable mode to not fit vertically within the disk body, then the axisymmetric MRI is quenched, and accretion proceeds through magnetic Rayleigh-Taylor interchange modes instead. This is the so-called ‘magnetically arrested’ disk state that is explored in various experiments in the next three chapters.

1.2.2 Magnetic topology and field strength

The first GRMHD simulations (starting with [Wilson \(1977\)](#)) with full time-independent GR of global disks have typically included weak initial magnetic fields of either a single set of large poloidal loops tracing pressure contours of a hydrostatically stable torus, or a series of poloidal loops with alternating field direction to avoid introducing surfaces of artificial reconnection in the initial conditions.

These magnetic field initializations are useful in studying the magneto-dynamo and carrying out simulations with high resolution to study disk turbulence. A lack of large-scale magnetic field threading the disk minimizes activity very far off the equatorial plane, so one can even save computing resources by cutting out large polar conical zones without significantly effecting disk behavior.

However, many real BH systems at any given time have access to large amounts of large-scale poloidal magnetic flux (Zamaninasab et al., 2014; Mocz and Guo, 2015) either from the surrounding environment or from remnant structures from a prior epoch of accretion, and so the inclusion of these large-scale fields in simulations with focused self-consistency is key. For instance, large scale magnetic field can be advected inward and accumulate on the horizon affecting many aspects of the accretion inflow/outflow behavior, as we will soon discuss. Also, large-scale magnetic fields launch powerful mass-loaded winds to high latitudes and so no conical excision of the grid around the poles will suffice if we want to capture this part of the system.

In addition to magnetic topology, the initial field strength can significantly affect the accretion disk as well (Penna et al., 2010a; Bai and Stone, 2013; Salvesen et al., 2016). Strong magnetic fields can enhance magnetic torques within the disk and affect the efficiency of magnetically driven winds and the strength of the jet driven by the spin of the BH via the Blandford-Znajek mechanism (BZ; Blandford and Znajek, 1977). Though simulations have yet to show if toroidally dominated magnetic field configurations, i.e., disks with only small patches of local net vertical flux, can lead to powerful jets, inclusion of large scale poloidal flux threading through a disk can drive powerful jets in simulations when either the disk is very thick and confining, or the spin of the BH is close to maximal.

Of fundamental importance is whether large scale magnetic fields can be transported to the inner disk and the horizon. If they can, the impact of magneto-centrifugally driven winds (Blandford and Payne, 1982; Bai and Stone, 2013, etc) on disk stability and structure, contribution of large-scale poloidal flux to jet power, and overall accretion efficiency of BH systems, could mean that the large-scale magnetic field is as fundamental a free parameter governing the observed behavior of BH systems as \dot{M} and inclination of the observer.

Most of the body of work presented in this thesis concerns the transport of large-scale magnetic flux and the associated influence on accretion flows.

1.3 Numerical methods

There are a plethora of techniques invoked by numerical experimentalists to solve the equations of MHD in various astrophysical contexts. I only attempt here to provide an overview of the particular choice of techniques implemented in the codes Athena (Stone et al., 2008) and HARM (Gammie et al., 2003; McKinney and Blandford, 2009; McKinney et al., 2012), used to carry out the work of this thesis, with a focus on the implementation in the latter. Teyssier (2015) and the Living Review of Font (2008) provide nice reviews of techniques used to solve the fluid and MHD equations in astrophysics.

1.3.1 Finite volume approach

Both Athena and HARM (and the extension HARMRAD (McKinney et al., 2014) which includes self-consistent radiative transport) are built upon a fundamentally conservative approach of the finite volume form. Rather than evolving quantities like ρ , $\rho\vec{v}$, \vec{B} , etc. at discrete points and approximating fluxes, by tracking a set of “conserved” quantities that are volume averaged over grid cells and accounting for transport of those quantities via fluxes across cell faces, one can precisely conserve their volume integrated totals to machine precision. It is the simple principle that whatever conserved quantity is lost by one cell is exactly captured by another.

While the simpler implementation of schemes that were not total-energy-conserving, such as ZEUS (Stone and Norman, 1992), makes them somewhat easier to write and run faster on computers, they can be less accurate, for instance, when used to study systems where the internal energy is a significant fraction of the total. Some non-energy-conservative schemes with artificial viscosity have trouble with relativistic shocks (Norman and Winkler, 1986). A major advantage of conservative schemes is that in one dimension, those methods that are total variation stable are guaranteed to converge to a *weak solution* of the equations (Lax and Wendroff, 1960; LeVeque, 1998). Though this does not strictly apply for higher spatial dimensions,

it is a promising starting point.

The basic method for solving a set of hyperbolic equations (like those of MHD) upon which the higher-order schemes of Athena and HARMRAD grew is called Godunov's scheme, which in its simplest form is first order accurate in space and time. It makes use of updates to conserved volume-integrate quantities using fluxes calculated by solving the Riemann problem at cell interfaces. A Riemann problem is an initial value problem associated with a conservation equation and piecewise constant values, such as those on the grid considered here.

Without sources, a system of hyperbolic conservation laws can be written in equations of the form

$$\frac{\partial q}{\partial t} + \nabla \cdot \mathbf{F}_q = 0, \quad (1.12)$$

where q is one conserved quantity of the system transported via flux \mathbf{F}_q .

Consider discretization of these quantities onto a grid (of 1 dimension for purpose of illustration) in the x direction, where at each discrete time step the spatial average of $q(t^n, x)$ is associated with cell center i , and is averaged over the volume between evenly spaced cell interfaces at $i - 1$ and $i + 1$, so that the volume averages are

$$Q_i^n = \frac{1}{\Delta x} \int_{x_{i-1/2}}^{x_{i+1/2}} q(t^n, x) dx. \quad (1.13)$$

Let's re-write Eqn. 1.12 as

$$q_t + (F(q))_x = 0, \quad (1.14)$$

where the sub-scripts represent partial derivatives.

If we integrated this over the volume of the cell we obtain

$$\frac{\partial}{\partial t} Q_i(t) = -\frac{1}{\Delta x} (F(q(t, x_{i+1/2})) - F(q(t, x_{i-1/2}))). \quad (1.15)$$

Now we time integrate through one step t^n to t^{n+1} , which yields the exact update formula,

$$Q_i^{n+1} = Q_i^n - \frac{1}{\Delta x} \int_{t^n}^{t^{n+1}} (F(q(t, x_{i+1/2})) - F(q(t, x_{i-1/2}))) dt. \quad (1.16)$$

In this low-order formulation, Godunov’s method uses the forward Euler method to replace each of the time integrated terms so that, for example,

$$\int_{t^n}^{t^{n+1}} F(q(t, x_{i+1/2})) dt \approx \Delta t f(Q_{i-1}^n, Q_i^n), \quad (1.17)$$

where f is found by solving the Riemann problem for flux at the interface with left and right values given by the left and right states Q_{i-1}^n and Q_i^n .

Therefore, the final update for the unknown Q_i from t^n to t^{n+1} is given by

$$Q_i^{n+1} = Q_i^n - \frac{\Delta t}{\Delta x} (f_{i+1/2}^n - f_{i-1/2}^n). \quad (1.18)$$

You can identify immediately from inspection which of the above steps in the method might be improved to higher order accuracy. For instance, the left and right states used to find fluxes by solving the Riemann problem at cell face $i - 1/2$, could be found using an interpolation rather than the strict values Q_{i-1}^n and Q_i^n . Similarly, a higher order time-step could be taken than the first-order Euler approximation in Eqn. 1.17. As a final example, approximate Riemann solvers can be used in circumstances where it is computationally expensive to iterate to an exact solution.

1.3.2 HARM

Though I will not attempt to fully cover the methodology of the numerical scheme called HARM, for high-accuracy relativistic magnetohydrodynamics ([Gammie et al., 2003](#)), I will attempt to outline the ways it extends beyond the basic introduction above.

Certainly the most significant extension is that of a general relativistic formulation of the MHD equations accounting for an arbitrary space-time metric, and which allows HARM to be used to simulate BH accretion disks following the flow self-consistently all the way past the event horizon. This, for instance, allows the extraction of rotational energy from the spinning black hole by surrounding magnetic field which has been shown to launch powerful jets via the BH mechanism.

The conservative scheme in HARM updates a set of conserved variables

$$\mathbf{U} \equiv \sqrt{-g}(\rho u^t, T_t^t, T_i^t, B^i), \quad (1.19)$$

where T_ν^μ is the stress energy tensor subject to the four equations expressing conservation of energy and momentum,

$$T_{\nu;\mu}^\mu = 0, \quad (1.20)$$

and B^i is the magnetic field 3-vector.

The MHD conservation equations are solved in a coordinate basis and if we write this out as such,

$$\partial_t(\sqrt{-g}T_\nu^t) = -\partial_i(\sqrt{-g}T_\nu^i) + \sqrt{-g}T_\lambda^\kappa\Gamma_{\nu\kappa}^\lambda, \quad (1.21)$$

one can see how the curvature of space effective adds a source term to the conservations equations.

Along with the vector of conserved variables, a vector of “primitive” variables is needed to model the flow within zones,

$$\mathbf{P} = (\rho, u, v^i, B^i). \quad (1.22)$$

$v^i = u^i/u^t$ is the 3-velocity. Both the primitive and conservative variables are used within the numerical scheme of HARM, but only the conserved quantities are updated directly. Therefore, HARM uses a multi-dimensional Newton-Raphson routine to solve for $\mathbf{P}(\mathbf{U})$ at the end of each time-step.

The original version of HARM in the 2003 paper evaluates fluxes using an MUSCL-type scheme, the HLL approach ([Harten et al., 1983](#)), with a monotized central “Woodward” limiter (other limiters available). More sophisticated formulations such as the HLLC scheme are used for the work presented in the following chapters.

The version of HARM used in the work of this thesis implements choices of constrained transport scheme based on weighing trade-offs of stability and speed in each problem studied. In general, the method of constrained transport, which manifestly conserves $\nabla \cdot \vec{B} = 0$, follows a similar procedure to the Gudunov method outline above. Electromotive forces, integrated along the edges of grid cell faces are used to update the face-centered (i.e., staggered) magnetic field vector quantities.

HARM has gone through multiple generations of code verification tests with each new code addition, and scales very well for $> 10^4$ cores on supercomputers, making it an ideal code to test global accretion problems onto BHs and to study the effects of the extreme BH space-time.

1.3.3 Radiative GRMHD

The work in Chapters 3 and 4 involve a new code HARMRAD (McKinney et al., 2014), which solves the equations of GRMHD + radiative transport using a closure scheme for the radiation called M1 (Levermore, 1984). This closure formulation has the form

$$\mathbf{P}^{ij} = E \mathbf{T}^{ij}(E, \mathbf{F}^i), \quad (1.23)$$

where \mathbf{P} is the radiation pressure tensor, E is the energy density of radiation in the lab frame, and \mathbf{T} is the Eddington tensor. In the M1 closure, the Eddington tensor is taken to be only a function of the first two moments of the specific intensity, the radiative energy density and the radiative flux vector, respectively, and is further assumed to be a linear combination of the isotropic unit tensor and the directional tensor taken in the direction of the radiative flux. In the rest frame of the radiation fluid, the specific intensity is isotropic. In any other frame (rest frame of fluid or laboratory, for instance) the radiation field is Dirac-distributed in the direction of the radiation ‘flow’.

The M1 formulation has several advantages in its treatment of radiation. One key feature is the ability of the M1 approach to handle radiation fields that have both optically thick and thin regions, with a natural scaling for all intermediate states! It deals with shadows much better than flux limited diffusion, where the radiation pressure tensor is assumed to be proportional to the local gradient of E alone, and M1 does not have the spurious angular affects when free-streaming over large distances that the variable Eddington tensor (VET) formulation has (see Jiang et al., 2012, and references therein). However, M1 does not deal well with converging radiative zones, where the two incoming radiative fluids can merge in

unphysical ways rather than free-streaming through each other.

In any case, M1 offers a good choice when trying to understand the radiation produced by optically thick, geometrically thin flows, where radiation is processed by the optically thick disk before being radiated away (and, as I will show, into a wind that can substantially re-processes the radiation).

The numerical techniques used to solve the equations in HARMRAD and for GRRMHD (GRMHD + radiation) in general are similar to those outlined above and those implemented in HARM. The radiation adds sometimes stiff source terms to the conservation equation, and so they are usually dealt with using a hybrid explicit/implicit method where fluxes, conserved quantities, and source terms are updated iteratively, solving the radiative MHD equations to 2nd order or more in time and space.

1.4 Outline - Description of chapters

As introduced above, there are several fundamental problems in BH accretion that can be addressed using a code that solves the equations of GR(R)MHD:

- (1) Are geometrically thin, radiatively efficient disks able to advect large-scale poloidal magnetic flux inward? If so, can it reach the MAD state, where the MRI is quenched the the fundamental behavior of the accretion mode could be very different than our standard model of thin-disk accretion? Is MAD an inevitable outcome?
- (2) What is the behavior of a MAD thin disk?
- (3) What is the radiative efficiency of a MAD thin disk? Is it enhanced compared to that predicted by the standard NT model of accretion?
- (4) What is the radiative efficiency of super-Eddington accretion in the MAD mode?

Chapter 2 addresses the first three problems listed, but uses an *ad hoc* cooling function to keep the disk thin and to estimate radiative efficiency of the MAD

thin disk. Chapter 3 is very similar in setup but uses HARMRAD to address the same problems with self-consistent radiative transport. Chapter 4 describes the use of HARMRAD in simulating thicker, super-Eddington MAD accretion flows, where characteristics of the flow associated with the MAD state are responsible for significant enhancement of radiative efficiency compared to traditional super-Eddington, or slim-disk models of accretion.

In addition to my work studying BH accretion flows using ideal MHD, as part of my early graduate work I studied an astrophysical problem in which non-ideal MHD effects, namely anisotropic conduction, must be accounted for. Chapter 5 is comprised of this study of properties of heat transport in the intracluster medium of galaxy clusters. The efficiency of accreting SMBHs in these systems, and the coupling of that energy output to the ICM, is still under dispute under the title of the ‘cooling flow problem’. While Chapters 2-4 address the energy output of AGN in various states, Chapter 5 addresses a related issue: is efficient coupling of AGN power to the ICM necessary to provide the required heating, or can regulated heat conduction solve the problem without the invocation of AGN feedback. Future studies of BH accretion flows will necessitate similar departures from ideal MHD. In fact, simulations of disks with weakly collisional and collision-less plasmas are already under way.

Chapter 2: Efficiency of Thin Magnetically-Arrested Disks Around Black Holes

Abstract

The radiative and jet efficiencies of thin magnetized accretion disks around black holes (BHs) are affected by BH spin and the presence of a magnetic field that, when strong, could lead to large deviations from Novikov-Thorne (NT) thin disk theory. To seek the maximum deviations, we perform general relativistic magnetohydrodynamic (GRMHD) simulations of radiatively efficient thin (half-height H to radius R of $H/R \approx 0.10$) disks around moderately rotating BHs with $a/M = 0.5$. First, our simulations, each evolved for more than $70,000 r_g/c$ (gravitational radius r_g and speed of light c), show that large-scale magnetic field readily accretes inward even through our thin disk and builds-up to the magnetically-arrested disk (MAD) state. Second, our simulations of thin MADs show the disk achieves a radiative efficiency of $\eta_r \approx 15\%$ (after estimating photon capture), which is about twice the NT value of $\eta_r \sim 8\%$ for $a/M = 0.5$ and gives the same luminosity as a NT disk with $a/M \approx 0.9$. Compared to prior simulations with $\lesssim 10\%$ deviations, our result of an $\approx 80\%$ deviation sets a new benchmark. Building on prior work, we are now able to complete an important scaling law which suggest that observed jet quenching in the high-soft state in BH X-ray binaries is consistent with an ever-present MAD state with a weak yet sustained jet.

2.1 Introduction

Black hole (BH) accretion systems can operate as efficient engines converting gravitational potential energy and BH spin energy into radiation. Quasars, active

galactic nuclei (AGN), X-ray binaries, gamma-ray bursts, and other BH accretion systems enter a thin radiatively efficient mode when the luminosity is between $\sim 10^{-2}$ and ~ 0.5 times the Eddington luminosity (Abramowicz et al., 1995; Narayan and Yi, 1995). The Novikov and Thorne (1973b), NT, calculation for the thin disk radiative efficiency assumes emission terminates at the inner-most stable circular orbit (ISCO). However, accretion is driven by magnetic stresses via the magneto-rotational instability (MRI) (Balbus and Hawley, 1991, 1998a) or magnetic braking by large scale field threading the disk (Blandford and Payne, 1982) or BH (Blandford and Znajek, 1977), hereafter BZ. A fundamental question in accretion theory has been whether the NT model is applicable to actual magnetized disks where magnetic flux couples to a rotating BH and increases the radiative efficiency near the ISCO (Gammie, 1999; Krolik, 1999). Any extra radiative efficiency could, in principle, affect BH spin estimates obtained from Soltan’s argument (e.g., see Shapiro 2005) or from continuum emission spectrum observations (McClintock et al., 2011).

An upper limit to the amount of magnetic flux a disk and BH in steady-state can support is achieved when an accretion flow reaches the so-called magnetically-arrested disk (MAD) state, when magnetic flux accretes until magnetic forces pushing out balance gas forces pushing in (Igumenshchev et al., 2003; Narayan et al., 2003; Igumenshchev, 2008; Tchekhovskoy et al., 2011; McKinney et al., 2012). If jet power scales as $P_j \propto B^2 a^2$ for magnetic field B and BH spin a/M (Blandford and Znajek, 1977), then the MAD state leads to the maximum jet power. The existence of such a maximum well-defined magnetic flux for a given spin is assumed when using transient jets in BH X-ray binaries to test the BZ prediction of power vs. spin (McClintock et al., 2014). Destruction of such a strong magnetic flux could lead to such transient jets without the need for BH spin (Igumenshchev, 2009; Dexter et al., 2014), while BH spin measurements may be more reliable for thin MADs that could have angular momenta aligned with the BH spin axis near the BH (Polko and McKinney, 2015).

General relativistic magnetohydrodynamic (GRMHD) simulations of thin disks have found different degrees of deviations from NT theory, but in these cases there

are no more than 10% fractional deviations for the radiative efficiency (Shafee et al., 2008; Noble et al., 2009; Penna et al., 2010a; Noble et al., 2010, 2011). Differences in results are likely due to the amount of magnetic flux that threads the BH and disk (Penna et al., 2010a). Unlike other choices for initial conditions, the amount of magnetic flux threading the BH and disk in a MAD state is independent of the initial magnetic field strength or geometry as long as there is a plentiful supply of magnetic flux (McKinney et al., 2012; Tchekhovskoy and McKinney, 2012). Numerous non-MAD GRMHD simulations of relatively thick disks have been performed (De Villiers and Hawley, 2003; McKinney and Gammie, 2004; De Villiers et al., 2005; McKinney, 2005, 2006; Komissarov and McKinney, 2007; McKinney and Narayan, 2007; Fragile et al., 2007; McKinney and Blandford, 2009; Narayan et al., 2012). Simulations of MADs have so-far involved only relatively thick disks with no cooling (Tchekhovskoy et al., 2011; McKinney et al., 2012) and thick disks with radiative transfer (McKinney et al., 2015a).

We perform fully 3D GRMHD simulations of radiatively efficient thin (half-height H to radius R of $H/R \approx 0.1$) disks around rotating BHs (dimensionless spin, $a/M = 0.5$) that reach the MAD state. We expect the MAD to maximize the radiative efficiency of thin disks and lead to the maximum deviations from the NT model. First, we test how easily magnetic flux advects inward by threading the disk with weak magnetic field. Second, we setup a disk that is initially nearly MAD, let it become MAD to large radius, and then measure the radiative efficiency.

We describe the physical and numerical setup in §2.2, present results and provide discussions in §4.3, and summarize in §4.4.

2.2 Fully 3D GRMHD Thin MAD Model

For this study we use the HARM GRMHD code (Gammie et al., 2003) with various improvements (McKinney and Blandford, 2009; McKinney et al., 2012) with two physical setups, both with spin $a/M = 0.5$. Each was run with a low resolution, medium resolution, and high resolution for convergence testing and the high resolu-

tion was used for detailed analysis. We name the simulations in this work MADxy where x=i,f signifies whether the disk starts with enough flux to be nearly MAD in the initial, i, or only MAD in the final, f, state. y=HR,MR,LR distinguishes the grid as high, medium, or low resolution.

2.2.1 Physical Model

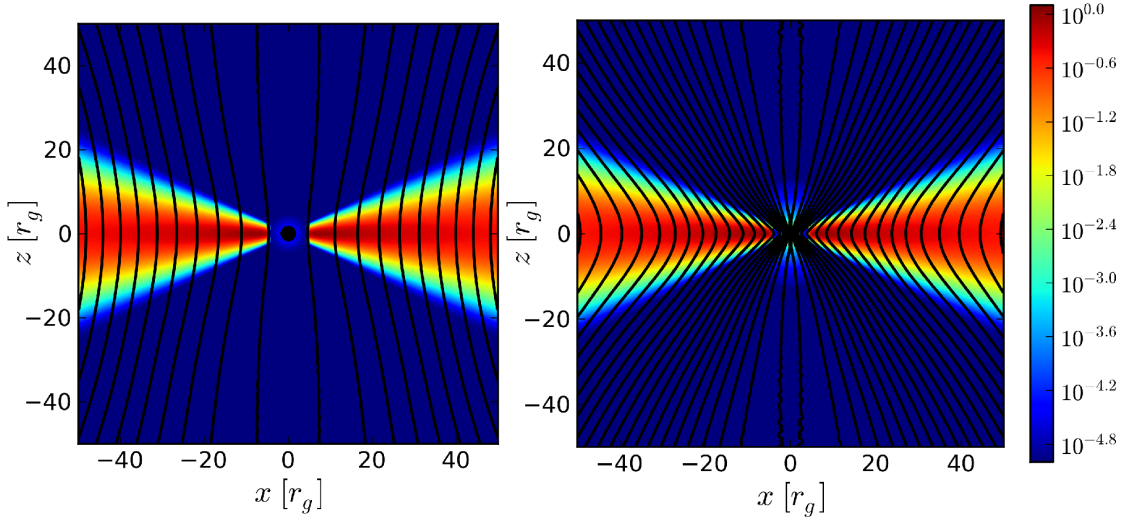


Figure 2.1: Snapshots of the initially sub-MAD (MADfHR - left panel) and nearly-MAD (MADiHR - right panel) models at $t=0$, showing ρ in color (with legend) with magnetic field lines (black lines). In MADfHR there is no magnetic field initially present within the ISCO or on the horizon and the field is weak throughout the disk. On the other hand, in MADiHR, a sufficient magnetic flux is present throughout the disk and on the horizon so that the disk will quickly become MAD out to large radius. The higher density surrounding the horizon in MADiHR at $t=0$ is the result of the density floor activated due to the presence of an initially strong magnetic field.

The initial disk is Keplerian with rest-mass density that is Gaussian in angle with a half-height-to-radius ratio $H/R \approx 0.1$ and a power-law radial distribution $\rho \propto r^{-0.6}$. Since this is not an equilibrium solution near and inside the ISCO at r_{ISCO} , the density is tapered as $\rho \rightarrow \rho(1 - .95(r_{\text{ISCO}}/R)^3)$ and truncated at r_{ISCO} . The

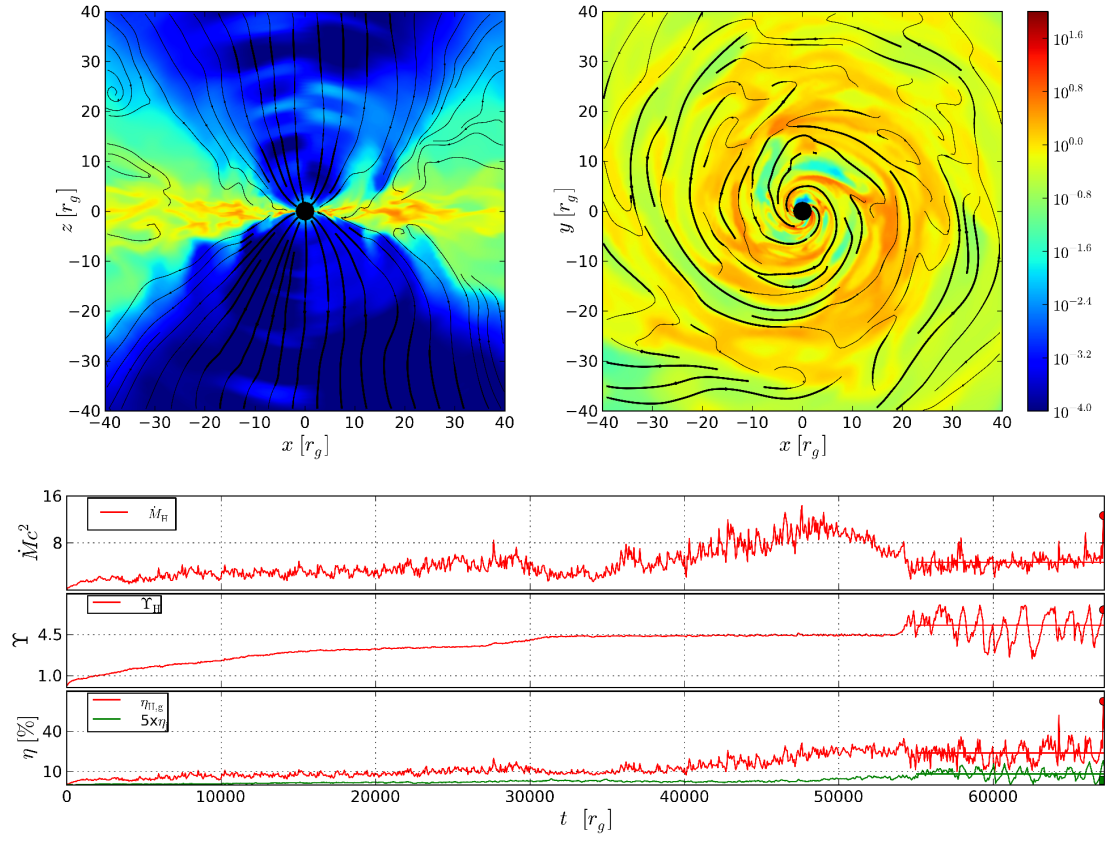


Figure 2.2: (Caption on next page.)

Figure 2.2: (Previous page.) Evolved snapshot of the MADfHR model at $t \approx 70,000r_g/c$ showing log of rest-mass density in color (with legend) in both the $z-x$ plane at $y=0$ (top-left panel) and $y-x$ plane at $z=0$ (top-right panel). Black lines with arrows trace field lines, where thicker black lines show where field is lightly mass-loaded. The bottom panel has 3 subpanels. The top subpanel shows the mass accretion rate through the BH (\dot{M}_H). The middle subpanel shows the magnetic flux threading the BH (Υ_H), normalized so that order unity is a dynamically-substantial amount of magnetic flux. The bottom subpanel shows the gas efficiency measured on the horizon ($\eta_{H,g}$) and jet efficiency measured at $r=50r_g$ (η_j). In this model, the disk initially has a weak large-scale poloidal magnetic field, which is transported by the MRI and other magnetic stresses toward the BH. Eventually, by $t \sim 55000r_g/c$, the magnetic flux saturates on the BH and cannot grow despite plentiful magnetic flux outside. The MAD state that develops consists of a highly non-axisymmetric clumpy thin disk with a weak ($\eta_j \sim 1\%$) jet.

gas internal energy density e_{gas} is obtained from the vertical hydrostatic equilibrium condition of $H/R \approx \bar{h} \equiv c_s/v_{\text{rot}}$ for sound speed $c_s \approx \sqrt{\Gamma P_{\text{gas}}/\rho}$ and rotational speed v_{rot} chosen to be Keplerian with velocity $v_K = (r/r_g)/((r/r_g)^{3/2} + a/M)$. In order to seed the MRI we use a 10% random perturbation to the pressure that obeys the ideal gas law $P_{\text{gas}} = (\Gamma - 1)e_{\text{gas}}$. We choose $\Gamma = 4/3$ because the disk is expected to be radiation dominated near the BH. We set an atmosphere for the disk with $\rho = 10^{-4}(r/r_g)^{-3/2}$ and $e_{\text{gas}} = 10^{-6}(r/r_g)^{-5/2}$.

We choose an initially purely poloidal large-scale magnetic field. With other low resolution (MADxLR) simulations already performed, we know ahead of time the magnetic flux saturation level reached on the BH and throughout the disk in the quasi-equilibrium MAD state, so we then tune our initial conditions to be either nearly MAD (for MADi) or sufficiently sub-MAD to be MRI dominated initially (for MADf). Net magnetic flux on the BH and through the disk out to some radius is conserved and only changes by accretion or expulsion through that radius. We refer to the simulation as in ‘quasi-equilibrium’ when characteristic diagnostics of

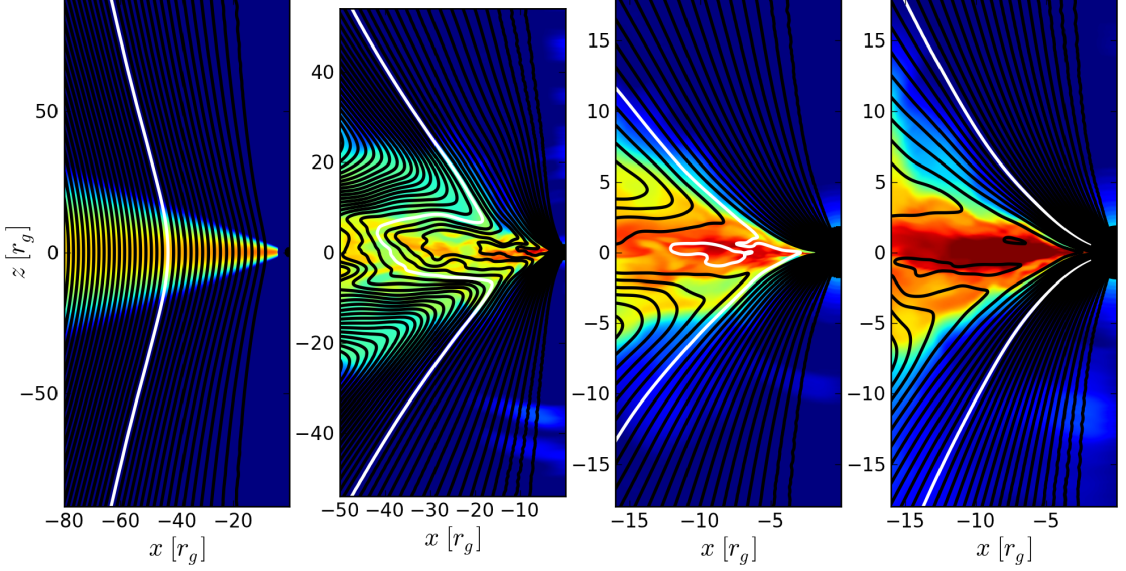


Figure 2.3: (Previous page.) Plotted from left to right are snapshots from MADfHR at $t=[0,10000,16320,40000]r_g/c$. Black contours (with a single colored white) trace the same values on all snapshots and show the ϕ -averaged magnetic field. The contours demonstrate the transport of magnetic flux radially toward the horizon. All magnetic flux is initially threading the disk only, then accretes most rapidly through coronal processes along the surface of the disks where it piles up at these latitudes before it does in the mid-plane of the accretion flow. Reconnection near the horizon where the disk is very thin leads to magnetic loops (seen in middle panel) in the inner disk out to $\sim 20r_g$, where further reconnection and decoupling from the magnetically driven wind cause a drop in the effective disk viscosity. Ultimately the magnetic loops are also accreted and some flux originally threading the disk then threads only the horizon.

the accretion state remain steady, rather than saying it is in ‘inflow equilibrium’, since the magnetic flux beyond that MAD/non-MAD transition radius is still slowly evolving. We consider the simulation in quasi-equilibrium out to the radius at which quantities like \dot{M} are constant, and at least one inflow timescale has been reached, $t_{\text{inflow}} = r/|v_r|$.

In both simulation types, MADi and MADf, our initial conditions, shown in Figure 2.1, provide an effective reservoir of magnetic flux at larger radii that can be accreted by the inner disk and onto the black hole to reach the maximal amount of magnetic flux allowed. The supply reservoir is the same for our two setups to ensure that our two disk states are not the result of initial ‘background solution’ conditions. The supply is vast compared to what ends up on the BH or in the disk near the BH, but not so large that outward diffusion of flux would be prevented by our choice.

The coordinate basis ϕ -component of the vector potential is matched to the radial gas pressure profile so that the plasma parameter $\beta = P_{\text{gas}}/P_b$ (P_b as magnetic pressure), and thus the number of critical MRI wavelengths spanning a full scale-height of the disk, is a tunable constant for all radii. For MADiy runs, we found it useful to transition from MAD-flux levels to a weaker sub-MAD field beyond a transition radius, $r_{0,\text{MAD}} = 30$, with a transition function $F_{\pm} = 0.5 \pm \frac{1}{\pi} \arctan((r - r_{0,\text{MAD}})/4)$. This keeps the evolution of the disks at larger radii the same and allows us to better capture the ‘pile-up’ effect of flux capture producing the MAD state on the BH and inner disk. The vector potential is then calculated by radially integrating

$$A_{\phi,r} \propto (sF_- + F_+) \sin \theta^\nu \cdot \begin{cases} B_0^\theta & \text{if } r > r_{\text{tr}} \\ B_{\text{tr},0}^\theta r^{(-0.6/2+3/2)/\mu} & \text{if } r \leq r_{\text{tr}} \end{cases} \quad (2.1)$$

where B_0^θ is the field threading the disk mid-plane at time $t=0$ necessary to start with $s = 2$ and $\beta = 200/s^2 = 50$ inside $r_{0,\text{MAD}}$, and with $\beta = 200$ elsewhere. Thus, the disk within $r_{0,\text{MAD}}$ initially has $S_d \approx 0.7$, where S_d is the number of MRI wavelengths within two disk scale heights, $S_d \lesssim 0.5$ where the MRI is suppressed (Balbus and Hawley, 1998a), and MADs typically have had $S_d \lesssim 0.25$ (McKinney

et al., 2012). This means the MRI is marginally suppressed in MADs. The field threading the BH horizon and within the ISCO matches to the disk values at a transition radius of $r_{\text{tr}} = 12$. $\mu = 4$ ensures the initial flux residing within r_{tr} is small enough (≈ 2.5 times smaller than what ends up on the BH plus out to r_{tr}) that the BH and the region between the horizon and r_{tr} can slowly build-up to a MAD level.

To ensure a MAD can readily develop for a thin disk, our MADf model starts with sub-MAD flux at $t=0$, with $\beta = 200$ outside r_{tr} . The solution for A_ϕ is the same as the $r > r_{\text{tr}}$ branch of Eq. 2.1 but with $r_{0,\text{MAD}} \rightarrow -\infty$ and a linear taper in the field from r_{tr} to the ISCO so there is no initial magnetic flux any closer.

While there is only a factor of 2 in field strength in the inner disk separating our two initial conditions, these set-ups straddle the boundary of MRI stability in the disk. While MADfy simulations would still be considered to have a strong magnetic field, with the associated large effective viscosity, they are clearly distinguished from the limiting MAD state. Over the course of our MADfHR simulation, the disk and BH inside $r = 35r_g$ accumulate an amount of flux equivalent to that contained in the disk initially out to $r \sim 110r_g$. The disk thus evolves significantly away from its initial conditions toward the MAD limit.

2.2.2 Numerical Grid and Density Floors

We use similar numerical grid mapping and identical boundary conditions as McKinney et al. (2012), except a smooth arctan transition from exponential to hyper-exponential radial grid spacing is used. For our high (mid) resolution grid we choose resolution $N_r \times N_\theta \times N_\phi = 192 \times 96 \times 208$ ($168 \times 64 \times 152$) with radial grid spanning $R_{\text{in}} \approx 0.75r_H$ (horizon radius r_H) to $R_{\text{out}} = 10^4 r_g$.

The θ -grid spans from 0 to π with the mapping of McKinney et al. (2012), but with $n_{\text{jet}} = 0$ used for our entire disk since it is thin at all radii. We adjust the constants of the mapping so that at $r/r_g = 6, 30, 100$ we resolve the disk vertically with 56, 62, 60 cells within $\pm 2H = 2 \cdot 0.1R$. We flare the inner radial grid to avoid unnecessarily small limiting time-steps. The polar boundary conditions are trans-

missive (see appendix in [McKinney et al. 2012](#)), and the ϕ -grid is equally spaced from 0 to 2π with periodic boundary conditions.

Apart from our direct resolution studies, we also measure convergence quality factors for the MRI and turbulence correlations lengths. Our values demonstrate good resolution and are reported in Section [2.3.5](#).

2.2.3 Cooling

To keep the disk thin and radiatively efficient, we implement an *ad hoc* cooling function similar to [Noble et al. \(2010\)](#) with

$$S_\nu = \left(\frac{dU}{d\tau} \right) u_\nu, \quad (2.2)$$

as a source term to the conservation equations, $\nabla_\mu T_\nu^\mu = S_\nu$, for gas stress-energy tensor T and 4-velocity u_ν . This assumes an isotropic comoving rate of thermal energy loss $dU/d\tau$. dU is computed so that cooling decreases internal energy toward a target temperature set by the desired $H/R \approx 0.1$ and local density and radius.

Radiative cooling is efficient for a NT thin disk with a cooling timescale on the order of the orbital timescale ([Novikov and Thorne, 1973b](#)). The NT model assumes radiation gets out only by diffusion, while our disk is clumpy and can be optically thin near the ISCO ([Zhu et al., 2012](#)). Radiative GRMHD MAD simulations are required for an accurate cooling timescale, which could be faster than for literal NT disks ([McKinney et al., 2015a](#)). We only try to keep the disk thin, and we settled upon a graded cooling timescale $d\tau$ so that

$$\frac{dU}{d\tau} = -\frac{\rho T_{\text{target}}}{d\tau} = -\rho T_{\text{target}} \cdot \begin{cases} \Omega_K / \tau_{\text{cool}} & \left(\frac{H}{\nu_{\text{Alf}}} \right) > \tau_{\text{cool}} / \Omega_K \\ \frac{\nu_{\text{Alf}}}{H} & \tau_{\text{cool}} / \Omega_K > \left(\frac{H}{\nu_{\text{Alf}}} \right) > 2\Delta t \\ \frac{1}{2\Delta t} & \left(\frac{H}{\nu_{\text{Alf}}} \right) < 2\Delta t \end{cases} \quad (2.3)$$

where ν_{Alf} is the Alfvénic frequency and thus H/ν_{Alf} is the Alfvén time across one disk scale height, $2\Delta t$ is the code time-step with a prefactor 2 for stability, and $\Omega_K = v_K/r$. The target temperature is from thin disk theory and is isotropic across

cylindrical radii R ,

$$T_{\text{target}} \equiv \left(\frac{0.1 \cdot R}{a + r^{3/2}} \right)^2$$

where the denominator uses spherical radius r to control the temperature along the polar axes. If $T_{\text{gas}} = P_{\text{gas}}/\rho < T_{\text{target}}$ then $dU/d\tau = 0$. To ensure there is always rapid enough cooling, we set $\tau_{\text{cool}} = 0.1 \cdot 2\pi$ that enforces cooling on $1/10^{\text{th}}$ the orbital timescale.

We also use a temperature ceiling that acts as another cooling term, operating after each timestep. We limit the temperature where $\beta < 0.1$ and $T_{\text{gas}} > T_{\text{target}}$. Unfortunately these losses were not tracked in the version of HARM used. When we sum the radiative losses from the cooling function during our analysis, in order to compute the contribution lost to the temperature ceiling, we restarted MADiHR at a late time with the ceiling turned off. The additional heat is then captured by the cooling function which we can measure for the radii near the BH where the temperature ceiling mattered. Accounting for all cooling effects gives us a nearly constant radial profile for total efficiency, and so the procedure correctly recovers how a steady-state flow should behave.

Rest-mass density is injected whenever $2P_b/\rho > 200$ in order to ensure the code remains stable, and internal energy density is added when $e_{\text{gas}}/\rho > 100$ (though this limit is never reached).

The cooling keeps the disk very close to the target scale height. After a very short ($< 5000r_g/c$) initial period of disk evolution, the disk height is very stable.

2.2.4 Diagnostics

The disk's geometric half-angular thickness (H) per radius (R) is

$$\frac{H}{R}(r, \phi) \equiv \frac{(\int_{\theta} \rho(\theta - \theta_0)^n dA_{\theta\phi})^{1/n}}{(\int_{\theta} \rho dA_{\theta\phi})^{1/n}}, \quad (2.4)$$

where

$$\theta_0(r, \phi) \equiv \frac{\pi}{2} + \frac{(\int_{\theta} \rho(\theta - \pi/2)^n dA_{\theta\phi})^{1/n}}{(\int_{\theta} \rho dA_{\theta\phi})^{1/n}}, \quad (2.5)$$

and with surface differential $dA_{\theta\phi}$. Typically we use $n = 1$ but also compare to using other n .

The radiative energy and angular momentum lost are

$$L_\nu(r) = \int R_\nu^r(r) dA_{\theta\phi} = -\frac{1}{Dt} \int_{Dt} \int_{R_{\text{cap}}}^r S_\nu dt dV, \quad (2.6)$$

respectively, for $\nu = t, \phi$ for some period Dt over all angles with photon capture radius R_{cap} (see §4.3). The radiation contribution from beyond the inflow equilibrium radius ($\sim 30r_g$ for our MADiHR model) is conservatively estimated by using NT's radial dependence.

The mass accretion rate, gas+radiative energy efficiency, and specific angular momentum accreted are, respectively,

$$\dot{M}_0 = \left| \int \rho u^r dA_{\theta\phi} \right|, \quad (2.7)$$

$$\eta = -\frac{\int (T_t^r + \rho u^r + R_t^r) dA_{\theta\phi}}{[\dot{M}_0]_H}, \quad (2.8)$$

$$j = \frac{\int (T_\phi^r + R_\phi^r) dA_{\theta\phi}}{[\dot{M}_0]_H} \quad (2.9)$$

where R is the radiation stress-energy tensor and $[\dot{M}_0]_H$ is the time-averaged \dot{M} on the horizon. These diagnostic quantities are calculated as totals and for the jet and wind. The jet is defined as where $2P_b/\rho > 1$, and the wind is where $2P_b/\rho < 1$ with an outgoing flow. The radiative efficiency and specific angular momentum vs. radius are, respectively, $\eta_r = -L_t(r)/[\dot{M}_0]_H$ and $j_r = L_\phi(r)/[\dot{M}_0]_H$.

Time averages for the MADfHR simulation are made over $55000\text{--}68000r_g/c$, the time period during which the horizon flux has reached the MAD saturation. For MADiHR, \dot{M} is average from $10000\text{--}70000r_g/c$, and all other quantities from $30000\text{--}70000r_g/c$ except where explicitly stated.

With immediate proper normalization (rather than for only final quantities in the flux definitions in McKinney et al. 2012), the half-hemisphere horizon flux is

$$\Psi_H \equiv 0.7 \frac{\int_{\theta=\pi/2}^{\theta=\pi} dA_{\theta\phi} B^r}{\sqrt{[\dot{M}_0]_H}}, \quad (2.10)$$

which is negative compared to the integral from $\theta = 0$ to $\pi/2$, for radial magnetic field strength B^r in Heaviside-Lorentz units.

The θ magnetic flux vs. radius at angle θ is

$$\Psi_\theta(r, \theta) \equiv 0.7 \frac{\int_{r_H}^r \sqrt{-g} dx^{(1)} dx^{(3)} B^{x^{(2)}}}{\sqrt{[\dot{M}_0]_H}}, \quad (2.11)$$

integrated in internal coordinates, $x^\alpha \equiv (t, x^{(1)}, x^{(2)}, x^{(3)})$. Thus, the vertical magnetic flux threading the equator is

$$\Psi_{\text{eq}}(r) \equiv \Psi_\theta(r, \theta = \pi/2), \quad (2.12)$$

and we define the total magnetic flux along the equator as

$$\Psi(r) \equiv \Psi_H + \Psi_{\text{eq}}(r). \quad (2.13)$$

For all forms of Ψ , all ϕ -angles are integrated over.

The absolute magnetic flux (Φ) is computed similarly to Ψ , except one 1) inserts absolute values around the field (e.g. B^r and B^θ in the integrals); 2) puts absolute values around the integral; 3) integrates over all θ then divides by 2; and 4) does not immediately normalize. For example, $\Phi_r(r, \theta) = (1/2) \left| \int dA_{\theta\phi} B^r \right|$.

We introduce the [Gammie \(1999\)](#) model version of Υ for consistency in comparing to previous literature, normalized like our version of Ψ ,

$$\Upsilon \approx 0.7 \frac{\Phi_r}{\sqrt{[\dot{M}]_t}}, \quad (2.14)$$

which accounts for Φ_r being in Heaviside-Lorentz units ([Penna et al., 2010a](#)). Compared to Gaussian units version of $\phi_H \equiv \Phi_H / \sqrt{\dot{M} r_g^2 c}$ defined in [Tchekhovskoy et al. \(2011\)](#), $\Upsilon \approx 0.2 \phi_H$.

Viscous theory gives a GR α -viscosity estimate for v_r of $v_{r,\text{visc}} \sim -G\alpha(H/R)^2 |v_\phi|$, as defined in [McKinney et al. \(2012\)](#), leading to a definition for the measure of effective α -viscosity

$$\alpha_{\text{b,eff}} \equiv \frac{v_r}{v_{\text{visc}}/\alpha}, \quad (2.15)$$

whereas viscosity from local shear-stress in the disk is

$$\alpha_b \approx \alpha_{\text{mag}} = -\frac{b_r b_\phi}{p_b}, \quad (2.16)$$

where we have dropped other (e.g. Reynolds) terms from the full α because they are negligible compared to the magnetic term in the MAD regions of our simulations. These α 's are obtained by separately volume-averaging the numerator and denominator in θ, ϕ for each r with a weight of ρ and only including material with $b^2/\rho < 1$ in order to focus the measurement on the disk material and not the lower density corona. The quantity α_b measures the magnetic stress within the dense regions, while the $\alpha_{b,\text{eff}}$ measures the actual effective α based upon the radial velocity of the dense regions. For example, very little magnetic flux may thread the dense regions, but external magnetic torques may push and drive angular momentum transport and inflow of the dense regions. $\alpha_{b,\text{eff}}$ is only accurate far outside r_{ISCO} because of the G term.

2.3 Results and Discussion

With our fully global 3D GRMHD simulations we can demonstrate whether the non-linear MRI and other MHD physics in thin accretion flows is able to transport large-scale magnetic flux towards the BH and build-up the magnetic field to the MAD state. We first consider a disk with a weak magnetic field using our MADfHR setup to see if magnetic flux transports inward in a thin, MRI-dominated disk. Then, having confirmed thin disks transport magnetic flux efficiently to the BH and inner-radial disk, we use our second setup MADiHR to study a MAD where magnetic saturation is reached to large radii. This two-step procedure is necessary due to the extreme computational resources that would otherwise be necessary to build-up large-scale flux to the MAD state out to large radii in an initially MRI-dominated disk. In the thin-MAD state, we find the horizon contains an equivalent amount of flux as a significant radial portion of the disk, so our simulation with no flux initially inside the inner edge of the disk takes a long time to accrete enough flux to reach the MAD state on the horizon.

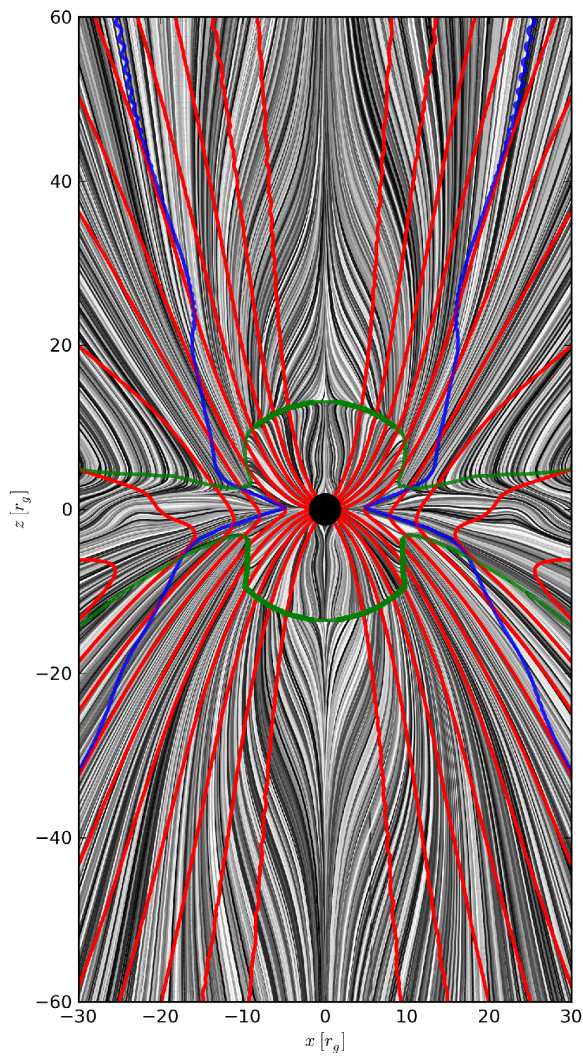


Figure 2.4: (Caption on next page.)

Figure 2.4: (Figure on previous page.) Time and ϕ -averaged quantities are plotted for MADfHR. The time average is taken over 55000-68000 r_g/c , during which time the horizon has reached a MAD saturation of flux. Rest mass gas flow is traced by black streamlines. The colored (green and blue) thick lines correspond to time-averages of quantities $Y = \{u^r, b^2/\rho\}$, respectively, at values $[Y]_t = \{0, 1\}$. While near the BH the flow has $[b^2/\rho]_t \gtrsim 1$ as averaged directly, the dense inflow has $[b^2/\rho]_t \lesssim 1$ at all other radii. The time and spatial variability of the jet causes the time- ϕ average to blend jet and disk material, so the average $[b^2/\rho]_t \gtrsim 1$ bleeds into the disk. Similarly, $[b^2]_t/[\rho]_t$ identifies a jet boundary in the opposite way, causing too much of the polar/jet region to appear to have $[b^2/\rho]_t \lesssim 1$. No particular average is correct, but our choice includes the part of the wind and disk that experiences extra acceleration through interaction with the jet. Streamlines nearest the polar axes are calculated using velocity structure five cells away from the axis for better visualization of the qualitative geometry of the jet flow. The flow exhibits equatorial asymmetry over many inflow times as found in thicker MAD simulations, likely a result of bulk flows associated with the very initial evolution of the disk. The red magnetic field line contours show how the magnetic flux threads the black hole and inner disk.

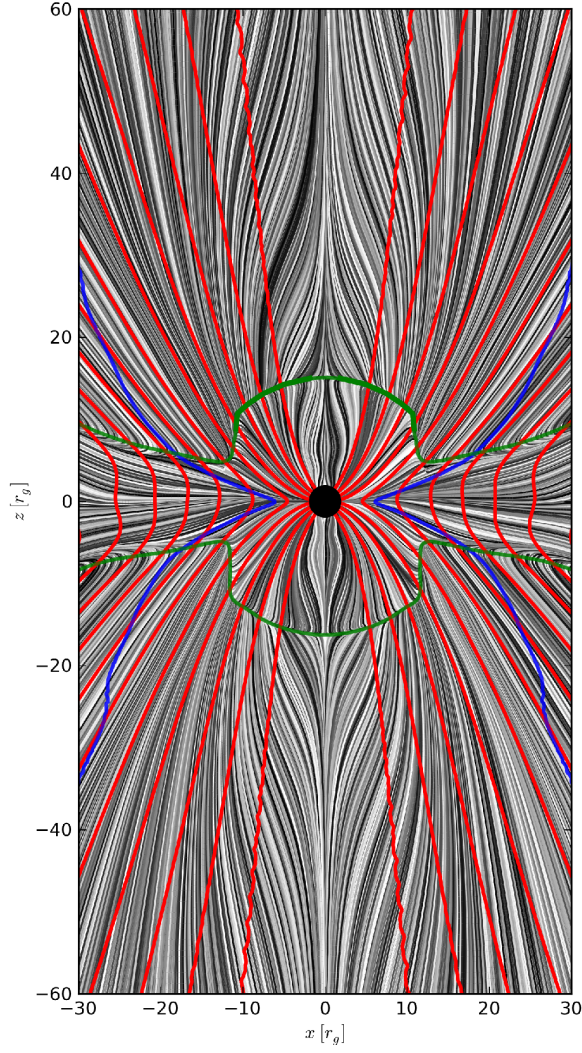


Figure 2.5: Time (from $30000-70000r_g/c$) and ϕ -averaged quantities are plotted for MADiHR. Identical layout as Fig. 2.4. The disk is magnetically arrested out to a transition radius of $\sim 35r_g$, which leads to a short inflow time-scale compared to the MADfHR disk at those radii, so the time-averaged velocity fields and other disk structure is smoother and more symmetric.

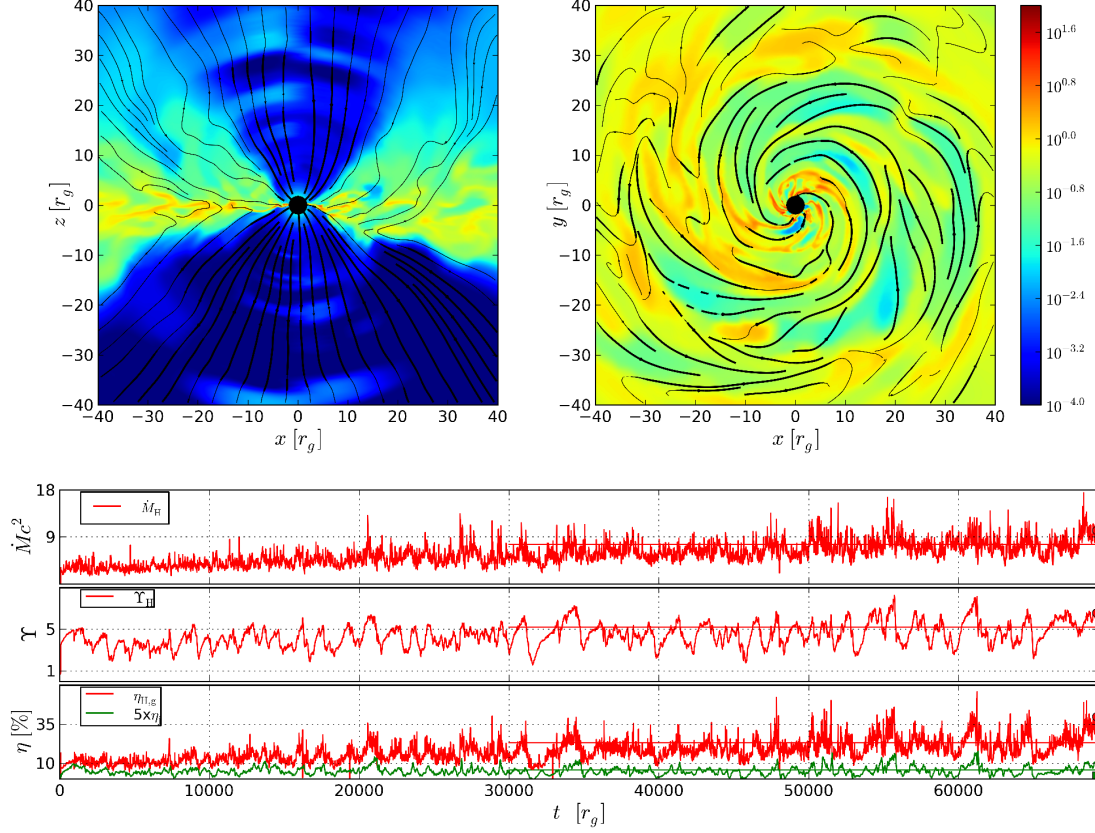


Figure 2.6: Evolved snapshot of the MADiHR model at $t \approx 70,000 r_g/c$, with identical layout to Fig. 2.2. The MAD state is highly non-axisymmetric and clumpy with a weak ($\eta_j \sim 1\%$) jet. The rest-mass accretion rate and magnetic flux on the horizon reach the MAD state quickly, which was as desired so that we can study a quasi-steady MAD out to large radii over long time periods. The dimensionless magnetic flux Υ_H on the horizon is in agreement with our MADfHR model, showing a disk initial condition with a relatively stronger poloidal field strength still reaches the same MAD state near the BH.

2.3.1 Demonstration of flux accumulation to MAD state

First, we consider a thin radiatively efficient disk threaded by weak large-scale magnetic field. This model, MADfHR/MR, started in the sub-MAD state with $\beta \approx 200$ (a field strength that is ~ 7 times weaker than when the MRI becomes suppressed and ~ 40 times weaker than the final MAD state) so that the MRI operates over long times.

In MADfHR, disk and coronal processes lead to accretion of magnetic flux inward, such that over $t \approx 70,000 r_g/c$ the BH and disk become MAD out to $r \sim 15 r_g$ in the main disk body. Figure 2.2 shows a steady accumulation of flux onto the horizon during the first $\sim 30000 r_g/c$. Movies of the phi-averaged vector potential and the time- r - θ dependence of flux accumulation reveal a faster pile-up of flux at higher disk latitudes via coronal processes, and a slower steady inward transport of flux near the equator by some combination of MRI processes and wind driving. Figure 2.2.1 shows the different stages of the inward flux transport. For detailed physical descriptions in prior explorations of this behavior see, e.g. Rothstein and Lovelace 2008; Beckwith et al. 2009.

Accumulation onto the BH is dominated in the first $5000 r_g/c$ by large-scale MRI ‘channel’-type modes typical of these initial conditions that last until ϕ -symmetry of the poloidal field is lost to parasitic modes, as well as coronal processes in the inner-most disk. Even during this very early evolution there is some separation of net flux passing through the disk from the most dense disk material, development of a two-phase flow, and during the initial transient evolution inside $r \sim 15 r_g$ the field transported from the disk to the horizon leaves behind some extra mass. This separation, as well as reconnection of field near the equator and on the horizon, leads to the remaining matter of the inner disk having a weaker net field and the MRI is under-resolved in this region for about $\sim 20000 r_g/c$. As flux is accumulated into this under-resolved region the effective viscosity rises until the over-dense region is fully accreted and the field in the inner disk is strong enough for the MRI to be resolved once again. Since the accretion rate drops and the strong field in the disk

near the horizon now provides low-order asymmetries previously suppressed by the under-resolved material, the field on the horizon, now also above the MAD limit, can reconnect and push sporadically into the disk. That sporadic reconnection is a behavioral signature of the MAD state near/on the horizon.

In the much longer run, MADfMR becomes MAD out to a radius of $r \sim 18r_g$ by the time $t \approx 183,000r_g/c$. Plenty more magnetic flux exists at larger radii in both MADfMR and MADiMR, and it would presumably contribute to the MAD region of the disk at later times if we continued running the simulations. It is unclear if this slower transport of net flux inward through the main disk body is primarily due to the MRI processes or wind driving.

Though the physics behind the saturation of magnetic flux needs more exploration in future work, it has reached a maximum far below the supply, yet far beyond the initial value. This demonstrates that large-scale magnetic flux can readily accumulate even with $H/R \approx 0.1$ and radiative cooling, and that it saturates at a maximum value like seen in prior MAD simulations.

Fig. 2.4 shows the time and ϕ -averaged rest-mass velocity structure and distinguishes several key features of the accretion flow. This includes showing the jet boundary and the flow stagnation surface (where material has zero radial velocity, moves outward at higher latitudes in the disk, and moves inward at lower latitudes). Most importantly, the plot indicates the time- ϕ -averaged structure of the magnetic field once the inner disk and BH have reached magnetic flux saturation. As with the thicker MAD model plotted similarly in Fig. 6 of McKinney et al. (2012), the evolution of the ϕ -averaged field structure, which we studied in movies of these frames, demonstrate ordered poloidal magnetic flux is easily transported through the disk from large radii through a combination of coronal and disk processes.

2.3.2 Long-term evolution of MAD state

In order to study the thin MAD out to large radii to ensure an accurate quasi-steady radiative efficiency, we next considered the disk having an initially nearly MAD-level of magnetic field. Figure 2.1, and Figures 2.5 and 2.6 show the initial and

evolved quasi-equilibrium state of our high-resolution model that is initially nearly MAD inside $r = 30r_g$. As the accretion flow evolves from its initial state, rotation drives outward angular momentum transport by turbulent magnetic stresses via the MRI as well as by a magneto-centrifugal wind. Mass, energy, angular momentum, and magnetic flux are accreted and ejected at large latitudes, and by $\sim 5000r_g/c$ magnetic stresses balance incoming gas forces so the accretion is MAD out to $r \sim 30r_g$. By the end of the simulation, $t \sim 70000r_g/c$ for MADiHR, the MAD extends to $r \sim 35r_g$.

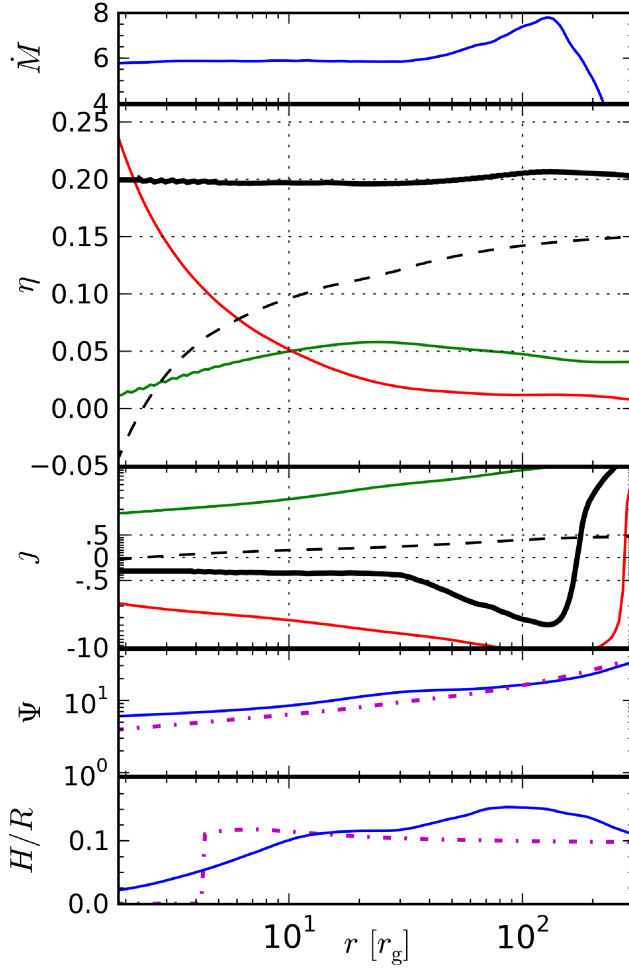


Figure 2.7: (Caption on next page.)

The evolved state is evaluated for specific reported values and time- ϕ -averaged quantities using the period $t = [30000, 70000]r_g/c$. However, a slightly longer period

Figure 2.7: (Figure on previous page.) Time-averaged quantities, averaged over $10000\text{--}70000r_g/c$, as a function of radius. From top to bottom, panels are: Total mass accretion rate (\dot{M}_0 , blue line), energy efficiency (η), specific angular momentum (j), magnetic flux (Ψ), and disk thickness (H/R , $n=1$ in Eq. 2.4, blue line). Plots for η and j show total gas+radiative (black solid), electromagnetic (green), matter (red), and radiation (black dashed) components. Remaining plots show their initial value (magenta dot-dash). The plot of Ψ shows the cumulative net vertical flux including BH and disk contributions (blue). The constancy of \dot{M} , η , j show where the flow has achieved inflow equilibrium. Ψ shows the MAD to non-MAD transition at $r \sim 35r_g$, while throughout the disk $H/R \approx 0.1$ (bound gas), as maintained by cooling. The primary result of this plot is the efficiency panel showing the radiative contribution of $\eta_r \sim 15\%$ with most of emission beyond the standard NT disk model coming from quite close to the photon orbit where the MAD state differs significantly in structure and behavior from the NT disk.

$t = [10000, 70000]r_g/c$ is used for the time-averaged functions of radius plotted in Figure 2.7 to minimize the effects of long-term trends predominantly at larger radii. The time- ϕ -averaged structure is show in Figure 2.5 and shows qualitatively similar behavior to MADfHR regarding the structure of inwardly accumulating magnetic flux and rest mass flow.

The gas+radiative efficiency $\eta \sim 20\%$, and specific angular momentum $j \approx -0.4$ are constant within the MAD/non-MAD transition $r \sim 35r_g$, indicating a quasi-steady MAD state has been reached out to a relatively large radius.

The disk thickness at $r \sim 20r_g$ is regulated by cooling to be $H/R \approx 0.11$ for $n=1$ in Eq. 2.4, $H/R \approx 0.14$ for $n = 2$, density-weighted normalized $H/R \approx 0.13$ (Penna et al., 2012), and thermal thickness of $\bar{h} \equiv \arctan(c_s/v_{\text{rot}}) \approx 0.13$. An accurate measurement of H/R is complicated by the fact that magnetic compression leads to a geometric $H/R \approx 0.05$ near the BH, mass is launched into a broad wind, and vertical disk fluctuations are the same order as H/R . For the ϕ -averaged density profile and including only bound material (i.e. $-u_t(\rho + e_{\text{gas}} + P_g + 2P_b)/\rho < 1$), valid

when comparing with NT, we get $H/R \approx 0.10$, which is our target value we desired for the disk proper. Figure 2.8 shows the time evolution of H/R at four radii for $n = 1$. The same quantities are plotted for MADfHR for comparison in Figure 2.9.

While it is less physically informative than Ψ in evaluating the quantity of magnetic flux present, we refer to values of Υ for comparison to prior work. When only considering the highly ordered dipole magnetic field on the horizon in the MAD state, these quantities are usually very similar in magnitude anyway. Our thin MAD achieves a magnetic flux on the BH of $\Upsilon_H \approx 5$. The stability of Υ_H with time and the presence of plentiful magnetic flux remaining in the disk (see Fig. 2.8, lower panel) indicate that the disk has achieved a balance between magnetic forces and gas forces with a strong magnetic field ($\Upsilon \gg 1$). Thus one expects maximum magnetically-induced deviations from the standard NT thin disk solution.

Large temporal deviations are driven by magnetic flux repeatedly building up on the BH horizon to a level the disk cannot sustain. As soon as a weak point in the disk exists, a non-axisymmetric mode in in-falling matter, gas pressure distribution, or rest-mass, then there is a sudden re-emergence of magnetic flux back into the disk, a process that creates large low-density bubbles in the form of a magnetic prominence. The magnetic flux that is ejected is then processed by turbulence by the outer parts of the disk until being accreted again at which point the process repeats. Figure 2.10 shows one of the most extreme magnetic prominences occurring in the MADiHR simulation.

2.3.3 Radiative Efficiency

We find that nearly as much radiation is released near and inside the ISCO as in the entire rest of the disk, so we calculate the radiative efficiency assuming 100% photon capture within a choice among three radii: the horizon, the photon orbit radius $r \approx 2.4$, and the critical impact parameter radius, $r \approx 4.1$, for which geodesics with any smaller impact parameter intersect the horizon. An estimate of photon capture using ray-tracing from a thin disk gives as much as 30% escape fraction from the photon orbit for equivalent BH spin (see Beckwith et al. 2006),

and more than 70% for $r \approx 4.1$. This suggests using the photon orbit may give the best choice for our simple approximation.

The radiative efficiency is $\eta_r \sim 15\%$ for MADiHR ($< 0.5\%$ lower for MADiMR) when including only radiation from outside the photon orbit. This is about twice larger than the $\eta_r \approx 8\%$ efficiency in standard NT thin disk theory for BH spin $a/M \approx 0.5$. The impact parameter estimate is an extreme, albeit unphysical, limit giving efficiency $\eta_r \sim 9.4\%$. Also unphysical, including all radiation released outside the horizon gives $\eta_r \sim 19\%$. Unbound gas only contributes $\sim 1\%$ to η_r , a smaller relative contribution compared to prior simulations (Penna et al., 2010a; Zhu et al., 2012).

Thus, our thin MAD with $H/R \approx 0.05$ – 0.1 and a radiative efficiency of $\eta_r \approx 15\%$, demonstrates an $\approx 80\%$ deviation from NT. Prior GRMHD simulations of thin disks have had $H/R \approx 0.1$ with 6% deviations (Noble et al., 2009), $H/R \approx 0.06$ with 6% to 10% deviations (Noble et al., 2011), and $H/R \approx 0.07$ – 0.13 with 4% to 5% deviations (Penna et al., 2010a). So despite having similar H/R , our thin MAD has vastly higher deviations from NT.

2.3.4 Jet Efficiency

Some of the horizon magnetic flux reaches into the polar regions leading to a jet efficiency of $\eta_j \approx 1\%$ at $r = 50r_g$ for both MADiHR and MADfHR. A caveat is that the jet within $b^2/\rho > 1$ at $r = 50r_g$ is only resolved by about 7 grid cells. So we check the jet efficiency and resolution on the horizon, where the jet is resolved with more than 12 grid points per hemisphere and still has a jet power of $\eta \approx 1\%$. These horizon jet grid cells are sufficient resolution to capture the force-free behavior of the jet near the polar axes, according to prior resolution studies (McKinney and Gammie, 2004). So the jet efficiency measurement is robust to resolution changes, slight model changes, and what radius it is measured at.

The BH spin and disk rotation drive a magnetized wind with efficiency $\eta_w \approx 4\%$, though at least an additional 1% wind efficiency may be lost to radiation via the very efficient cooling we use as well as lost to the comparatively low resolution

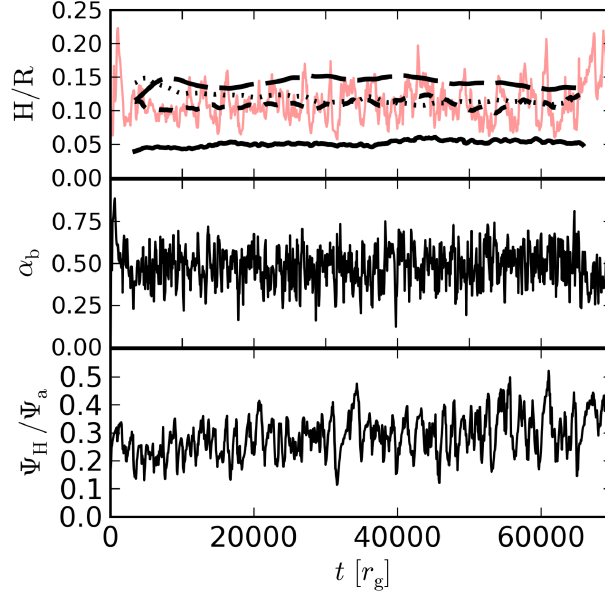


Figure 2.8: Shows temporal evolution of a few quantities for our MADiHR model. The disk scale height H/R is shown in the top panel. We show the temporally-smoothed H/R as plotted for radii R_{ISCO} (solid-black), $15r_g$ (short-dashed), $30r_g$ (dots), and $60r_g$ (long-dashed). The red line is the un-smoothed evolution at $15r_g$ to demonstrate the level of variability. The H/R value is regulated by cooling to be $H/R \sim 0.1$, which is what is achieved for radii just outside the ISCO and out to the inflow equilibrium radius of $r \sim 35r_g$. The middle panel shows the α_b viscosity parameter spatially-averaged over the disk at a radius $10r_g$. The relatively high $\alpha_b \sim 0.5$ is indicative of MADs, implying efficient transport of mass and angular momentum. The third panel shows the ratio of the total magnetic flux threading the BH to the total magnetic flux available at the start of the simulation inside the radius out to which the simulation ultimately reaches at least one inflow time. This shows that the horizon retains only a fraction of the flux available during the course of the simulation, so the quasi-steady state has a horizon-threading flux that has reached saturation.

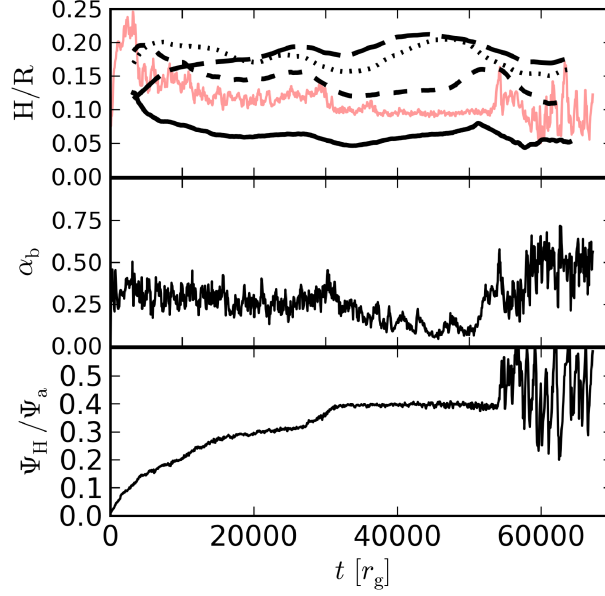


Figure 2.9: Shows temporal evolution of same quantities as Figure 2.8 for our MADfHR model. The disk scale height H/R is shown in the top panel. We show the temporally-smoothed H/R as plotted for radii R_{ISCO} (solid-black), $15r_g$ (short-dashed), $30r_g$ (dots), and $60r_g$ (long-dashed). The red line is the un-smoothed evolution at $10r_g$ to demonstrate the level of variability and show the evolution of the under-resolved dense torus present at early times. $\alpha_b \sim 0.5$ averaged around $8r_g$ drops to low values during that time as expected.

in the jet and highly magnetized wind regions.

The jet and wind contribute only a bit to the total $\eta \approx 20\%$. However, the jet and wind carry nearly as much angular momentum outward as the dense Keplerian disk carries inward. This results in the BH spin-up parameter $s = -j - 2(a/M)(1 - \eta) \approx -0.4$, i.e. the BH is somewhat spinning down (McKinney et al., 2012).

Further, the jet efficiency as a function of H/R is constrained by our thin MAD result. Magnetic compression leads to varying geometric H/R vs. radius, so the more constant thermal thickness $\bar{h} \equiv \arctan(c_s/v_{\text{rot}})$ is used (McKinney et al., 2012). Our thin MAD models have $\bar{h} \approx 0.13$ and older MADs had $\bar{h} \approx 0.5$ (e.g. with geometric $H/R \approx 0.3$ at $r = 20r_g$) or $\bar{h} \approx 1.5$.

Prior thick MAD simulations found that the saturated magnetic flux on the BH given by Υ_H is roughly constant vs. BH spin. That data showed a slight tendency to peak at $a/M \sim 0.5$, but this is probably intrinsic to the initial disk conditions or due to intrinsic errors that suggest $a/M \sim 0$ could be the peak as well (McKinney et al., 2012; Tchekhovskoy et al., 2012). The thick MAD simulations of moderate thickness show a clear asymmetry in the Υ_H vs. spin for positive vs. negative spin that is consistent with the asymmetry in jet efficiency vs. spin. So we do not try to fit the peak in Υ_H being at $a/M \sim 0.5$, but we capture the asymmetry. We also capture the fact that this spin asymmetry is seen to go away as the disc becomes even thicker.

Combining more than 25 different thicker MAD models with our new thin MAD model, a rough fit of the jet efficiency is given by

$$\eta_j \approx 400\% \omega_H^2 \left(1 + \frac{0.3\omega_H}{1 + 2\bar{h}^4}\right)^2 \bar{h}^2, \quad (2.17)$$

where $\omega_H \equiv a/r_H$, which assumes steady activation of a Blandford and Znajek (1977) jet. The $\eta_j \propto \bar{h}^2$ scaling is required (compared to $\propto \bar{h}$) to reach our thin MAD with $\eta_j \approx 1\%$. That $\eta_j \propto (H/R)^2$ is consistent with S7.1 of Penna et al. (2010a) who analytically found $\Upsilon_H \propto (H/R)$, and with Meier (2001) who argued that $\eta_j \propto (H/R)^2$.

In our model we fit to jet efficiency rather than jet power since this is easily

compared to observations of stellar and super-massive BH systems, and because rest-mass density can be scaled to any value in these simulations. However, our formula is roughly consistent with what is expected based upon the BZ formula for jet power $\propto \Upsilon_{\text{H}}^2 \Omega_{\text{H}}^2$. Models with $\bar{h} \approx 0.5$ and $a/M = 0.5$ gave $\eta_{\text{j}} \sim 20\%$ and $\Upsilon_{\text{H}} \approx 13$. Our thin MAD has $\Upsilon_{\text{H}} \approx 5$, so the BZ formula suggests we should get $\eta_{\text{j}} \approx 3\%$ while we got $\eta_{\text{j}} \approx 1\%$. Why the factor of three difference?

First, Υ measured on the BH is not relevant to the BZ jet. One cannot use Υ_{H} with $\eta_{\text{j}} \propto \Upsilon_{\text{H}}^2$, because in general (and as found in thicker MAD models) magnetic flux in the jet is a fraction of Υ_{H} and the jet only partially covers the rotating BH's surface. Instead, the magnetic flux passing through the jet is what is relevant to the jet power. The $\bar{h} \approx 0.5$ model had $\Upsilon_{\text{j}} \approx 10$, while our model has $\Upsilon_{\text{j}} \approx 4$. These are significantly different from the magnetic flux over the entire horizon. This still implies we should have $\eta_{\text{j}} \approx 3\%$ for consistency with the BZ expectation.

Second, the BZ formula fails to account for the disk covering a significant part of the potential power output (McKinney, 2005). The disk at the equator gets in the way, even for MADs (especially at lower spin when less magnetic compression occurs). However, most of the BZ power would be at the equator where the Poynting flux peaks. The disk chops-off this peaked part of the Poynting flux for the jet, giving some of it to the wind. Some of that BZ power is never produced in the first place due to the heavy mass-loading by the disc. A better model of that disk part that connects to the horizon is the Gammie (1999) model of a thin magnetized disc. In that case, Υ locally in the disk is much less than over the entire horizon, so the Gammie (1999) model predicts much less than BZ for extraction of energy. One cannot just fit η_{j} vs. Υ_{H} and expect it to match BZ.

Third, we have defined the jet arbitrarily as where $b^2/\rho > 1$. The wind is defined as the rest of the non-radiative flux that adds up to the total efficiency. For our thin MAD, this is 4% (i.e. 20%-1%-15%). The wind efficiency is partially directly due to the disk rotation, but some of the wind efficiency derives from magnetic flux threading the BH that passes into the disk leading to a BH-spin-driven wind. Some of this BH-spin-driven wind absorbs what would have otherwise (without a disk)

become the jet and can account for another missing 2%, giving a total BZ-like efficiency matching expectations. If this were the sole effect in comparison to the thicker MAD models, this would suggest that thin MADs may have more powerful winds per unit jet power relative to thick MADs.

Fourth, the jet efficiency for the $\bar{h} \approx 0.5$ $a/M = 0.5$ model is a peak among all the otherwise identical models with different BH spins. Given how much the results vary for slight changes in the model setup (like initial magnetic field strength), the $\eta_j \approx 20\%$ could easily have been $\eta_j \approx 10\%$ within systematic errors. Then there would be no discrepancy between our formula and the BZ approximation.

So our Eq. (2.17) is not supposed to be derived from BZ because the BZ-driven process creates both a “jet” and a “wind”, while we have defined the jet by that part which would be capable of becoming relativistic. So in that sense, our formula is useful in application to real jets instead of a test of whether the theoretical BZ extraction efficiency applies to the simulation data. However, only direct observational comparisons without ad hoc definitions will test the validity of these simulations being applicable to real systems. The fitting formula is just a useful guide.

2.3.5 Resolution

We test the resolution of our simulations using convergence quality factors for the MRI ($Q_{\theta\phi,\text{MRI}}$; number of grid cells per MRI wavelength in each direction) and turbulence ($Q_{r\theta\phi,\text{corr}}$; number of cells per turbulence correlation length in each direction) (Shiokawa et al., 2012; Hawley et al., 2011; McKinney et al., 2012; Hawley et al., 2013; McKinney et al., 2013, 2014). For our high resolution runs, MADiHR (MADfHR), at $r = 12, 30r_g$ centered on the equatorial flow, we have $Q_{\theta,\text{MRI}} = 160, 55$ ($Q_{\theta,\text{MRI}} = 88, 18$) with a weighting of $\sqrt{\rho b^2}$ and we have $Q_{\phi,\text{MRI}} = 120, 100$ ($Q_{\phi,\text{MRI}} = 79, 77$) with a weight of ρ . Weighted averages are computed for the numerator and denominator separately before taking the ratio to get Q . The purely density-weighted values represent a stricter constraint on whether we have sufficient resolution (because MADs have strong fields mostly outside the dense region, and

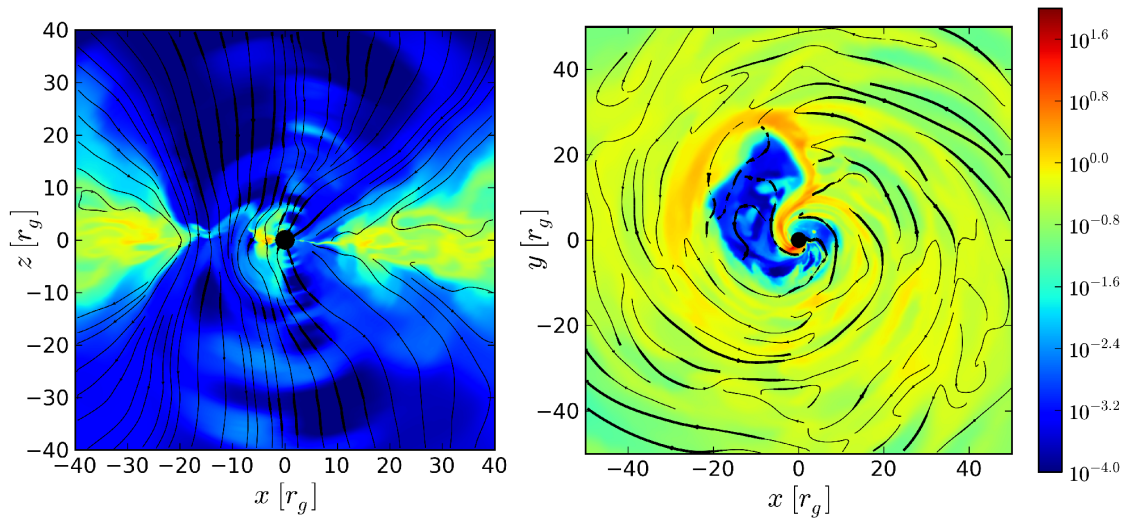


Figure 2.10: Plotted as in the top frames of Fig. 2.6 is a snapshot of MADiHR at $t = 31568r_g/c$ when the disk experiences an extreme eruption of magnetic flux from the BH horizon. A large magnetic flux tube creates a low-density cavity in the disk before it is partially blended with disk material by the magnetic Rayleigh-Taylor instability. Such prominences occur frequently in the MAD state.

the external stresses are important to whether transport occurs). These are plotted as a function of radius in Figure 2.11. Resolution of turbulent structures in rest-mass and magnetic energy density are evaluated at four radii $r = \{r_H/r_g, 4, 8, 30\}r_g$. For MADiHR, rest-mass correlation values are, at each radius respectively, $Q_{r,corr} \sim 6, 10, 14, 14$, $Q_{\theta,corr} \sim 40, 35, 31, 34$, and $Q_{\phi,corr} \sim 6, 7, 8, 11$. Correlation values for magnetic energy density are, similarly, $Q_{r,corr} \sim 6, 12, 17, 15$, $Q_{\theta,corr} \sim 34, 33, 29, 36$, and $Q_{\phi,corr} \sim 8, 9, 12, 16$.

For MADfHR, calculated for the disk once the BH has reached the MAD state, rest-mass correlation values are, at each radius respectively, $Q_{r,corr} \sim 6, 10, 14, 14$, $Q_{\theta,corr} \sim 3, 29, 28, 32$, and $Q_{\phi,corr} \sim 7, 9, 11, 13$. Correlation values for magnetic energy density are, similarly, $Q_{r,corr} \sim 6, 12, 16, 15$, $Q_{\theta,corr} \sim 5, 28, 30, 31$, and $Q_{\phi,corr} \sim 7, 9, 12, 14$.

These MRI and turbulent quality factors show convergence according to strict application of conventional tests. Of course there could be behavior characteristic of the MAD state that eludes tests for convergence in accretion physics so far devised. We therefore directly convergence tested our results by performing simulations of each setup with three resolutions. The qualitative structure of the disk in the MR and HR simulations are the same, but the lower resolution in MR allowed us to run these simulations for significantly longer. The nature of magnetic flux accumulation is the same, but the longer MR simulations ultimately become magnetically arrested to larger radius, $r \sim 18r_g$ in MADfMR compared to only $r \sim 15r_g$ in MADfHR. A difference of only $\sim 0.5\%$ in radiative efficiency between MADiMR and MADiHR indicates very good convergence in our quantity of interest. We find only small (typically $\sim 10\%$ or less) differences between our MR and HR simulations for the other quantities reported which characterize the accretion flow. For instance, the jet power differs by only $\sim 50\%$ between MADiMR and MADiHR, unsurprising since $\Upsilon_H \approx 5$ for both. Low resolution ‘testing’ simulations were largely in qualitative agreement, but with some Q ’s indicating lack of convergence.

Figures 2.8 and 2.11 show values of the α_b viscosity parameter, dominated by the magnetic stress. We find $\alpha_b \sim 0.5$, as consistent with resolved disks in prior

MAD simulations. The effective viscosity $\alpha_{\text{b,eff}}$, corresponding to a measurement of the actual inflow rate indicated by an α parameter, is much larger than α_{b} due to enhanced inflow caused by external torques driven by low-density highly-magnetized material that introduces large-scale stresses on the more dense inflow. α_{b} does not reflect the effective viscosity in large part because the ρ weighting in calculating α_{b} predominantly excludes the flux tubes that drive the Blandford-Payne-type transport of angular momentum. The dense parts of the disk lose angular momentum by running into these flux tubes on their orbit. One can think of the MAD, then, as a two-phase flow where MRI drives turbulence, still, in small dense clumps, but the large-scale evolution of the disk, at scales where the MRI is quenched by magnetic field strength, is dominated by magnetic-Rayleigh-Taylor and wind/jet processes.

2.3.6 Power-law Fits for Radial Dependence

We now consider radial power-law fits (of the form $f = f_0(r/r_0)^n$) for quantities associated with the disk structure and flow, plotted in Figure 2.12, for MADiHR. The fits to disk quantities are performed as in McKinney et al. (2012) between radii $r = 12r_g$ and $r = 30r_g$ for both our high resolution models. The profiles for MADiHR (MADfHR) are $\rho \propto r^{-0.4 \pm 0.1}$ ($\propto r^{-0.8 \pm 0.2}$), $p_g \propto r^{-1.5 \pm 0.1}$ ($\propto r^{-1.8 \pm 0.1}$), $|v_r| \propto r^{-1.6 \pm 0.06}$ ($\propto r^{-0.8 \pm 0.2}$), $|v_\phi| \propto r^{-0.38 \pm 0.01}$ ($\propto r^{-0.49 \pm 0.01}$), $|b_r| \propto r^{-1.4 \pm 0.07}$ ($\propto r^{-1 \pm 0.1}$), and $|b| \propto r^{-1.2 \pm 0.05}$ ($\propto r^{-0.89 \pm 0.02}$).

The MADiHR fits are more representative of a steady-state MAD solution, because the disk in MADiHR is actually magnetically arrested over all radii used for fitting and the model is in quasi-equilibrium out to large radii. Our thin disk has a somewhat shallower radial density profile than prior MAD models, but are otherwise consistent. To obtain a density profile accurate to large radii, much longer-run simulations would be required. The overall fits are consistent with $p_g \propto r^{-1.5}$ and $|b| \propto r^{-1}$ expected for accretion disks, while the shallow density profile could be connected with the stronger wind (relative to the jet) compared to thicker MAD simulations.

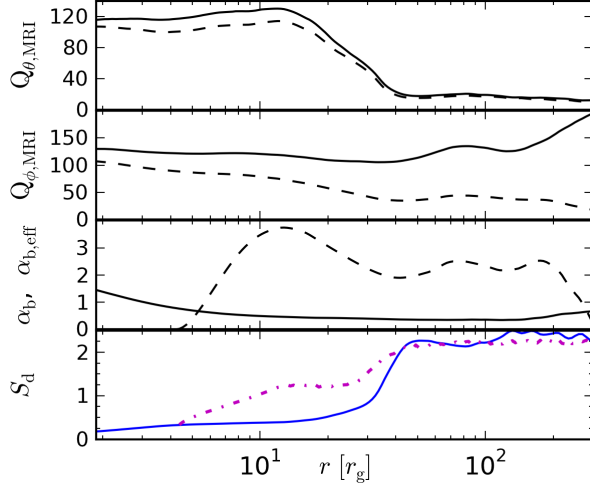


Figure 2.11: MRI quality factors indicating time- ϕ averaged resolution, viscosity of the disk, and vertical MRI half-wavelengths per disk scale height (S_d , blue line) are plotted as a function of radius. Q factors indicated the number of grid cells per critical MRI wavelength, averaged with weight $\sqrt{\rho b^2}$ (solid lines) and ρ (short dashed) across the disk where $b^2/\rho < 0.5$. The third panel shows the viscosity parameter α_b (solid line) and the effective viscosity calculated via the mass accretion rate (short dashed). The magnetic evolution of the disk is well resolved and leads to a high viscosity as measured by local stresses, α_b , and the rate of mass inflow $\alpha_{b, \text{eff}}$. The magenta dot-dash line represents the value of S_d at $t=0$ and the time-average is blue-solid.

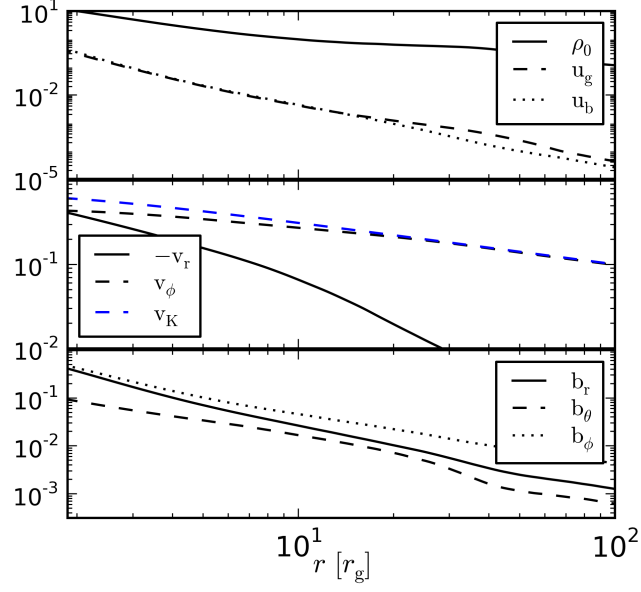


Figure 2.12: Several quantities characterizing the accretion flow in MADiHR are plotted as a function of radius. The top panel shows the density profile ρ (solid), the internal gas energy u_g (dashed), and magnetic energy density u_b (dotted). The inner disk, that has reached the MAD state, has $u_g \sim u_b$ indicating equipartition is achieved even within the dense parts of the disk. The middle panel includes the disk radial velocity, azimuthal velocity, and Keplerian velocity (v_r , solid; v_ϕ , black-dashed; v_K , blue-dashed, respectively). The final panel shows the radial profiles of each component of the comoving magnetic field, $b_{r,\theta,\phi}$, in solid, dashed, and dotted lines respectively. The density is shallower than thicker disk solutions, the disk is fairly Keplerian, and the magnetic field falls off as expected for accretion disks.

2.4 Summary and Conclusions

We have performed fully 3D GRMHD simulations of radiatively efficient thin accretion disks seeking to maximize the magnetically induced deviations from NT thin disk theory. We first demonstrated that even in thin disks, after a time $183,000r_g/c$ and out to $r \sim 18r_g$, magnetic flux readily advects inward and builds-up to a MAD level (for which accumulation results in magnetic forces pushing out balancing against gas forces pushing in). This occurs despite possible outward magnetic diffusion through the disk.

Our simulation that is MAD out to $r \sim 35r_g$ after $70,000r_g/c$ has a radiative efficiency of $\eta_r \approx 15\%$. This is $\approx 80\%$ higher than the standard NT thin disk value of $\eta_{\text{NT}} \approx 8\%$ and is as if the disk were a standard NT thin disk but with $a/M \approx 0.9$. BH X-ray binaries have $L/L_{\text{Edd}} \sim 0.1$ in the high-soft state (Kulkarni et al., 2011), for which the NT model gives $H/R \lesssim 0.02$ near the BH. Prior non-MAD simulations suggest deviations scale with H/R (Penna et al., 2010a), so typical thin MAD deviations might be conservatively $\sim 20\%$. Such a magnitude of deviations could significantly impact BH spin measurements, such as in Noble et al. (2011) who found 6% deviations lead to a BH with $a/M = 0$ giving a spectrum like NT but with $a/M \approx 0.3$. However, it is unclear into what form the energy would be dissipated. Zhu et al. (2012) found that emission from near the ISCO is mostly high-energy, but more physics (e.g., dissipation-radiation energy balance, optical depth effects, BH photon capture) is required for BH spin fitting (Kulkarni et al., 2011). We plan to obtain spectra via post-processing (Zhu et al., 2015; Narayan et al., 2016). Also, clumpy rest-mass distribution in thin MAD flows may help to explain spectra from AGN (Dexter and Agol, 2011) and BH X-ray binaries (Dexter and Quataert, 2012).

It is not a new idea that X-ray binaries in the low-hard (LH) state supply enough magnetic flux to the BH to enable BZ-type powering of an observable jet by being geometrically thick, and that the jet quenches when the disk collapses to become thin in the high-soft state. For instance, plunging material inside the ISCO may enhance the flux on the BH in the low-hard state only, even in sub-MAD disks

(Reynolds et al., 2006). However, these ideas generally propose transition mechanisms in which the jet switches between being either powered or not, depending on disk state. Our model does not require a special mechanism for the LH state.

Radiatively inefficient flows have $H/R \approx 0.4$ (Narayan et al., 2012). Our fitting formula Eq. (2.17) suggests that jet power in the MAD state can drop by $\gtrsim (0.4/0.02)^2 \sim 400$ (or drop by $\gtrsim (0.4/0.01)^2 \sim 1600$ for 4U 1957+11 if at $L/L_{\text{Edd}} \approx 0.06$) when undergoing hard-to-soft state transitions. This implies that the observed jet quenching in BH X-ray binaries (Russell et al., 2011) can occur despite the presence of a large-scale MAD-level magnetic field in both disk states. Such hard-to-soft transitions may also be applicable to tidal disruption events at late times (Tchekhovskoy et al., 2014). The MAD state could be necessary to explain powerful jet systems (Zamaninasab et al., 2014; Mocz and Guo, 2015), while the thermodynamically determined disk thickness may also play an important role in setting just how much magnetic flux a MAD has. Even thinner disks than studied here would be implied to have $\Upsilon_{\text{H}} \propto H/R$ and so could have much weaker magnetic flux and much weaker jets rather than being independent of the disk state.

Acknowledgments

We thank Ramesh Narayan, Jack Steiner, Roman Gold, Peter Polko, Alexander Tchekhovskoy, and Eliot Quataert for discussions. We acknowledge NASA/NSF/TCAN (NNX14AB46G), NSF/XSEDE/TACC/Stampede (TG-PHY120005), NASA/Pleiades (SMD-14-5451), and UMD Deepthought2.

Chapter 3: General Relativistic Radiation Magnetohydrodynamic Simulations of Thin Magnetically Arrested Disks

Abstract

The classical, relativistic thin-disk theory of Novikov and Thorne (NT) predicts a maximum accretion efficiency of 42% for an optically thick, radiatively efficient accretion disk around a maximally spinning black hole (BH). However, when a strong magnetic field is introduced to numerical simulations of thin disks, large deviations in efficiency are observed, in part due to mass and energy carried by jets and winds launched by the disk or BH spin. The total efficiency of accretion can be significantly enhanced beyond that predicted by NT but it has remained unclear how the radiative component is affected. In order to study the affect of a dynamically relevant large-scale magnetic field on radiatively efficient accretion, we have performed numerical 3D GRRMHD simulations of a disk with scale height to radius ratio of $H/R \sim 0.1$ around a moderately spinning BH ($a = 0.5$) using the code HARMRAD. We use fully global simulations with different numerical grids and resolutions to measure the jet, wind, and radiative properties of a magnetically arrested disk (MAD) that is kept thin via self-consistent radiative transport using the M1 closure scheme. Our fiducial disk is MAD out to a radius of $\sim 17R_g$ and the majority of the total $\sim 13\%$ efficiency of the accretion flow is carried by a magnetically driven wind. We find that the radiative efficiency is slightly suppressed compared to NT, contrary to prior GRMHD simulations with an *ad hoc* cooling function, but it is unclear how much of the radiation and thermal energy trapped in the outflows could ultimately escape.

3.1 Introduction

Black hole accretion disks are present in Active Galactic Nuclei (AGNs), X-ray binaries, gamma-ray bursts (GRBs) and tidal disruption events (TDEs) and are able to convert gravitational potential energy and BH spin energy into radiation, jets and winds through the stresses induced via the magnetorotational instability (MRI) (Balbus and Hawley, 1991, 1998a), magnetic field threading the disks (Blandford and Payne, 1982) and magnetic field threading the black hole (BH) (Blandford and Znajek, 1977). Novikov and Thorne (1973b) developed a general relativistic model for thin disks which has been successfully applied to understand many astrophysical systems. In this model it is assumed that all energy carried away from the disk is radiation. In addition, it is assumed that radiative emission ceases inside the inner-most stable circular orbit (ISCO) where stresses in the NT model disappear. However, Gammie (1999) and Krolik (1999) demonstrated that additional stress inside the ISCO can increase the gravitational potential energy converted by the disk.

Another way to increase the conversion efficiency of a BH accretion disk is to increase the magnetic stress within the disk by making the field dynamically important. If the disk piles up magnetic flux on the BH horizon and in the disk until the MRI is quenched and the magnetic forces pushing out balance gas forces pushing in, no more magnetic flux can be transported inward. This is the so called magnetically arrested disk (MAD) state (Narayan et al., 2003), which has been shown to maximize jet power. GRMHD simulations of thick disks in the MAD state have found accretion efficiencies as high as 30% for a black hole with $a/M=0.5$ and 140% for a black hole with $a/M=0.99$ (Tchekhovskoy et al., 2011). Tchekhovskoy and McKinney (2012) studied the differences in the jet power of prograde and retrograde black holes and found accretion efficiencies of up to $\sim 300\%$ for the prograde case and $\sim 80\%$ for the retrograde case, for a black hole with $|a/M|=0.9375$. These simulations were the first to demonstrate that the amount of magnetic flux threading the horizon and inner disk in the MAD state is determined by the accretion state

alone, not the initial magnetic conditions of the simulations, so long as sufficient large-scale flux is available to the disk.

GRMHD simulations of non-MAD thin disks (untilted and tilted) have found roughly 10% of deviation of the accretion efficiency compared with the expected value from the NT73 model (Shafee et al., 2008; Noble et al., 2009, 2010; Penna et al., 2010a; Morales Teixeira et al., 2014) where this difference has been associated with the amount of vertical magnetic flux that threads the black hole and disk.

Chapter 2 (Avara et al., 2016) built upon prior numerical work to study MAD disks in the thin, radiatively efficient Sub-Eddington regime. We were able to demonstrate the self-consistent inward transport of magnetic flux by a thin disk thereby saturating into the MAD state, and characterized the radiation, wind, and jet efficiencies, disk structure, and jet power in such a system. We found that a sub-Eddington, moderately thin disk can be as much as twice as radiatively efficient as the NT model would predict, with an even greater total efficiency. However, in Chapter 2 we made use of an *ad hoc* cooling function to maintain a particular disk state, and large unknowns in converting the cooling in those simulations to the dissipation of a real system called for more realistic numerical experiments which include self-consistent radiative transport and proper ray-tracing. The present work provides that next step.

In this chapter we study the accretion efficiency of a thin disk in the sub-Eddington limit with half-height (H) to radius (R) of $H/R \approx 0.1$ around a black hole with dimensionless spin (a/M)=0.5 that reaches the MAD state, potentially maximizing accretion efficiency. We compare our values with the results from the simulation MADiHR from Chapter 2 (Avara et al., 2016), that used an ad-hoc cooling function to control the scale-height, in order to understand how radiation affects the jet and wind efficiencies. Here we alternatively make use of the GRRMHD code HARMRAD (McKinney et al., 2014) which includes radiative transport self-consistently and solves the GRRMHD equations using the M1 closure for radiation.

The structure of the chapter is as follows: the methodology and numerical setup are presented in §3.2, results are presented in §??, and in §?? we present our

conclusions and look forward.

3.2 3D GRRMHD thin disk model

We start our simulations with an accretion disk around a black hole with $M_{BH}=1M_{\odot}$ and spin $a/M=0.5$ where the initial conditions of our disk follows the NT73 solution and the density was tuned in order to have a quasi steady-state accretion flow with $\dot{M}=0.4\dot{M}_{Edd}$ where \dot{M}_{Edd} is the Eddington accretion rate defined as $\dot{M}_{Edd} = (1/\eta_{NT})L_{Edd}/c^2$. η_{NT} is the NT73 accretion efficiency and L_{Edd} is the Eddington luminosity defined as

$$L_{Edd} = \frac{4\pi G M c}{\kappa_{es}} \approx 1.3 \times 10^{46} \frac{M_{BH}}{10^8 M_{\odot}} \text{ergs}^{-1}, \quad (3.1)$$

where for our case we have $\eta_{NT} \approx 8.6\%$ and $\dot{M}_{Edd} \approx 1.68 \times 10^{18} \text{g s}^{-1}$.

We initialized our simulations with a Keplerian disk that has a density profile given by:

$$\rho(r) = \rho_0 e^{-z^2/(2H^2)}, \quad (3.2)$$

with

$$\rho_0 = \Sigma/(2H), \quad (3.3)$$

where Σ is the surface density, H the height, and their expressions are given by NT73 solution for the inner (radiation-pressure dominated) region (equation 5.9.10 in NT73).

The initial radial velocity profile of the disk is given by:

$$V_r = \alpha_{visc} (H/R)^2 r |\Omega|, \quad (3.4)$$

where Ω is the angular velocity and α_{visc} was set to 0.5.

Due to the poor resolution in the radial direction at large radii we have truncated the disk at $R_{tr1}=120M$, tapered off by an exponential profile for the density,

$$\rho'(r) = \rho(r)e^{(-r/R_{tr1})+1}. \quad (3.5)$$

The total ideal pressure is given by $P_{tot} = (\Gamma_{tot} - 1)u_{tot}$, where $\Gamma_{tot}=4/3$, u_{tot} is the internal energy density, and the gas pressure was randomly perturbed at the 10% level to seed the MRI. The disc is initialized with an atmosphere of density $\rho = 10^{-5}(r/R_g)^{-1.1}$, gas internal energy density $e_{gas} = 10^{-6}(r/R_g)^{-5/2}$, and the radiation energy density and flux were set by the local thermodynamic equilibrium (LTE) and flux-limited diffusion approximation (McKinney et al. 2014) with a negligible radiation atmosphere. We set the rest mass and internal energy densities to zero near the black hole within the jet and near the axis, corrected by the numerical ceilings of $b^2/\rho=300$, $b^2/e_{gas}=10^9$ and $e_{gas}/\rho=10^{10}$.

The magnetic field in the disk is large scale and poloidal only, with open field lines and a transition to monopolar at R_{tr2} . For $r < R_{tr2}$ the ϕ component of the vector potential is given by:

$$A_\phi = MAX((r + 5)^\nu - 10^{40} - 0.02, 0)(\sin \theta)^{1+h}, \quad (3.6)$$

with $\nu=1$ and $h=4$. For $r \geq R_{tr2}$ the field transitions to monopolar using a vector potential given by

$$A_\phi = MAX((R_{tr2} + 5)10^{40} - 0.02)(\sin \theta)^{1+h(R_{tr2}/r)}. \quad (3.7)$$

Our field is normalized inside one MRI wavelength per half-height H giving a ratio of gas+radiation pressure to average magnetic pressure of $\beta \approx 10$ ($\beta = (p_{gas} + p_{rad})/p_{mag}$). In order to investigate the effects of the transition to monopolar field, we have choosen $R_{tr2}=120R_g$ for our simulations RADHR and RADLR and $R_{tr2}=200R_g$ for our simulation RADvHR. The motivation for the changing the field transition radius was to try to reach a MAD state out to large radii.

For the radiation transport processes, we have assumed that our initial disk has solar abundance with mass fractions of hydrogen, helium and metals equal to $X=0.7$, $Y=0.28$ and $Z=0.02$, which gives an electron fraction of $Y_e = (1 + X)/2$

Table 3.1: Grid resolution

Simulation	Polar grid	N_r	N_θ	N_ϕ	$T_{stop}(R_g/c)$
MADiHR	Avara et al. (2016)	192	96	208	70,000
RADLR	McKinney et al. (2012)	128	64	32	40,000
RADHR	McKinney et al. (2012)	128	128	64	40,000
RADvHR	This work	128	128	64	18,000

and mean molecular weight of $\bar{\mu} \approx 0.62$. The expressions for the electron scattering, absorption-mean energy, bound-free, and free-free opacities are the same used by [McKinney et al. \(2015b\)](#).

3.2.1 Numerical grid

In this section we will describe the two grids used in our simulations RADHR, RADLR, and RADvHR. For simulations RADHR and RADLR we used the same grid as in [McKinney et al. \(2012\)](#). Our grid for RADvHR is similar, but with important modifications that will be described below. In all of our simulations we have adopted the same boundary conditions as [McKinney et al. \(2012\)](#), where the radial grid has N_r cells spanning from $R_{in} \sim 1.5R_g \sim 0.084R_h$ (where R_h is the horizon radius) to $R_{out}=10^5R_g$ with cell size increasing exponentially until r_{break} and then increasing hyper-exponentially. Outflow radial boundary conditions were adopted. The θ grid has N_θ cells spanning from 0 to π and the grid of our simulation RADvHR has been properly adjusted for a disk with $H/R=0.1$ concentrating mostly of the cells in the disk. The ϕ grid has N_ϕ cells spanning uniformly from 0 to 2π with periodic boundary conditions. The resolutions for the radial, θ and ϕ directions and the grid type for each of our simulations are given in Table 3.1.

In the results section we will show that in our simulation RADHR the MAD state has only built up until $R=17R_g$ and for this reason we have modified the θ grid in order to better resolve the MRI and raise the efficiency of the transport of

magnetic flux to try to reach MAD state beyond $17R_g$. Our simulation RADvHR has only been run up to a time $18,000R_g/c$ due to the limitations of computer resources and algorithmic improvements in HARMRAD will aid in feasibly running this simulation substantially longer.

Before we introduce the new equations for the new θ grid, we must define some new variables:

$$T_r(x) = \frac{e^{-1/x}}{e^{-1/x} + e^{-1/(1-x)}}, \quad (3.8)$$

and

$$Trans(X, L, R) = \begin{cases} 0.0 & \text{if } x \geq L, \\ 1.0 & \text{if } x \geq R, \\ T_r\left(\frac{x-L}{R-L}\right) & \text{if } L < x < R. \end{cases} \quad (3.9)$$

To concentrate most of the cells in the disk, the expressions for S_0 and S_2 to control the cells at small, middle and large radii were changed. In our case S_0 was changed to:

$$S_0(r, r_a, r_b) = Trans(\log(r), \log(r_a), \log(r_b)), \quad (3.10)$$

where the objective of S_0 is to control the cell size at middle and large radii. The expression for S_2 has been changed and in our case is given by:

$$S_2(r, r_a, r_b) = 1 - S_0(r, r_a, r_b), \quad (3.11)$$

where this expression for S_2 controls the cell size at small and middle radii. Then the new expression for h_2 is given by:

$$h_2 = h_3 S_2(r, 40, 200) + S_0(r, 40, 200)(h'_2(r) S_2(r, 200, 500) + h'_2(500) S_0(r, 200, 500)), \quad (3.12)$$

where

$$h'_2(r) = h_3 + \left(\frac{r - r_{sj3}}{r_{0j3}} \right)^{n_j}, \quad (3.13)$$

is the same equation for h_2 in [McKinney et al. \(2012\)](#). The original equation for θ_2 has also been modified and in our case is given by

$$\theta'_2 = \theta_2^a S_0(r, 20, 40) + \theta_2^b S_0(r, 20, 40), \quad (3.14)$$

where θ_2^a and θ_2^b are the original expression for θ_2 and T_2 presented in [McKinney et al. \(2012\)](#).

Similar to the other expressions, the original expression for h_0 was modified to

$$h_0(r) = h_3 S_2(r, 40, 200) + S_0(r, 40, 200)(h'(r)_0 S_2(r, 200, 500) + h'(500) S_0(r, 40, 200)), \quad (3.15)$$

where the expressions for h' is now given by

$$h'(r) = 2 - Q_j(r/r_{1j})^{-n_{j2}[(1/2)+(1/\pi) \arctan(r/r_{0j}-r_{sj}/r_{0j})]}. \quad (3.16)$$

The expression for θ_1 in our case is given by

$$\theta_1 = T_0 S_2(r, 20, 200) + \theta'_2 S_0(r, 20, 200), \quad (3.17)$$

where T_0 is the original expression from [McKinney et al. \(2012\)](#).

Finally the expression for θ is

$$\theta = \theta_2^a S_2(r, 1, 10) + S_0(r, 1, 10) \theta_1. \quad (3.18)$$

The parameters for the polar grid of each of our simulations are listed in [3.2](#).

As in [McKinney, Tchekhovskoy & Blandford \(2012, 2013\)](#), [McKinney et al. \(2014\)](#) and [McKinney, Dai & Avara \(2015\)](#), we tested the convergence quality factors for the MRI in the θ and ϕ directions ($Q_{\theta, MRI}$, $Q_{\phi, MRI}$) and turbulence ($Q_{nlm, corr}$) measuring, respectively, the number of grid cells per MRI wavelength in the θ and ϕ directions and the number of correlation wavelengths in the radial, θ and ϕ directions. The values were averaged over the period 30,000-40,000 R_g/c and over θ

and ϕ at $r=10R_g$, which represents the non-choked part of the accretion flow. Our simulation RADHR has $Q_{\theta,MRI} \sim 110$, $Q_{\phi,MRI} \sim 13$ and $Q_{nlm,corr} \sim 11$, 13 and 4 respectively. The value of $Q_{nlm,corr}$ in the ϕ direction shows that the turbulence is not well resolved since the previous works mentioned above have shown that 6 or more cells are required to resolve the turbulence, but even being slightly under resolved we can still identify some physical effects as we will discuss in the next sections. We have also measured the disk thickness per unit MRI wavelength, S_d (where for $S_d < 0.5$ the MRI is suppressed). Initially for our simulation RADHR, $S_d \sim 0.9$ and the time averaged flow has $S_d \sim 0.26$ out to $r \sim 17R_g$. The simulation RADLR has $Q_{\theta,MRI} \sim 21$, $Q_{\phi,MRI} \sim 8$ and $Q_{nlm,corr} \sim 12$, 8, 3 where the values were time averaged over $30,000\text{--}40,000R_g/c$. Our simulation RADvHR at its end has $Q_{\theta,MRI} \sim 56$, $Q_{\phi,MRI} \sim 13$ and $Q_{nlm,corr} \sim 15$, 22, 7 and the MAD state built up to $13R_g$. As we can see our simulation RADLR is underresolved and will be used for reference to study resolution effects of the flow at late times and check how the MAD state builds up while the turbulence in our simulation RADvHR was much better resolved.

Table 3.2: Polar grid Parameters

Simulation	n_0	c_2	n_2	r_s	r_0	h_3	r_{0j3}	r_{sj3}	n_{j1}	r_{1j}	r_{oj}	r_{sj}	Q_j	n_θ	h_θ	r_{sj2}	r_{0j2}	r_{break}
RAD(HR,vHR)	1	1	6	40	40	0.1	40	0	0.5	30	30	40	1.8	5	0.1	8	3	200
RADLR	1	1	6	100	60	0.1	40	0	0.7	30	30	40	1.7	5	0.1	5	2	300

3.2.2 Diagnostics

The diagnostics evaluated in this study are identical to those used in Chapter 2 save for a few cases, so we do not reproduce the majority of the definitions here. However, unless otherwise stated, the half-angular thickness H normalized by the radius R is calculated with equation 2.4 in this study as before, but with $n = 2$ unless otherwise specified.

With the addition of the radiation fluid, we introduce several new characteristic

quantities. In order to obtain the optical depth in the radial direction for each instant in time we compute:

$$\tau = \int \rho \kappa_{tot} dl, \quad (3.19)$$

where $dl = -f_\gamma dr$, $f_\gamma = u^t(1 - (v/c) \cos \theta)$, where for large radii $(v/c) \sim 1 - 1/(u^t)^2$, $\theta=0$ and the integral is carried out from $r_0=3,000$ (to consider only transient material that would contribute to the optical depth, a radius where the disk wind has reached) to r in order to obtain $\tau_t(r)$. In the angular direction $dl = f_\gamma r d\theta$, $\theta = \pi/2$ and the integral is carried out from each polar axis towards the equator to obtain $\tau_\theta(\theta)$. The radiation photosphere is defined as $\tau_r=1$, which is an upper limit to the radius of the photosphere for an observer since radiation can escape.

Finally the radiative luminosity is given by:

$$L = - \int dA_{\theta\phi} R_t^r, \quad (3.20)$$

where the luminosity is measured at $r = 400R_g$ where only the gas has $\tau_t(r) < 1$ is included.

3.3 Results

In this section we will use our three new simulations which are magnetically arrested on the BH and in the innermost accretion flow, evolving from highly magnetized NT-type initial conditions. Our discussion focuses on results from RADHR and RADvHR to study how self-consistent radiative transport affects the accretion efficiencies when compared with the simulation MADiHR from [Avara et al. \(2016\)](#). We will also show how resolution affects disk behavior.

RADHR and RADLR have been run until $t=40,000R_g/c$, by which time the inner disk accretion flow reaches a MAD quasi-equilibrium, where magnetic flux continues to accumulate at the edge of the MAD region, and the disk is slightly sub-MAD beyond that transition radius. Figure 3.1 shows three main regimes of behavior in RADHR, culminating in the long-term evolution of the MAD inner disk

illustrated in the disk cross-sections. The first stage of evolution involves the rapid evolution of magnetic flux threading the horizon to balance the inner-most accretion flow and dynamical effects of the plunging region inside the innermost stable circular orbit (ISCO), as the system evolves away from equilibrium NT conditions, subject to the dynamically-relevant large-scale poloidal magnetic flux. The second behavioral stage involves mass accretion rate and magnetic flux growing until $t \sim 17,000 R_g/c$. At that point there is a weak point in the inner disk and a large magnetic disruption occurs which redistributes a lot of poloidal flux into the disk, increasing the size of the MAD region. The final stage, covering roughly the second half of the simulation involves a quasi-steady state MAD accretion flow, order unity oscillations of the horizon threading flux (consistent with prior numerical findings), and a general accretion structure very similar to the MADfHR simulation in [Avara et al. \(2016\)](#), where only the horizon and inner disk reach the MAD state over the time they were able to run their simulation.

In [Figure 3.2](#) we show characteristic quantities that describe the quasi-steady state of the disk. We time averaged these quantities over the last quarter of our high resolution simulation that we were able to run for a longer time, RADHR (RADvHR was too expensive to run longer for this work). We average over the period $t=30,000$ - $40,000 R_g/c$, when the disk evolution is less subject to initial conditions different than the unknown true thin-disk steady-state structure, for which there is no detailed analytic radiative model. In the next sub-sections we will make a discussion of each of these quantities that we believe best characterize the accretion flow in our simulations, and provide a direct comparison to prior work with *ad hoc* cooling. We will also describe the time dependence of some quantities, will present the results of our highest resolution simulation, RADvHR, and describe resolution effects.

3.3.1 Accretion rate

Analyzing the mass accretion rate profile of our simulation we can observe that the simulation has reached a quasi-steady state out to a radius of $r \sim 15 R_g$, but it is clear from the radial dependence of \dot{M} that going further out there are larger

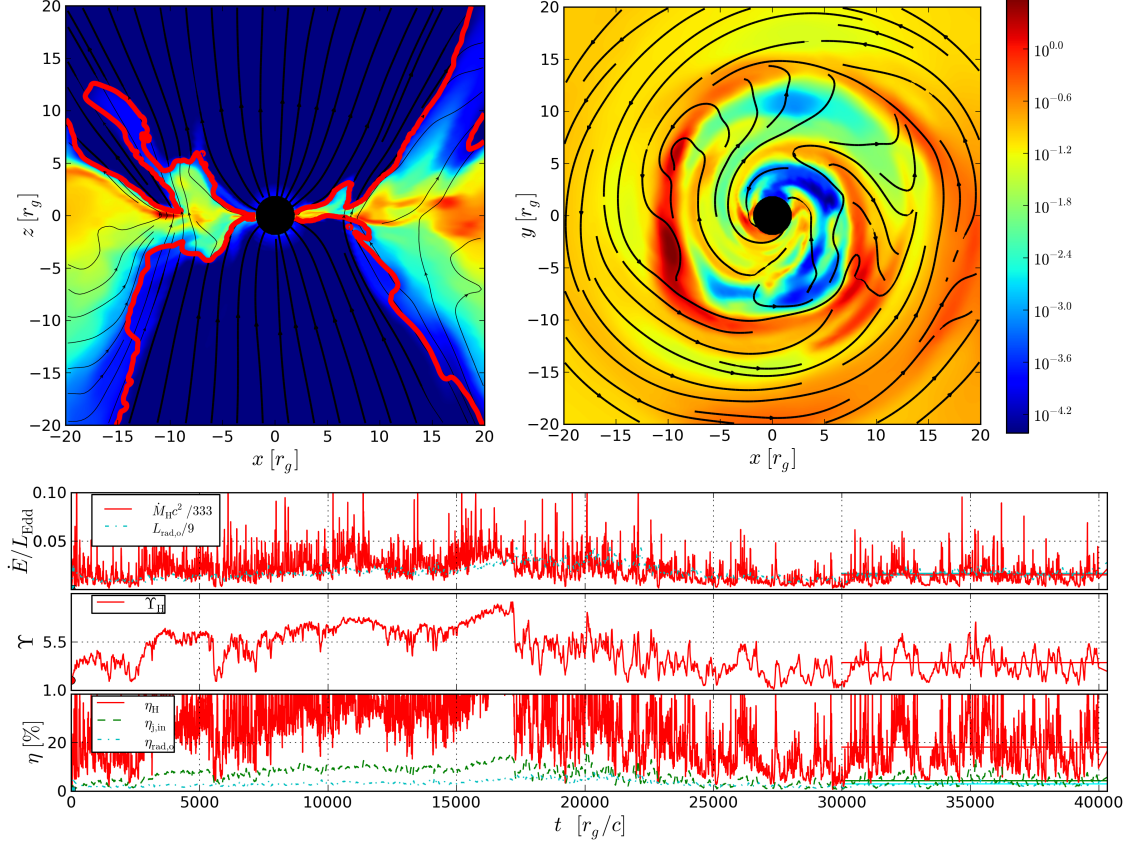


Figure 3.1: Snapshot of our simulation RADHR at the time $t=40.000R_g/c$ where the top two panels represents the $X - Z$ at $y=0$ and $X - Y$ at $z = 0$ slices of the density with the red line showing where $b^2/\rho=1$ and the black lines with arrows trace field lines where thicker black lines show where field is lightly mass loaded. The top sub-panel shows the mass accretion rate at the horizon (red line) and the luminosity (green line). The middle sub-panel shows the magnetic flux in the horizon normalized so that order unity is a dynamically substantial amount of magnetic flux. The bottom sub-panels shows the accretion efficiencies in the horizon (red line), jet efficiency (green line) measured at $15R_g$ and radiation (blue line) measure at $50R_g$.

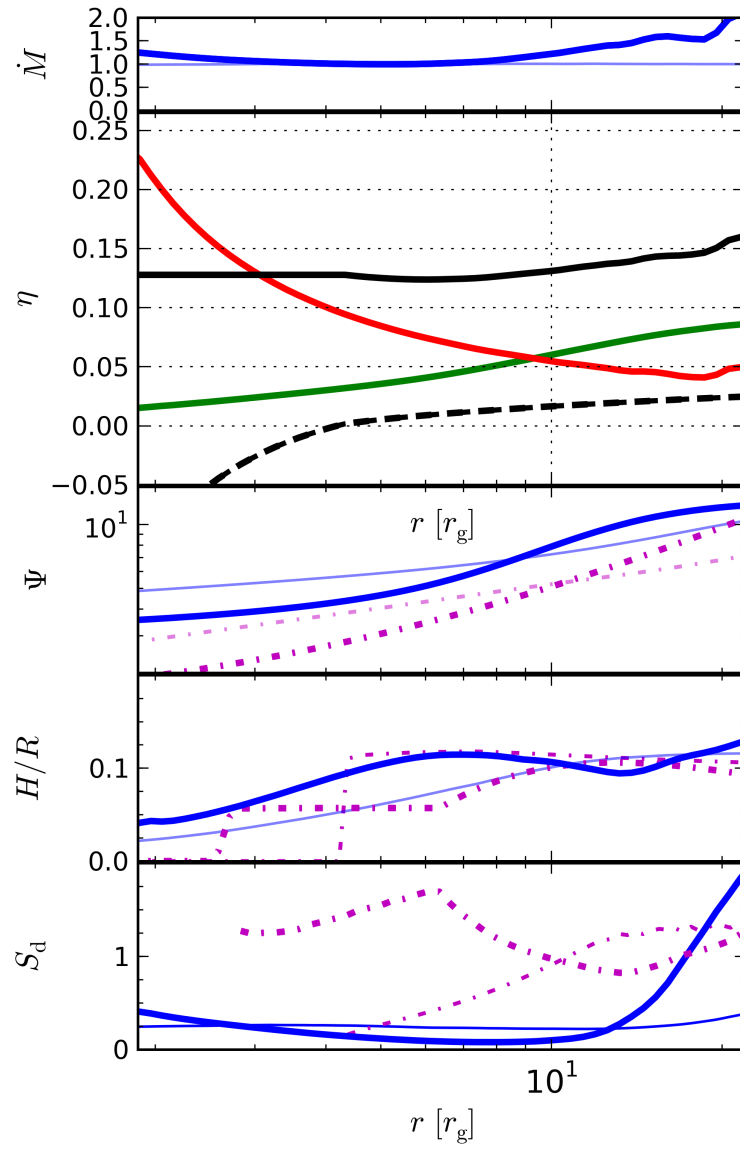


Figure 3.2: (Caption on next page.)

Figure 3.2: (Figure on previous page.) Characteristic quantities as a function of radius, time-averaged over the period $t = [30,000-40,000]R_g/c$ for the simulation RADHR. Panels consecutively show, from top to bottom: the mass accretion rate (\dot{M}), energy efficiencies (η) for different parts of the stress-energy tensor, magnetic flux (Ψ), disk scale-height (H/R), and S_d . In efficiencies plot the black line corresponds to the total gas+radiative (black line), electromagnetic (green line), matter (red) and radiation (black dashed) components. The magenta lines in the plots of Ψ , H/R , and S_d correspond to their initial values. The thick lines show values for RADHR and the thin line MADiHR from (Avara et al., 2016) time-averaged as in that paper.

deviations where the disk is still evolving from initial conditions. The large-scale magnetic flux in these types of simulations enhances these effects due to large-scale coronal flows, large mass transfer from MRI channel modes, and initial radiative evolution since the disk in this simulation does not start in an equilibrium state due to the radiation. Inside the ISCO there is also a deviation in the radial dependence of \dot{M} due to mass injection associated with the floors which demands a careful analysis. It is worth noting that in these and the simulations of Avara et al. (2016) the radial dependence of \dot{M} near the BH flattens when the number of snapshots over the averaging time period increases, though it is unclear if it would improve beyond the average shown here if more snapshots were available from the simulation output.

The additional mass added by the floor in the simulation is removed from the calculation of \dot{M} where cells have rest-mass values of $b^2/\rho > 1$. The profile of Avara et al. (2016) is much flatter because they time average over a later and longer period, $30,000 - 70,000R_g/c$ in MADiHR, an *ad hoc* cooling function evolves the disk toward equilibrium faster than the self-consistent processes we capture with full radiative transport, which demands more time to reach thermal equilibrium, and because the higher resolution allows large-scale initial transient modes to break up faster thus having a smaller impact on later evolution (e.g. parasitic modes of the

MRI at intermediate and large radii).

3.3.2 Scale Height

In these simulations with self-consistent radiative transport, we start with a NT disk with a scale height of 0.1, but there is no a priori reason to expect that the MAD disk resulting from these initial conditions should persist at this disk width. There was some tuning of initial conditions using test simulations to try to attain a scale height of 0.1 but this result is entirely self-consistent with the mass accretion rate and radiative transport alone. On the other hand, the disk scale height was fixed directly in [Avara et al. \(2016\)](#). This is one of the central advantages of including self-consistent radiative transport, which would allow an inherently thermally unstable disk to collapse if that were the true physical behavior.

Unlike the prediction from thin-disk theory, and similar to the findings of [Mishra et al. \(2016\)](#); [Sądowski et al. \(2016\)](#), our disk is thermally stable in the inner parts. Over the $30,000 - 40,000 R_g/c$ time period we average RADHR we find that the disk has reached thermal equilibrium only in the inner parts, not having enough time to reach an equilibrium state further out. We determine that a given radius has reached thermal equilibrium when that part of the disk has reached inflow/outflow quasi-equilibrium and the scale height, in part governed by vertical radiative transport and pressures support evolving under temperature evolution, stabilizes to roughly a fixed value. The time evolution of H/R at a sampling of radii is shown in Figure 3.3. By $25,000M$ the values of H/R in RADHR at $H/R = R_H, 10R_g, 20R_g$ have converged to the expectation for a magnetically choked flow (standard inner disk structure in the MAD state) where the disk has $H/R \approx 0.1$.

The radial profile of the disk shown in 3.2 shows the inner region ‘choked’ by magnetic compression, where the disk scale height is reduced to ~ 0.04 . In the inner edge of the disk the scale height grows to 0.1 at $r=5R_g$ and to 0.1 by $r=10R_g$. Beyond that radius we don’t show the values because the disk hasn’t reached thermal equilibrium in this locations. For comparison, the MADiHR simulation in [Avara et al. \(2016\)](#) had $H/R \sim 0.05$ near the black hole and 0.1 throughout the rest

of the disk. Thus there is significant similarity in disk structure as a function of radius in simulations with radiative transfer and those using only an *ad hoc* cooling function. This gives additional credibility to the findings taken from the much longer simulations with *ad hoc* cooling since artificial cooling and the associated choices for cooling timescale are arguably the least trustworthy in the plunging region and very inner disk.

In a future paper we will provide an extensive study of stability of the disk and describe the processes by which thin disks, formally thermally unstable in standard thin-disk theory, appear to be stabilized in the MAD state.

3.3.3 Efficiencies

Figures 3.2 and 3.5 show the radial profile of the total disk efficiency and the different contributions to the total including all radiation (in both optically thick and thin regions), energetics of the matter, and electromagnetic (EM) flux. Total disk efficiency, efficiency of the accretion flow in converting gravitational potential energy to combined forms escaping beyond the domain studied (transport to infinite radius opens questions addressed in the conclusions), is roughly 17% out to $r=20R_g$ in RADvHR, $\sim 13\%$ in RADHR, and is more constant for RADHR in the region inside $10R_g$ where the disk is more securely in inflow quasi-equilibrium. While the conversion of energy into radiation is significantly less in this simulation than was estimated using the *ad hoc* cooling procedure for MADiHR, there is some additional contribution by the matter component, and possibly the EM component beyond the choked region of the inflow. RADvHR has significantly more outward going EM energy flux, but it is unclear if this enhancement is due to better resolution in RADvHR or if it is a transient that would disappear if the simulation were ran the same length as RADHR and RADLR. If one considers only the radiation that reaches the optically thin region and would travel outward unimpeded, the radiative efficiency of our MAD thin disk is even less, only $\sim 2\%$. Thus, the total efficiency of this type of disk is significantly enhanced beyond the expected NT value but the energy is transported outward in the form of winds and jets predominantly rather

than radiation.

For our system with spin $a/M = 0.5$, the total efficiency of RADHR is 18.6% and the corresponding value from NT73 is 8.2%, a deviation of 125%. At the horizon, the efficiency in matter, electromagnetic and radiation forms are $\eta_H^{EM}=1.5\%$, $\eta_H^{MAKE}=22.5\%$ and $\eta_H^{Rad}=-5.5\%$, respectively. At $r=50R_g$ and we found that the jet is carrying 4.28%, the wind 7.39%, and the radiation 2.94%, where for the jet efficiency 4.09% is in the electromagnetic form and 0.20% in the matter, while for the wind 4% is being carried by the electromagnetic part and 3.39% in the matter. The summed values of the efficiencies carried by the jet, wind and radiation is less than the total efficiency and this difference is because even at $R=50R_g$ it's not trivial to guarantee that the wind material will reach infinity and for this reason we have assumed that the wind efficiency is $\eta_{wind} = \eta_{BH} - \eta_{jet} - \eta_{Rad}$; using this condition we found that the wind has an efficiency of 11.4%.

3.3.4 Magnetic flux

Measuring the absolute flux threading the horizon as a function of time, demonstrated in Figure 3.3, we find that the black hole gains a significant quantity of poloidal magnetic flux across the first half of the simulation, in the initial transitory phase due to large scale MRI channel modes that survive until the ϕ -symmetry of the field falls subject to parasitic modes and non-linearity. Then, similar to the MADiHR in Chapter 2, during the early evolution we observe the two modes of flux accumulation as it is transported both along the disk surfaces through a coronal-type mechanism and through disk advection. Similar to the build-up of flux from sub-MAD to MAD conditions on the horizon seen in MADfHR there is a steady build-up of flux on the horizon in RADHR until at $\sim 17,000R_g/c$ there is more flux on the horizon than the disk can contain, and a significant portion of the flux on the horizon finds a low pressure, ‘weak’ spot in the previously rather axisymmetric disk and reconnects, pushing out into the disk through that point. Future work will be needed to determine if the velocity profile of the disk over some time-periods renders it stable to the magnetic Rayleigh-Taylor instability, which could also contribute to

determining when the field will break free from the horizon. Whatever the process, from that moment on the more highly magnetized disk inside $r \sim 10R_g$ is MAD.

Due to constraints imposed by having NT-type initial conditions necessary to study the disk with self-consistent radiative transport, and having attainable resolution for the outer disk in our simulations, a significant portion of the poloidal magnetic flux in the outer disk is lost as the system evolves through initial transients. Despite this loss of flux in the disk, analyzing the suppression factor (S_d) of RADHR reveals that at late times the disk reaches the MAD state out to $r = 15R_g$. As in [Avara et al. \(2016\)](#) this radius grows over time as disk and coronal processes transport more magnetic flux inward.

When the net vertical magnetic flux threading any given radius in the disk increases as flux is transported inward (or alternatively decreases if it is diffusing outward), we expect the value of α_{mag} to increase at that radius. Once a section of the disk has reached the MAD state, however, the value of α_{mag} is expected to saturate at a maximum and this can be seen in the evolution of α_{mag} at $10R_g$ in [Figure 3.3](#), where it's possible to see that by the time $t=20,000R_g/c$ the value of effective α_{mag} rises and saturates to be roughly constant for the remainder of the simulation.

3.3.5 Luminosities

In [Figure 3.4](#) we use the time- ϕ averaged structure of the radiative and EM luminosities to demonstrate the angular distribution of this outgoing energy, the dissipate locations where radiation originates in the accretion inflow/outflow, and the distribution of reprocessing. Most of the EM flux comes from the jet in the south which is less isotropically distributed in θ , while the jet pointing to the north direction shows a more uniform distribution. The electron scattering surface has a large opening angle due to the substantial quantity of material blocking the radiation at large distances.

The radiation luminosity along jets in both directions also exhibits a non-uniform distribution having a more enhanced emission in the north side in a opening

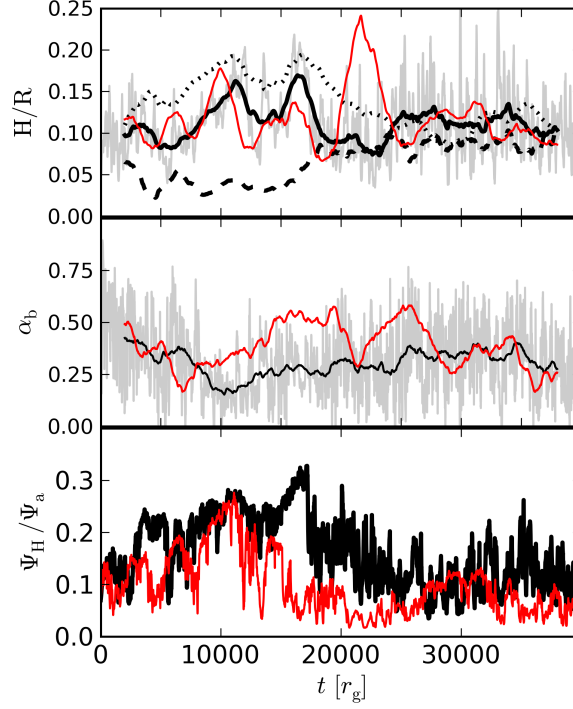


Figure 3.3: Red is for RADLR, black for RADHR. Top panel: Disk scale-height as function of time. The solid line corresponds to the values for $10R_g$ (lines for all radii are smoothed, with only the $10R_g$ line duplicated without smoothing in gray), the dotted and dashed lines correspond to the values of H/R at the horizon and $20R_g$ respectively. Middle: Magnetic α measured at $10R_g$ (full, un-smoothed RADHR data in gray). Bottom: Amount of magnetic flux on the horizon normalized by the amount of magnetic flux contained in the portion of the disk which reaches one inflow time by the end of the simulation, i.e. the total magnetic flux available for the inner disk and horizon.

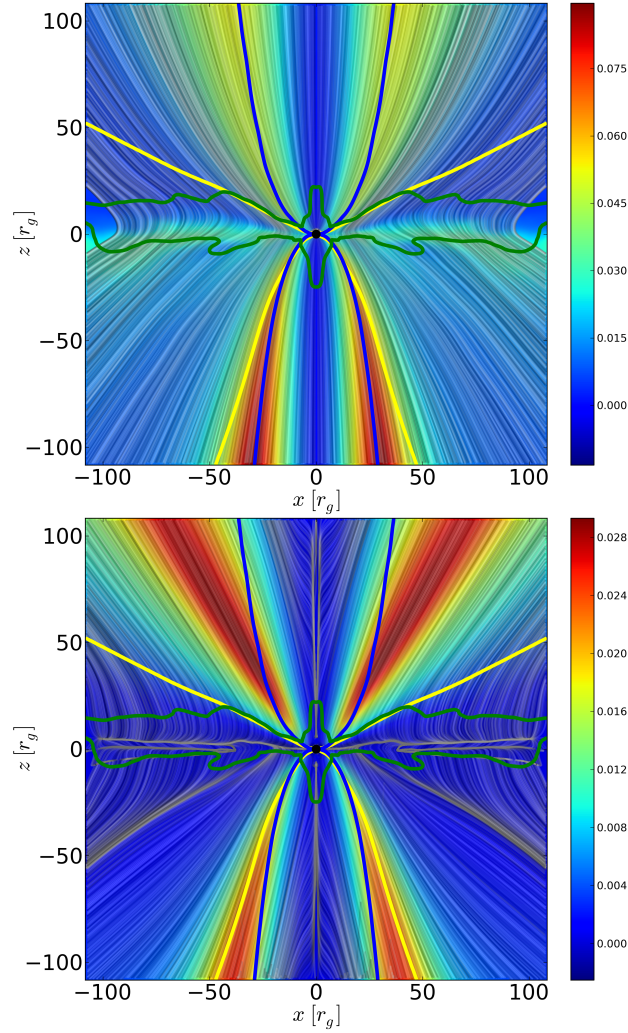


Figure 3.4: Top: Electromagnetic luminosity per unit angle $(\partial_\theta L_{EM})/(\dot{M}_H c^2)$ with time- ϕ averaged magnetic flux (translucent gray lines); blue lines show the $b^2/\rho=1$ boundary; the green line shows the $u^r=0$ boundary; yellow is the surface where optical depth reaches unity to electron scattering, integrating inward from a large, but at least moderately evolved, radius. Bottom: lab-frame radiation flux and radiation luminosity.

angle roughly similar to the EM emission. The disk seems to spontaneously break the north-south symmetry of the emission and then the larger radiation flux to the north may maintain that asymmetry for long periods of time. It is not clear if the asymmetry would persist if the RADHR simulation was run longer, but we see this present to some degree in each of our GRRMHD simulations and a weaker asymmetry was seen in some simulations of [Avara et al. \(2016\)](#) as well, suggesting the magnetic wind may be playing a role in the observed behavior.

For both EM and radiation streaming, it is possible to see that the emission largely originates from the region inside $r=15R_g$.

3.3.6 Resolution effects

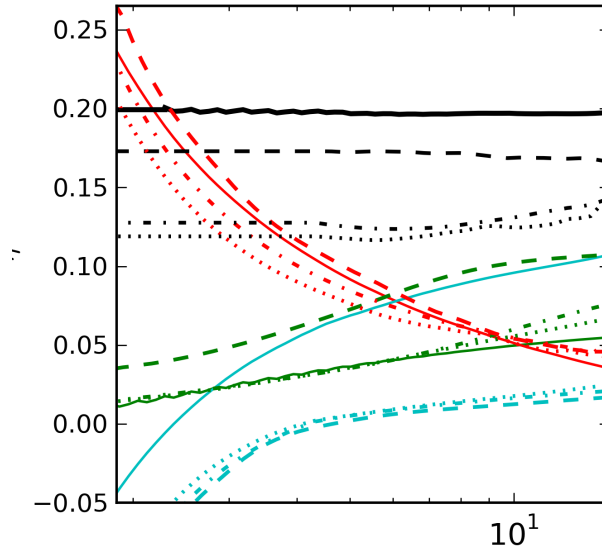


Figure 3.5: Plot showing the efficiencies for the simulation RADHR (dot-dashed line), RADvHR (dashed line), RADLR (dotted line) and MADiHR (continuous line). Black: total, Red: PAKE, Green: EM, Cyan: Radiation.

In this section we will demonstrate how the resolution affects the disk thickness, efficiencies, accretion rate, stress and the MAD state.

The disk thickness at the horizon for simulation RADHR(LR) is 0.04 (0.03), at $r=5R_g$ is 0.1 (0.08), and at $r=20R_g$ is 0.12 (0.15). When comparing the values at

the horizon it's possible to see that the disk thickness may be sensitive to resolution: low resolution may lead to enhanced dissipation through radiation, with enhanced escape potential, thereby cooling the disk further and into a thinner distribution. where the disk hasn't reached thermal equilibrium at large radii.

When comparing S_d for our simulations RADHR and RADLR, we found that RADHR has reached the MAD state out to $r=16R_g$ while RADLR is MAD out to $r=13R_g$. This difference can be explained considering resolution of the fastest growing MRI modes, which are important to the processes of magnetic field dynamo and transport in the part of the disk that is sub-MAD. Our simulation RADHR has $Q_{\theta,\phi}=110,13$ while RADLR has $Q_{\theta,\phi}=21,8$ showing that the MRI is not resolved for our simulation S2, affecting this transport of magnetic flux.

In Figure 3.3 one can see that the higher resolution of RADHR makes the time evolution of the disk scale height smoother and more magnetic flux is held by the horizon and inner disk.

Since the numerical resolution seems to affect the transport of magnetic flux we might expect our low resolution simulation RADLR to have lower efficiencies in the horizon and jet. For the jet we expect a lower efficiency since less rotational energy is extracted from the black hole while for the jet and radiation at $r=50R_g$ we must expect the efficiencies to be larger since the wind and radiation in this case absorb more energy. As expected the jet efficiency is 3.06%, compared to 4.28% for RADHR, the wind has 15.8% (7.39% for RADHR) and the radiation 4.58% (2.94%).

The most robust measure of resolution effects in our simulation suite is the monotonically increasing total efficiency with increasing resolution seen in Figure 3.5. While we expect the EM efficiency component of RADvHR to likely drop to a value consistent with other simulations if we were to run it longer, even then, it would have a higher total efficiency compared to RADHR and RADLR respectively. Thus, the true total efficiency of a MAD thin disk is likely underestimated by our simulations. While the estimate for radiative efficiency in MADiHR is found to be an overestimate in light of this work, it is worth noting that the resolution was substantially higher, which would be consistent with the trend seen in these new

simulations.

3.4 Discussion and Conclusions

We have shown the results of the first known simulations of radiatively efficient thin disks, with $H/R \sim 0.1$, around a spinning black hole with $a/M=0.5$, that are in the MAD state and include self-consistent radiative transport. Our longer high-resolution simulation RADHR reached the MAD state out to $17R_g$ and most energy extracted by the disk is carried away by the wind consistent with the findings in Chapter 2 but with a smaller total efficiency due to a significantly smaller radiation component. This is because our calculations include self-consistent absorption and scattering of the radiation, advection by plunging material, and true ray-tracing. We measured the electromagnetic and radiation luminosities and we found anisotropic emission in both cases. The electromagnetic emission is dominated by the southern jet/wind, with the jet in the north direction having more uniform distribution. Radiation, on the other hand, prefers emission to the north.

If one considers the radius at which radiation dissipated in the central disk no longer has a time-averaged path leading to the infinite observer, and is instead captured by the horizon (whether it streams away from the disk material first or not), one can make a more accurate estimate for a radiation inflow/outflow transition radius than the simple photon orbit chosen in the previous chapter. For RADHR this is $\sim 4R_g$. If only radiation outside that radius is considered from MADiHR, the disk has a total radiative efficiency of $\sim 6 - 7\%$. Allowing for some additional dissipation of radiative energy by the wind component, this could easily match the 8% NT prediction. The additional 4% discrepancy between RADHR and MADiHR is primarily from contributions between the ISCO and $\sim 10R_g$. This is where additional behavior of the energetics of the flow, advection, choking/magnetic compression, and the atypically fast cooling rate chosen in Chapter 2 could account for the difference. Because the geometry, magnetization, and resolution of the accretion flow in this region is not identical in RADHR and MADiHR, we are not yet

able to determine if the 4% difference is inherent to radiative transport, or due to different disk initial conditions and simulation parameters. Future simulations will shed light on this difference.

One should note that the radiative and magnetic energy converted from gravitational potential energy of the accretion flow has above-NT contributions everywhere the disk is MAD in RADHR and MADiHR. This could imply that a disk MAD out to larger radii than studied here would have increasing efficiency with increasing MAD/non-MAD transition radius. However, this is somewhat speculative and requires further numerical exploration.

A key result of this work that will also be explored in the future is the thermal stability of the disk, likely a result of the very strong magnetic fields intrinsic to the MAD state. It remains to be shown if there is a qualitative difference in disk stabilization by a strong magnetic field in a standard disk that is MRI dominated, compared to a disk in the MAD state where the MRI no longer dominates the accretion process.

Chapter 4: Efficiency of Super-Eddington Magnetically-Arrested Accretion

Abstract

The radiative efficiency of super-Eddington accreting black holes (BHs) is explored for magnetically-arrested disks (MADs), where magnetic flux builds-up to saturation near the BH. Our three-dimensional general relativistic radiation magnetohydrodynamic (GRRMHD) simulation of a spinning BH (spin $a/M = 0.8$) accreting at ~ 50 times Eddington shows a total efficiency $\sim 50\%$ when time-averaged and total efficiency $\gtrsim 100\%$ in moments. Magnetic compression by the magnetic flux near the rotating BH leads to a thin disk, whose radiation escapes via advection by a magnetized wind and via transport through a low-density channel created by a Blandford-Znajek (BZ) jet. The BZ efficiency is sub-optimal due to inertial loading of field lines by optically thick radiation, leading to BZ efficiency $\sim 40\%$ on the horizon and BZ efficiency $\sim 5\%$ by $r \sim 400r_g$ (gravitational radii) via absorption by the wind. Importantly, radiation escapes at $r \sim 400r_g$ with efficiency $\eta \approx 15\%$ (luminosity $L \sim 50L_{\text{Edd}}$), similar to $\eta \approx 12\%$ for a Novikov-Thorne thin disk and beyond $\eta \lesssim 1\%$ seen in prior GRRMHD simulations or slim disk theory. Our simulations show how BH spin, magnetic field, and jet mass-loading affect the radiative and jet efficiencies of super-Eddington accretion.

4.1 Introduction

Black hole (BH) accretion drives a broad range of phenomena, including quasars, active galactic nuclei, BH X-ray binaries, some gamma-ray bursts, and tidal disruption events (TDEs). The disk's gravitational potential energy and BH spin

energy are converted into radiation, winds, and relativistic jets via magnetic stresses generated by the magneto-rotational instability (MRI) (Balbus and Hawley, 1998a), magnetic field threading the disk (Blandford and Payne, 1982), or magnetic field threading the BH (Blandford and Znajek, 1977). Magnetic torques are maximized when magnetic flux advects inward and piles-up until magnetic stresses balance incoming gas forces – the so-called magnetically-arrested disk (MAD) state (Narayan et al., 2003). Simulations of non-radiative MADs show up to $\sim 300\%$ total efficiency (Tchekhovskoy et al., 2011; McKinney et al., 2012), corresponding to 3 times the energy out as going into the BH. A fundamental question is: What form does this energy take at large distances and what fraction is radiative?

The radiative efficiency of BH systems is expected to be dependent upon the accretion rate \dot{M}_0 , which controls the density, disk thickness, and dynamical importance of radiation (from gas-pressure dominated at low \dot{M}_0 to radiation-pressure dominated at high \dot{M}_0). To scale $\dot{M}_0 c^2$ or the radiative luminosity L , for a black hole mass M , speed of light c , gravitational constant G (giving gravitational radius $r_g \equiv GM/c^2$), and Thomson electron scattering opacity κ_{es} , one can use the Eddington luminosity

$$L_{\text{Edd}} = \frac{4\pi G M c}{\kappa_{\text{es}}} \approx 1.3 \times 10^{46} \frac{M}{10^8 M_{\odot}} \text{ erg s}^{-1}. \quad (4.1)$$

One can also choose to normalize \dot{M}_0 by $\dot{M}_{\text{Edd}} = (1/\eta_{\text{NT}})L_{\text{Edd}}/c^2$, where η_{NT} is the nominal accretion efficiency for the Novikov-Thorne thin disk solution (Novikov and Thorne, 1973a) (commonly, a fixed $\eta_{\text{NT}} = 0.1$ is used, but we include the spin dependence).

For luminosities $L \gtrsim 0.3L_{\text{Edd}}$, the accretion flow is expected to become geometrically thick and optically thick, and in this regime the photons can remain trapped within the flow as in the “slim disk” model (which includes no magnetic field) (Abramowicz et al., 1988). The super-Eddington accretion regime where $\dot{M} \gtrsim \dot{M}_{\text{Edd}}$ or $L \gtrsim L_{\text{Edd}}$ may help explain ultra-luminous X-ray sources as highly super-Eddington stellar-mass BHs (Watarai et al., 2001; Miller and Colbert, 2004). Also, some black hole X-ray binaries can have $L \gtrsim L_{\text{Edd}}$ (e.g., SS433, Margon et al.

1979; Takeuchi et al. 2010; GRS1915+105, Fender and Belloni 2004), while tidal disruption events seem to require $\dot{M} \gg \dot{M}_{\text{Edd}}$ (Bloom et al., 2011).

In this paper, we seek to test whether super-Eddington MADs around spinning BHs are radiatively efficient. We use the general relativistic radiation magnetohydrodynamic (GRRMHD) code HARMRAD, which uses the M1 closure for radiation (McKinney et al., 2014). The slim disk model and recent GRRMHD simulations of non-MAD (i.e. lower magnetic flux than MAD on the BH and in the disk) super-Eddington flows are radiatively inefficient with $L \lesssim L_{\text{Edd}}$ even for $\dot{M} \sim 100\dot{M}_{\text{Edd}}$ (Sądowski et al., 2014; McKinney et al., 2014), far below the thin disk Novikov-Thorne (NT) efficiency (e.g. about 6% efficient for BH spin of $a/M = 0$ to 12% efficient for $a/M = 0.8$). However, MADs (not yet studied with radiation) can maximize the efficiency and may lead to a radiatively efficient state. This is also plausible for rapidly spinning BHs because MADs are then compressed into a thin disk (McKinney et al., 2012), which can lose radiation more rapidly.

We discuss the physical and numerical setup in §4.2. Results and discussions are presented in §4.3. We summarize in §4.4.

4.2 Fully 3D GR Radiative MHD MAD Model

This model with black hole mass of $M = 10M_{\odot}$ and dimensionless spin $a/M = 0.8$ has nominal thin disk efficiency $\eta_{\text{NT}} \approx 12.2\%$, so that $\dot{M}_{\text{Edd}} \approx 1.2 \times 10^{19} \text{g/s}$ (see Eq. 4.1). While we choose a specific BH mass, the flow is strongly electron scattering dominated and so the results might apply roughly equally to all BH masses.

4.2.1 Opacities

We assume solar abundances (mass fractions of Hydrogen, Helium, and “metals”, respectively, $X = 0.7$, $Y = 0.28$, $Z = 0.02$) giving electron fraction $Y_e = (1 + X)/2$ and mean molecular weight $\bar{\mu} \approx 0.62$, entering gas entropy, pressure, and temperature T_g [Kelvin].

We use a frequency (ν) mean of the opacity α_{ν} to get an absorption-mean ab-

sorption opacity (units of $[\text{cm}^2/\text{g}]$) of $\kappa = (\int_\nu d\nu \alpha_\nu J_\nu) / (\int_\nu d\nu J_\nu)$, where the absorbed radiation J_ν is assumed to be a Planck distribution at a radiation temperature of $T_r = (\hat{E}/a_{\text{rad}})^{1/4}$ [Kelvin], where $\hat{E} = u^\mu u^\nu R_{\mu\nu}$, u^μ is fluid 4-velocity, R is radiation stress-energy tensor, and a_{rad} is the radiation constant.

The electron scattering opacity is

$$\kappa_{\text{es}} \approx 0.2(1 + X)\kappa_{\text{kn}}, \quad (4.2)$$

where the Klein-Nishina correction for thermal electrons is $\kappa_{\text{kn}} \approx (1 + (T_g/(4.5 \times 10^8))^{0.86})^{-1}$ (Buchler and Yueh, 1976).

The absorption-mean energy absorption opacity is

$$\kappa_{\text{abs}} \approx \left(\frac{1}{\kappa_{\text{m}} + \kappa_{H^-}} + \frac{1}{\kappa_{\text{Chianti}} + \kappa_{\text{bf}} + \kappa_{\text{ff}}} \right)^{-1}, \quad (4.3)$$

which bridges between different temperature regimes. The molecular opacity is $\kappa_{\text{m}} \approx 0.1Z$, and the H^- opacity is $\kappa_{H^-} \approx 1.1 \times 10^{-25} Z^{0.5} \rho^{0.5} T_g^{7.7}$. Rest-mass density, ρ , is in cgs units. The Chianti opacity accounts for bound-free at slightly lower temperatures and is given by $\kappa_{\text{Chianti}} \sim 4.0 \times 10^{34} \rho (Z/Z_{\text{solar}}) Y_e T_g^{-1.7} T_r^{-3.0}$ (this accounts for the assumed $Z = Z_{\text{solar}} = 0.02$ for figure 34.1 in Draine (2011), most applicable for baryon densities of $n_b \sim 1 \text{cm}^{-3}$). The bound-free opacity is

$$\kappa_{\text{bf}} \approx 3 \times 10^{25} Z(1 + X + 0.75Y) \rho T_g^{-0.5} T_r^{-3.0} \ln(1 + 1.6(T_r/T_g)), \quad (4.4)$$

(Rybicki and Lightman, 1986), where the $1 + X + 0.75Y$ term is roughly accurate near solar abundances, and the $\ln()$ term comes from fitting the absorption-mean integral. The free-free opacity is

$$\begin{aligned} \kappa_{\text{ff}} &\approx 4 \times 10^{22} (1 + X)(1 - Z) \rho T_g^{-0.5} T_r^{-3.0} \ln(1 + 1.6(T_r/T_g)) \\ &\times (1 + 4.4 \times 10^{-10} T_g), \end{aligned} \quad (4.5)$$

for thermal electrons and no pairs (see Eq.5.25 in Rybicki and Lightman 1986 and Shu 1991). Thermal energy Comptonization is included as in Sądowski et al. (2015). The mean emission opacity κ_{emit} is the same as κ_{abs} but letting $T_r \rightarrow T_g$, such that Kirchoff's law gives an energy density emission rate of $\lambda = c\rho_0 \kappa_{\text{emit}} a_{\text{rad}} T_g^4$. The total opacity is $\kappa_{\text{tot}} = \kappa_{\text{es}} + \kappa_{\text{abs}}$. The low-temperature opacities avoid unphysical opacity divergences during the simulation.

4.2.2 Initial Conditions

The initial disk is Keplerian with a rest-mass density that is Gaussian in angle with a height-to-radius ratio of $H/R \approx 0.2$ and radially follows a power-law of $\rho_0 \propto r^{-0.6}$. The solution near and inside the inner-most stable circular orbit (ISCO) is not an equilibrium, so near the ISCO the solution is tapered to a smaller density ($\rho_0 \rightarrow \rho_0(r/15)^7$, within $r = 15r_g$) and a smaller thickness ($H/R \rightarrow 0.2(r/10)^{0.5}$, within $r = 10r_g$ – based upon a low-resolution simulation). The total internal energy density u_{tot} is estimated from vertical equilibrium of $H/R \approx c_s/v_K$ for sound speed $c_s \approx \sqrt{\Gamma_{\text{tot}} P_{\text{tot}}/\rho_0}$ with $\Gamma_{\text{tot}} \approx 4/3$ and Keplerian speed $v_K \approx (r/r_g)/((r/r_g)^{3/2} + a/M)$. The total ideal pressure $P_{\text{tot}} = (\Gamma_{\text{tot}} - 1)u_{\text{tot}}$ is randomly perturbed by 10% to seed the MRI. The disk gas has $\Gamma_{\text{gas}} = 5/3$. The disk has an atmosphere with $\rho_0 = 10^{-5}(r/r_g)^{-1.1}$ and gas internal energy density $e_{\text{gas}} = 10^{-6}(r/r_g)^{-5/2}$. The disk’s radiation energy density and flux are set by local thermal equilibrium (LTE) and flux-limited diffusion (McKinney et al., 2014) with a negligible radiation atmosphere.

We do not use polish donuts (Abramowicz et al., 1978) or equilibrium tori as initial conditions. The outer parts of tori have an extended column of gas at high latitudes that contributes significantly to spurious luminosity (see section 6.8 in McKinney et al. 2014), trapping of the disk wind and radiation, and artificial (instead of the self-consistent wind) collimation of the jet.

The initial magnetic field is large-scale and poloidal. For $r < 300r_g$, the coordinate basis ϕ -component of the vector potential is

$$A_\phi = \text{MAX}(r^\nu 10^{40} - 0.02, 0)(\sin \theta)^{1+h}, \quad (4.6)$$

with $\nu = 1$ and $h = 4$. For $r \geq r_0 = 300r_g$, the field transitions to monopolar using $A_\phi = \text{MAX}(r_0^\nu 10^{40} - 0.02, 0)(\sin \theta)^{1+h(r_0/r)}$. The field is normalized with ~ 1 MRI wavelength per half-height H giving a ratio of average gas+radiation pressure to average magnetic pressure of $\beta \approx 24$ for $r < 100r_g$.

4.2.3 Numerical Grid and Density Floors

The numerical grid mapping equations and boundary conditions used here are identical to that given in [McKinney et al. \(2012\)](#). The radial grid of $N_r = 256$ cells spans from $R_{\text{in}} \approx 0.688r_{\text{H}}$ (horizon radius r_{H}) to $R_{\text{out}} = 10^5 r_g$ with cell size increasing exponentially till $r \sim 500r_g$ and then even faster. Radial boundaries use absorbing conditions. The θ -grid of $N_\theta = 128$ cells spans from 0 to π with mapping given in [McKinney et al. \(2012\)](#) but with $n_{\text{jet}} = 0.7$ to follow the jet. Other coefficients are tuned so that the grid aspect ratio at $r \sim 30r_g$ near the equator is $1 : 2 : 3$ in $r, r d\theta, r \sin \theta d\phi$. Approaching the horizon the disk thins due to magnetic compression, so we refine the grid to have 20 points across a half-height thickness $H/R \sim 0.1$ on the horizon. The Poynting-dominated polar jet contains, respectively, about 80, 60, and 110 θ grid cells at $r \sim r_{\text{H}}$, $r \sim 20r_g$, and $r \gtrsim 500r_g$. This gives sufficient resolution of the Poynting-dominated jet. The ϕ -grid of $N_\phi = 64$ cells spans uniformly from 0 to 2π with periodic boundary conditions.

As in our other papers ([McKinney et al., 2012, 2013, 2014](#)), we test the so-called convergence quality factors for the MRI in the θ and ϕ directions ($Q_{\theta, \text{MRI}}$ and $Q_{\phi, \text{MRI}}$) and turbulence ($Q_{nlm, \text{cor}}$) measuring, respectively, the number of grid cells per MRI wavelength in the θ and ϕ directions and the number of grid cells per correlation length in the radial, θ and ϕ directions. At late times, our simulation has $Q_{\theta, \text{MRI}} \sim 340$, $Q_{\phi, \text{MRI}} \sim 45$, and rest-mass and magnetic energy densities have $Q_{nlm, \text{cor}} \sim 25, 20, 6$ at $r \sim 8r_g$, indicating good r, θ resolution and marginal ϕ resolution. We also measure the thickness of the disk per unit MRI wavelength, S_d , where $S_d < 0.5$ is where the MRI is suppressed. Initially $S_d \sim 0.6$ at all radii, while the time-averaged flow has $S_d \sim 0.1$ out to $r \sim 60r_g$.

The rest-mass and internal energy densities are driven to zero near the BH within the jet and near the axis, so we use numerical ceilings of $b^2/\rho_0 = 300$, $b^2/e_{\text{gas}} = 10^9$, and $e_{\text{gas}}/\rho_0 = 10^{10}$. The value of b^2/ρ_0 is at the code's robustness limit for the chosen resolution.

4.2.4 Diagnostics

The disk's geometric half-angular thickness (H) per radius (R) is

$$\frac{H}{R}(r, \phi) \equiv \frac{H_0}{R} + \frac{(\int_{\theta} \rho(\theta - \theta_0)^n dA_{\theta\phi})^{1/n}}{(\int_{\theta} \rho dA_{\theta\phi})^{1/n}}, \quad (4.7)$$

with $n = 2$, $H_0/R = 0$, and surface differential $dA_{\theta\phi}$. One computes θ_0 like H/R , but let $n = 1$ and $\{\theta_0, H_0/R\} = \pi/2$.

The mass accretion rate and energy efficiency are, respectively,

$$\dot{M}_0 = \left| \int \rho_0 u^r dA_{\theta\phi} \right|, \quad (4.8)$$

$$\eta = -\frac{\int (T_t^r + \rho_0 u^r + R_t^r) dA_{\theta\phi}}{[\dot{M}_0]_H}, \quad (4.9)$$

where T is the gas stress-energy tensor and $[\dot{M}_0]_H$ is the time-averaged \dot{M} on the horizon. The specific angular momentum accreted is $j = (\int (T_{\phi}^r + R_{\phi}^r) dA_{\theta\phi}) / [\dot{M}_0]_H$. Both η and j are composed of free particle (PAKE=kinetic+gravitational), thermal (EN), electromagnetic (EM), and radiation (RAD) components. The jet is defined as PAKE+EN+EM, in locations where magnetic energy density exceeds rest-mass energy density. The wind is defined as PAKE+EN, located outside the jet. The wind can also contain untapped EM and RAD components. The dimensionless magnetic flux (McKinney et al., 2014) is

$$\Upsilon \approx 0.7 \frac{\int dA_{\theta\phi} 0.5 |B^r|}{\sqrt{[\dot{M}_0]_H}}, \quad (4.10)$$

for radial magnetic field B^r in Heaviside-Lorentz units.

To obtain the optical depth, at each instant in time we compute

$$\tau \approx \int \rho_0 \kappa_{\text{tot}} dl. \quad (4.11)$$

For the radial direction, $dl = -f_{\gamma} dr$, $f_{\gamma} \approx u^t(1 - (v/c) \cos \theta)$, $(v/c) \approx 1 - 1/(u^t)^2$ (as valid at large radii), $\theta = 0$, and the integral is from $r_0 = 3000$ (being some radius beyond which only transient material would contribute to the optical depth, but a radius the disk wind has reached) to r to obtain $\tau_r(r)$. For the angular direction,

$dl = f_\gamma r d\theta$, $\theta = \pi/2$, and the integral is from each polar axis toward the equator to obtain $\tau_\theta(\theta)$. The flow’s “true radiative photosphere” is defined as when $\tau_r = 1$, a conservative upper limit to the radius of the photosphere for an observer, because radiation can escape by tracking with relativistic low-density parts of the jet.

The radiative luminosity is computed at each instant as

$$L = - \int dA_{\theta\phi} R_t^r, \quad (4.12)$$

which is usually measured at $r = 400r_g$, where we only include those angles where the gas has $\tau_r(r) < 1$.

4.3 Results and Discussion

Fig. 4.1 and Fig. 4.2 show the initial and final state of the accretion flow. The initial disk is threaded by a weak large-scale poloidal magnetic field around a spinning black hole with $a/M = 0.8$. Rotation amplifies the magnetic field via the MRI leading to accretion of mass, energy, angular momentum, and magnetic flux. The magnetic flux accumulates and eventually forms a quasi-steady super-Eddington ($\dot{M}_0 \sim 400L_{\text{Edd}}/c^2 \sim 50\dot{M}_{\text{Edd}}$) state that is a MAD (where the MRI is suppressed) out to $r \sim 60r_g$ after the model is evolved for a time $31,200r_g/c$. The magnetically-compressed radiatively efficient thin disk near the BH is exposed by the jet channel, and the magnetized wind carries a significant fraction of radiation away from the disk.

Fig. 4.3 shows the mass accretion rate, efficiencies, disk thickness, and magnetic flux as time-averaged from $t = 30,000r_g/c$ to $31,200r_g/c$. The disk is in inflow and thermal equilibrium out to $r \sim 20r_g$ with constant fluxes of mass, energy, and specific angular momentum vs. radius. The total (kinetic + gravitational + electromagnetic + radiative) efficiency $\eta \approx 50\%$. As in non-radiative MAD models (Tchekhovskoy et al., 2011; McKinney et al., 2012), the efficiency is beyond the Novikov-Thorne value of $\eta_{\text{NT}} \approx 12\%$.

The magnetic field threading the BH is strong, with $\Upsilon \approx 10$ at late time and $\Upsilon \approx 8$ on average with $B_z \propto r^{-5/4}$ through the disk. The magnetic field threading

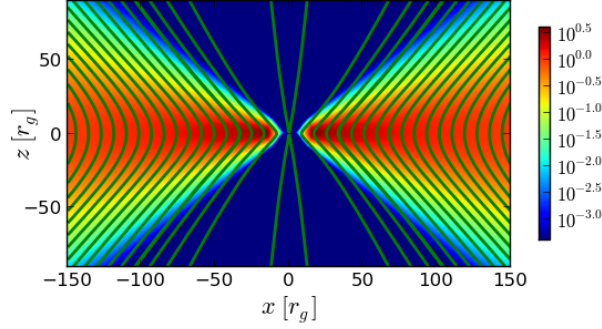


Figure 4.1: The initial ($t = 0$) state consists of a weakly magnetized radially-extended vertically-Gaussian disk with $H/R \sim 0.2$ around a spinning ($a/M = 0.8$) BH. Rest-mass density is shown as color with legend, while green lines show magnetic field lines. Density values are made dimensionless using \dot{M}_{Edd} , length r_g , and time r_g/c . The initial disk is threaded by weak (but ordered) magnetic flux, capable of accumulating onto the BH and leading to the MAD state.

the BH and disk leads to a magnetized wind that carries a significant amount of radiation away from the disk and helps to avoid the classical photon trapping effect of slim disks (Abramowicz et al., 1988). The magnetized wind at $r \sim 400r_g$ has a matter efficiency of about 15%, but the optically thick wind also contains about 15% trapped radiation energy and 10% electromagnetic energy that could be tapped for acceleration or heating. By $r \sim 400r_g$, the wind carries most of its radiation within a half-opening angle of 30° around the polar axes.

The Blandford-Znajek (BZ) effect leads to an electromagnetic, BZ, efficiency $\eta \sim 35\%$ on the BH. Some of that energy forms a jet with $\eta \sim 10\%$ at $r = 50r_g$, but some of that energy is absorbed by the wind, leading to a jet having only $\eta \sim 5\%$ by $r = 400r_g$.

Radiative-loading of magnetic field lines threading the BH leads to a lower-than-optimal BZ efficiency (relatedly, see Beskin et al. 2004; Takahashi and Ohsuga 2015) once the MAD state builds-up. The inertial loading of magnetic field lines is due to a total energy density $\rho_{\text{tot}} = \rho_0 + e_{\text{gas}} + \hat{E}$ once $\tau \gtrsim 1$ caused by ρ_0 keeping up with the MAD's higher b^2 when the numerical ceiling of $b^2/\rho_0 = 300$ is enforced. The

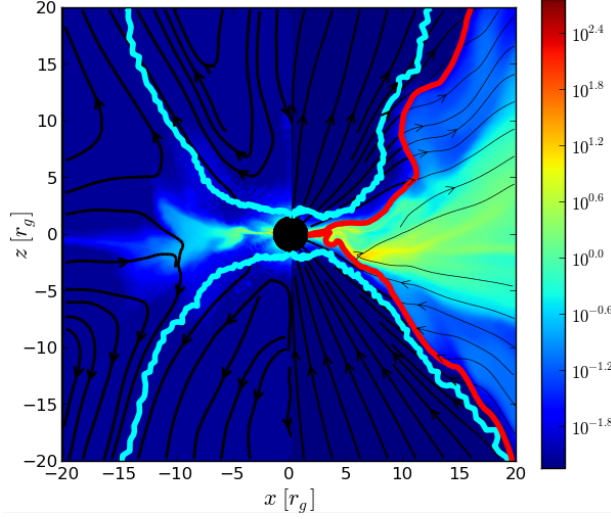


Figure 4.2: The evolved ($t = 31,200r_g/c$) super-Eddington MAD state, with the figure split at $x = 0$ as two panels ($x < 0$ on left and $x > 0$ on right). Left panel shows radiation-frame radiation energy density (color, with legend), radiation velocity lines (black, fixed line width), and optical depth of unity away from each polar axis, $\tau_\theta = 1$ (cyan lines). Right panel shows fluid-frame rest-mass density (color, same legend), magnetic field lines (black, thicker lines for more magnetized gas), where magnetic energy is equal to rest-mass energy density (red lines), and same optical depth (cyan lines). The MAD state reaches a quasi-steady state out to $r \sim 20r_g$. Radiation advects inward within the equatorial disk, outward through the low-density jet channel, and outward along with the optically thick wind.

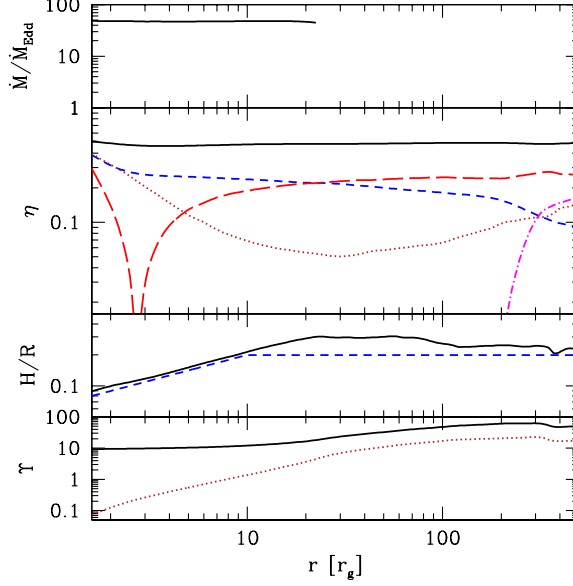


Figure 4.3: The time-averaged angle-integrated mass flux, efficiency, disk thickness, and magnetic flux. From top to bottom, panels are: Total mass accretion rate (\dot{M}_0) per unit \dot{M}_{Edd} out to where there is inflow and thermal equilibrium ($r \sim 20r_g$, beyond which the line is truncated), energy efficiency η (total: solid black line, electromagnetic: blue dashed, matter without rest-mass (i.e. kinetic+gravitational+thermal): dark red dotted, radiation (negative within $3r_g$): red long-dashed, radiative luminosity L : magenta dot-dashed), disk thickness H/R (evolved state: black solid, initial state: blue dashed), and magnetic flux (total on BH and threading disk: black solid, only threading disk: dark red dotted). The disk is magnetically compressed near the BH, and the thin disk generates a significant radiative flux that effectively releases starting at $r \sim 300r_g$. The initial disk with $H/R \approx 0.2$ has puffed up to $H/R \approx 0.3$ from $r \sim 20$ – $70r_g$ after evolving for several thermal times. By $r \sim 400r_g$, the luminosity reaches $L \sim 50L_{\text{Edd}}$.

optically thick radiation slows the jet magnetic field line rotation rate down by order unity compared to the optimal BZ value, because $b^2/\rho_{\text{tot}} \sim 1$ in the funnel (even if $b^2/\rho_0 \gg 1$ there) as determined by the rough condition that the jet and disk have similar b^2 , yet $\Upsilon \gg 1$ implies that $b^2 \sim \rho_0$ in the disk, and radiative energy density $\hat{E} \sim \rho_0$ (from a thermal estimate of $H/R \sim c_s/v_K \sim 0.3$). A restarted simulation with an exponentially reduced (as b^2/ρ_0 approached its ceiling) opacity has a BZ efficiency of $\eta \sim 100\%$ on the BH, as consistent with $\Upsilon \approx 8$ (Tchekhovskoy et al., 2011). A restarted simulation with a lower ceiling $b^2/\rho_0 = 100$ led to a 20% BZ efficiency. So, mass-loading and opacity physics in the funnel are important to BZ-driven jets and winds for super-Eddington flows where radiation crosses magnetic field lines.

Fig. 4.4 shows the jet, wind, and “true” photosphere at large radii. The jet-wind boundary oscillates in angle to order unity, causing the wind to absorb some of the jet and radiation energy. We have resolved the true photosphere at $r \sim 400r_g$, and the radiation escaping to an observer has a high radiative efficiency of $\eta \approx 15\%$ (comparable with the NT value of $\eta \sim 12\%$), corresponding to luminosity $L \sim 50L_{\text{Edd}}$. Most of this radiation is within a half-opening angle of 15° around the polar axes. The luminosity in this GRRMHD MAD simulation is much higher than predicted by the slim disk solution at $\eta \sim 2\%$ or seen in other viscous non-MAD or non-MAD MHD simulations at $\eta \lesssim 1\%$ (Ohsuga et al., 2005; Ohsuga and Mineshige, 2011; Sądowski et al., 2014; McKinney et al., 2014). Far beyond the photosphere, radiation might be absorbed (Sądowski and Narayan, 2015) or some might leak out of the wind containing $\eta \approx 15\%$ in trapped radiation, but our grid is too unresolved to accurately track energy conversion for $r > 600r_g$. The radiation ultimately released is high in our simulation because 1) the disk near the BH is forced to become thin; 2) a magnetized wind pulls radiation-filled material off the disk; 3) the jet drills a channel and pushes back the opaque disk wind; and 4) the jet becomes conical at large radii allowing free-streaming of radiation. These lead to an effective diffusion timescale shorter than in the slim disk model.

We also performed otherwise identical simulations that are MAD with $a/M =$

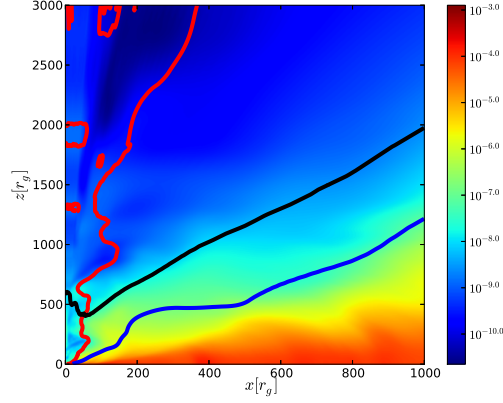


Figure 4.4: The evolved ($t = 31, 200r_g/c$) super-Eddington MAD state at large radii showing the jet, wind, and photosphere. Shows fluid-frame rest-mass density (color, with legend), where magnetic energy equal to rest-mass energy density (red lines), radiative photosphere at $\tau_r = 1$ (black line), and the wide-angle wind component's magnetic field line, within which (toward the polar axis) the outflow has achieved more than a single flow time along the line extending $\sim 1000r_g$ (blue line). Quantities are ϕ -averaged. The jet extends to $r \sim 30,000r_g$ with Lorentz factor $\gamma \sim 5$ by $r \sim 10^3r_g$. The wind extends to $r \sim 3000r_g$, with most of the wind's trapped radiation having an opening angle of 30° at $r \sim 400r_g$. The disk at $R \gg 100r_g$ has not evolved much. Radiation within $r \lesssim 400r_g$ can more freely stream within the jet's low-density channel. By $t \sim 30,000r_g/c$, at $r \sim 400r_g$ within 15° around the polar axis, the outflow become conical and optically thin.

0 as well as non-MAD simulations using a toroidal field in the initial disk (with $\beta \sim 20$ for all radii at the equator). The non-spinning MAD never produced a jet and the radiation remains trapped by the broad disk wind. Similarly, the toroidal field models with $a/M = 0$ and $a/M = 0.8$ show no low-density funnel region. Similar to [Sadowski and Narayan \(2015\)](#), our $a/M = 0$ MAD model with $\dot{M} \sim 20\dot{M}_{\text{Edd}}$ has a wind with NT-level efficiency of order 5% and negligible radiation flux at large radii by $r \sim 400r_g$ within the photosphere, because all radiation energy flux converted to kinetic energy flux. Our toroidal field models with $a/M = 0$ and $a/M = 0.8$ have $\dot{M} \sim \dot{M}_{\text{Edd}}$ with a wind efficiency of 2% and 4%, respectively, and a radiative efficiency of about 1%. So the formation of a low-density jet channel by a spinning BH, with enough magnetic flux to launch a jet and strong wind, helps super-Eddington accretion become radiatively efficient.

Convergence testing was performed by restarting each previously-mentioned model at a resolution twice lower in each dimension. The restarted simulation starts at half-way through the higher resolution simulation, and then the two resolutions are compared for the latter half of the simulations. We find that the total, BH, jet and radiative efficiencies, and Υ agree to within 30% or smaller error. Our convergence quality factors for the MRI and turbulence also suggest the simulations are converged.

A non-relativistic MHD simulation with $a/M = 0$ by [Jiang et al. \(2014\)](#) measured a NT-level radiative efficiency of about 5% that they attributed to MRI-driven magnetic buoyancy vertical transport of radiation. Their simulation had a small vertical extent $\pm 60r_g$, so τ computed from Eq. 4.11 does not include the extended wind. Over extended distances, a significant portion of radiation energy flux can convert into wind energy flux ([Sadowski and Narayan, 2015](#)). In our $a/M = 0.8$ MAD simulation, we attribute the high radiative efficiency to magnetic compression of the disk into a thin MAD, magnetized wind advection of radiation away from the disk, and the formation of a low-density jet channel through which radiation can more freely stream. Our simulation boundary is at $r \sim 10^5 r_g$, with accurate energy conversion out to $r \sim 600r_g$. Our photosphere at $r \sim 400r_g$ accounts for wind material that

reached $r \gtrsim 3000r_g$. If we ignore the extended wind, for the $a/M = 0.8$ MAD model we would miscalculate the radiative efficiency to be $\eta \sim 30\%$ – an overestimate by a factor of two. For the $a/M = 0$ MAD model, measuring at $r \sim 60r_g$ gives $\eta \sim 5\%$ – an overestimate from $\eta \sim 0\%$ (caused the wind absorbing radiation energy).

4.4 Summary

We have performed fully 3D simulations of super-Eddington accretion, including a simulation with $\dot{M}_0 \sim 400L_{\text{Edd}}/c^2 \sim 50\dot{M}_{\text{Edd}}$ onto a rotating black hole with $a/M = 0.8$. Sufficient magnetic flux was distributed throughout the disk that the BH and disk reached MAD levels, where magnetic forces pushing out balance gas forces pushing in. The MAD state enables the super-Eddington accretion flow to reach its maximum efficiency, with the total efficiency measured to be about 50% (higher for higher BH spins). Importantly, the system has a high radiative efficiency of about 15% (luminosity $L \sim 50L_{\text{Edd}}$) beyond the resolved photosphere at $r \sim 400r_g$. This occurs because the magnetized wind carries radiation away from the disk. Also, the magnetized jet creates a low-density channel for radiation to more freely stream and pushes away the more opaque wind. These effects increase the radiative flux escaping the disk and diminish conversion of radiation energy flux into kinetic energy flux of the wind. This mechanism allows high radiative efficiencies from super-Eddington accretion systems.

As applied to jetted TDEs ([Tchekhovskoy et al., 2014](#)), our super-Eddington MAD simulations show how the jet and radiative efficiencies depend not only upon BH spin and magnetic flux but also upon jet mass-loading physics that leads to sub-optimal BZ efficiencies via dragging of BH field lines by optically thick radiation. Also, while the wind absorbs some jet energy, the jet channel exposes the (otherwise obscured) inner hot X-ray emitting disk.

Acknowledgments

We thank Ramesh Narayan, Alexander Tchekhovskoy, Yan-Fei Jiang, and Aleksander Sadowski for discussions and acknowledge NASA/NSF/TCAN (NNX14AB46G), NSF/XSEDE/TACC (TG-PHY120005), and NASA/Pleiades (SMD-14-5451).

Chapter 5: Role of Magnetic Field Strength and Numerical Resolution in Simulations of the Heat-flux Driven Buoyancy Instability

Abstract

The role played by magnetic fields in the intracluster medium (ICM) of galaxy clusters is complex. The weakly collisional nature of the ICM leads to thermal conduction that is channelled along field lines. This anisotropic heat conduction profoundly changes the stability of the ICM atmosphere, with convective stabilities being driven by temperature gradients of either sign. Here, we employ the Athena magnetohydrodynamic code to investigate the local non-linear behavior of the heat-flux driven buoyancy instability (HBI), relevant in the cores of cooling-core clusters where the temperature increases with radius. We study a grid of 2-d simulations that span a large range of initial magnetic field strengths and numerical resolutions. For very weak initial fields, we recover the previously known result that the HBI wraps the field in the horizontal direction thereby shutting off the heat flux. However, we find that simulations which begin with intermediate initial field strengths have a qualitatively different behavior, forming HBI-stable filaments that resist field-line wrapping and enable sustained vertical conductive heat flux at a level of 10–25% of the Spitzer value. While astrophysical conclusions regarding the role of conduction in cooling cores require detailed global models, our local study proves that systems dominated by HBI do not necessarily quench the conductive heat flux.

5.1 Introduction

The intracluster medium (ICM) is a hot, weakly-collisional plasma comprising the majority of the baryonic mass in galaxy clusters. It has gained increasing attention in the last few decades since it provides a rich environment for the study of feedback, cosmology, low-density magnetohydrodynamics (MHD), and magnetogenesis. One area of recent focus is the study of dynamics induced by anisotropic conduction and anisotropic viscosity. The main goal of these studies has been to develop a better understanding of the role of magnetic fields in moderating heat conduction in the ICM.

Anisotropic conduction results from the fact that the electron gyroradius is much smaller than its mean free path and renders the ICM atmosphere buoyantly unstable to temperature gradients of either sign, relative to the direction of gravity. The outer region of the ICM, where virialization supports a negative temperature gradient, falls subject to the magnetothermal instability (MTI; [Balbus, 2000](#)). On the other hand, in the inner region of cool-core clusters the plasma density is high enough for bremsstrahlung cooling to turn over the temperature gradient and the atmosphere is unstable to the heat-flux driven buoyancy instability (HBI; [Quataert, 2008](#), hereafter Q08).

Previous studies of the local non-linear evolution of the HBI using numerical simulations ([Parrish and Quataert, 2008](#); [McCourt et al., 2011](#)) found that the instability acts to quench vertical heat conduction by wrapping magnetic field lines horizontally thereby insulating each temperature layer from one another. If this strong insulation effect occurs in real clusters, it renders thermal conduction irrelevant in consideration of the thermal energy balance of the cooling core.

In the absence of significant conduction, one must invoke AGN feedback or another type of turbulent stirring to stave off catastrophic cooling, but any such mechanism would simultaneously reorient some field lines vertically and conduction would again drive turbulence via the HBI. Therefore any self-consistent model of the ICM needs to both realistically capture the physics of the HBI as well as feedback

processes (Balbus and Reynolds, 2008; Sharma et al., 2009; Parrish et al., 2010; Kunz et al., 2011).

The HBI is fundamentally a weak-field instability, operating even when magnetic forces are completely negligible (provided that the field is strong enough to keep the electron gyroradius smaller than its mean free path). For this reason, most previous studies of the HBI have assumed extremely weak initial fields, $\beta \gtrsim 10^{11}$ where $\beta \equiv P/P_{\text{mag}}$ with P being the thermal plasma pressure and P_{mag} the magnetic pressure. However, the role of magnetic field/tension on the non-linear behavior of the HBI is poorly understood. Kunz et al. (2012, hereafter K2012) performed semi-global HBI runs with initial $\beta = 10^5$ and found a qualitatively different behavior to that seen previously. Instead of the field line wrapping and quenching of conduction seen by previous authors, K2012 found sustained conduction via magnetic filaments. However, it was unclear whether the semi-global nature of the simulation or the stronger initial field was the main cause of this difference.

This leaves open several questions. Does magnetic tension play a defining role in shaping the non-linear behavior of the HBI? Since tension forces are most relevant for highly curved field lines, is the numerical resolution typically used in simulations sufficient to fully capture the physics of the HBI? What role do magnetic filaments play in the transport of heat in the ICM?

In this paper we present new 2-d simulations in the local regime which cover the resolution- β parameter space in an attempt to answer these questions. We explore how the non-linear dynamics of the weakly collisional ICM changes as the initial magnetic field strength is varied from complete convective stability (HBI completely suppressed by magnetic tension at the local scale) to the low field strength used in previous studies. In order to determine whether current simulations have sufficient grid resolution for all aspects of the physics of the HBI to be fully converged, we also study trends in fundamental measures of the non-linear state of the plasma as grid resolution is varied.

We principally find that, as suggested by inviscid simulations of K2012, the non-linear state of the HBI is qualitatively different than in previous studies when an

intermediate (within a few orders of magnitude of HBI stability) initial magnetic field strength is chosen. In particular, there is enough magnetic flux to form sustained vertical filaments which prevent the quenching of vertical heat conduction in the ICM, saturating at a significant fraction of the Spitzer conductivity (Spitzer, 1962). We present the results of our parameter space exploration and describe new insights into the physics of HBI growth as well as the formation of magnetic filaments, including a connection between the non-linear turbulent state of the plasma and the linear theory. Our results hold for moderate resolution 3-d simulations, validating the applicability of a 2-d study and the physical model we present.

The paper is organized as follows. In §5.2 we briefly review the analytic description of the HBI focusing on aspects relevant for our results. In §5.3 we discuss the numerical method, boundary conditions, and initial conditions. §5.4 presents the results of the simulations and describes major trends we observe, which are then placed into context of the physics of the HBI in §5.5. In §5.6 a complimentary 3-d simulation of moderate resolution is described, and §5.7 provides a discussion of our work in the context of existing literature.

5.2 MHD of Weakly Magnetized Plasmas

We use the standard MHD equations with a term added to the entropy equation for anisotropic thermal conduction along magnetic field lines. For easy comparison to recent literature we primarily follow the prescription for linear analysis laid out in Balbus and Reynolds (2010, hereafter BR10) while excluding the term for radiative cooling.

We choose rationalized natural units with $k_B = c = \epsilon_0 = \mu_0 = 1$ such that total energy density is given by

$$E = \epsilon + \rho \frac{\mathbf{v} \cdot \mathbf{v}}{2} + \frac{\mathbf{B} \cdot \mathbf{B}}{8\pi} - \frac{\rho \mathbf{g} \cdot \mathbf{x}}{(\gamma - 1)} \quad (5.1)$$

with the internal (i.e., thermal) energy density $\epsilon = P/(\gamma - 1)$, where we assume the adiabatic index $\gamma = 5/3$ and the mean molecular weight $\mu = 1$ (pure hydrogen, fully ionized, plasma). The third term on the right hand side is the magnetic energy

density, or pressure, used in the definition of the plasma β -parameter

$$\beta = \frac{8\pi P}{B^2}. \quad (5.2)$$

The vector quantity $\mathbf{x} = x\hat{x} + z\hat{z}$ defines position in the 2-d simulations. \hat{z} points vertically upward and \hat{x} points horizontally to the right. Then, the mass conservation, momentum conservation, induction, and entropy equations are, respectively,

$$\frac{\partial \rho}{\partial t} + \nabla \cdot (\rho \mathbf{v}) = 0, \quad (5.3)$$

$$\rho \frac{D\mathbf{v}}{Dt} = \frac{(\nabla \times \mathbf{B}) \times \mathbf{B}}{4\pi} - \nabla P + \rho \mathbf{g}, \quad (5.4)$$

$$\frac{\partial \mathbf{B}}{\partial t} = \nabla \times (\mathbf{v} \times \mathbf{B}), \quad (5.5)$$

$$\frac{D \ln P \rho^{-\gamma}}{Dt} = -\frac{\gamma - 1}{P} \nabla \cdot \mathbf{Q} \quad (5.6)$$

where ρ is the mass density, \mathbf{v} is the fluid velocity, \mathbf{B} is the magnetic field vector, P is the gas pressure, \mathbf{g} is the gravitational acceleration, and \mathbf{Q} is the conductive heat flux. $D/Dt \equiv \partial/\partial t + \mathbf{v} \cdot \nabla$ is the Lagrangian derivative.

We define the anisotropic conductive heat flux \mathbf{Q} , with $\mathbf{b} = \mathbf{B}/B$ the unit vector in the direction of the magnetic field, as

$$\mathbf{Q} = -\chi \mathbf{b}(\mathbf{b} \cdot \nabla)T, \quad (5.7)$$

where T is the kinetic gas temperature and

$$\chi \simeq 6 \times 10^{-7} T^{5/2} \text{ erg cm}^{-1} \text{ s}^{-1} \text{ K}^{-1}$$

is the thermal conductivity (Spitzer, 1962) in physical units. As in Q08 and BR10 we define $\kappa \equiv \chi T/P$ to be the anisotropic thermal diffusion coefficient. In natural units, $\kappa \approx 10^{-2}$ is the Spitzer diffusion coefficient for a plasma of temperature 1 keV.

We ignore the ion component of the heat flux since it is smaller than the electron contribution by a factor of $(m_i/m_e)^{1/2} \approx 42$. Kunz et al. (2011) showed that, despite this large ratio, viscosity can have a significant effect on the HBI for conductivity at the Spitzer value, as chosen here, but that this effect is severely

diminished deep in cluster cores where the plasma is most collisional. For this work, we choose not to include viscosity so that we may probe the connection between the formation of magnetic filaments and the conduction driven physics of the HBI alone. Regardless, the presence of anisotropic viscosity seems to only enhance the formation of filaments (Parrish et al., 2012).

5.2.1 Background Equilibrium Conditions

We consider a vertically stratified atmosphere in which the gas is not self-gravitating and the extent of the domain is small enough to be in the local regime. We then approximate the gravitational acceleration to be a constant function of position $\mathbf{g}(z) = -g_0\hat{z}$.

The initial (unperturbed) magnetic field is purely vertical for all simulations presented. The simulations start with equilibrium initial conditions in which magnetic pressure is negligible compared to the thermal pressure. Moreover, a uniform initial field provides zero magnetic pressure gradient so field strength does not affect the equilibrium condition at all. Therefore the equilibrium state of the atmosphere is that of hydrostatic balance with

$$\frac{dP}{dz} = \mathbf{g}(z)\rho = -g_0\rho. \quad (5.8)$$

Given an initial temperature profile $T(z)$, in order to show distinction between that of the HBI and that of the classical adiabatic (Schwarzschild) instability, we employ profiles that have entropy increasing with height, i.e., that are Schwarzschild stable. Thus, as will be shown in §5.3, we assume a simple power law representation for equilibrium temperature and density such that $\partial s/\partial z > 0$ where the entropy s is

$$s = \frac{P}{\rho^\gamma}.$$

5.2.2 Stability analysis

We refer the reader to BR10 for a full construction of the Wentzel-Kramers-Brillouin (WKB) perturbation analysis using plane wave disturbances of the form

$\exp(\sigma t + i\mathbf{k} \cdot \mathbf{x})$ where \mathbf{x} is the position vector, σ is the formal growth rate, and the wavenumber \mathbf{k} has Cartesian components. However, there are a few points in the analysis which are particularly relevant to the results in this paper.

Without cooling, the linear analysis in BR10 results in the following dispersion relation:

$$(\sigma + C)(\sigma^2 + (\mathbf{k} \cdot \mathbf{v}_A)^2) \quad (5.9)$$

$$+ \frac{\sigma k_\perp^2 N^2}{k^2} + CK \frac{g}{k^2} \frac{\partial \ln T}{\partial z} = 0, \quad (5.10)$$

where

$$C \equiv \left(\frac{\gamma - 1}{\gamma} \right) \kappa (\mathbf{k} \cdot \mathbf{b})^2, \quad (5.11)$$

$$K \equiv (1 - 2b_z^2)k_\perp^2 + 2b_x b_z k_x k_z, \quad (5.12)$$

and the Brunt-Vaisala frequency, N , given by

$$N^2 = -\frac{1}{\gamma \rho} \frac{\partial P}{\partial z} \frac{\partial \ln s}{\partial z}, \quad (5.13)$$

describes the buoyant response of an adiabatic plasma. k_\perp is the component of \mathbf{k} perpendicular to the magnetic field direction. The square of the Alfvénic frequency is $\omega_A^2 \equiv (\mathbf{k} \cdot \mathbf{v}_A)^2$.

This cubic dispersion relation encodes three conditions for stability, one of which encodes the HBI and MTI criterion of [Balbus \(2000\)](#) and Q08,

$$K \frac{g}{k^2} \frac{\partial \ln T}{\partial z} + \omega_A^2 > 0, \quad (5.14)$$

where it is convenient to identify the characteristic dynamical timescale with the HBI/MTI growth rate (e -folding rate), $\omega_{dyn}^2 \equiv g \frac{\partial \ln T}{\partial z}$. Eqn. (5.14) then simplifies, in a purely vertical magnetic field, to

$$-\frac{k_\perp^2}{k^2} g \frac{\partial \ln T}{\partial z} + \frac{B^2}{4\pi\rho} (\mathbf{k} \cdot \mathbf{b})^2 > 0 \quad (5.15)$$

This equation is essentially a quantification of the competition between the effects of a destabilizing temperature gradient and the stabilizing influence of magnetic tension.

5.3 Numerical Setup

For our simulations we use the ATHENA MHD code (Stone et al., 2008) which uses an unsplit Godunov method utilizing constrained transport (Gardiner and Stone, 2005) to preserve the divergence free nature of a physical magnetic field. To prevent unphysical transport of heat against ∇T we add a monotonic flux limiter to our problem algorithm according to the scheme laid out in Sharma and Hammett (2007).

Atmospheres unstable to the HBI are those with a positive temperature gradient. To achieve this condition and maintain positive entropy gradient we set up the initial equilibrium configuration with temperature, density, and pressure given by power laws of the form

$$T(z) = T_0 \left(1 + \frac{z}{H_T}\right) \quad (5.16a)$$

$$\rho(z) = \rho_0 \left(1 + \frac{z}{H_T}\right)^{-2} \quad (5.16b)$$

$$P(z) = P_0 \left(1 + \frac{z}{H_T}\right)^{-1}, \quad (5.16c)$$

with $H_T \equiv (d \ln T / dz)^{-1} = 2$ the characteristic scale height of the atmosphere with sound speed $c_s \equiv \sqrt{\gamma P / \rho} \approx 1.3$. From hydrostatic equilibrium, with $g = 1$, we have $T_0 = 2\rho_0 = P_0 = 2\mu = 2$ and we choose an initial magnetic field oriented purely vertically ($\mathbf{B} = B_0 \hat{z}$).

This equilibrium configuration has a conductive heat flux that is divergence free,

$$\frac{d}{dz} \left(\chi_{\parallel} \frac{dT}{dz} \right) = 0, \quad (5.17)$$

since we choose a constant value for the parallel component of thermal conduction, χ_{\parallel} . Aside from ensuring that the HBI will develop with the same growth rate everywhere in the anisotropically conducting part of the atmosphere, since our models do not account for radiative cooling and zero-divergence implies no heating, the atmosphere is initially in thermal equilibrium.

Our simulations have dimensionless width \times height of 0.1×0.3 and we limit

anisotropic conduction and all our measurements of the gas dynamics to the central 0.1×0.1 region. The remaining 0.1×0.1 buffer zones above and below have isotropic conduction of the same magnitude as conduction in the active central zone. Early testing revealed the vertical reflective momentum boundary condition to cause suppression of the vertical growth by deflecting motion of the plasma before it naturally reached a non-linear state, but addition of buffer zones of this size alleviates the effects of the boundaries.

We choose momentum reflective boundary conditions for the upper and lower boundaries to provide mass conservation and pressure support. Periodic boundary conditions are chosen for the left and right boundaries. The temperature is held constant at the upper and lower boundaries where the magnetic field vector is set identically to that in the last active cell for each column. This magnetic boundary condition conserves total vertical magnetic flux.

In order to resolve the linear development of the HBI cleanly, we applied single-mode perturbations to the equilibrium atmosphere in most of our simulations. For consistency, we tested the dependence of our results on the perturbation spectrum by running a set (the H2d128_xPS series) of simulations with identical initial conditions but a power spectrum perturbation in momentum with $|v_k|^2 \propto k^{-\alpha}$ of Kolmogorov type, $\alpha = 5/3$. This produces a non-linear magnetic field topology approximately the same as a pure-mode perturbation where two wavelengths fit in each direction in the central square box. For all simulations exploring the β -resolution parameter space we start with a single pure-mode in both velocity and magnetic field of magnitude $k_x = k_z = 4\pi/0.1$.

We performed 24 simulations to cover the β -resolution parameter space and use the designation H2d128_5, for example, to label our 2-d HBI simulation with a resolution (covering the active region) of 128×128 and an initial plasma β -parameter of $\beta = 2 \times 10^5$. To connect our work with both linear theory and previous studies we chose five values of $\log_{10}(\beta) \sim 3, 5, 7, 9$ and 11, and five grid resolutions $R \times 3R$ where $R = [32, 64, 128, 256, 512]$ ¹. In addition to these 24 simulations we ran a

¹We chose not to use limited computing resources on the 25th simulation, H2d512_3, since the

power spectrum simulation of resolution 128×384 for each β and a 3-d simulation of resolution $128 \times 128 \times 384$ of $\beta = 2 \times 10^7$.

5.4 Plasma Behavior as a Function of Resolution and β

In this section we show the results of our β -resolution parameter space study. We first describe the effect of varying β (i.e., only changing magnetic field strength) on the non-linear saturation of the HBI. We then show the dependence of these effects, and evidence for general convergence of the physics of the HBI, with the grid resolution.

As a precursor to our discussion of the full parameter space, we show in the first two frames in Figures 5.1a and 5.1b the temperature and magnetic field structure of our atmosphere under the pure-mode perturbation. These frames show the entire height of the atmosphere at times when the HBI is in the linear growth phase and just reaching the non-linear regime. Note that for both simulations of Fig. 5.1a and 5.1b, corresponding to values of $\beta = 2 \times 10^7$ and 2×10^9 respectively, the linear growth phase appears identical, in agreement with the expectations of the linear theory.

Now we focus attention on the development of the HBI into the nonlinear regime illustrated in the late-time frames of Figures 5.1a and 5.1b.

5.4.1 Plasma β

Central to any study of the ICM is the plasma β -parameter. In the context of these simulations, consider the fully non-linear state of the plasma shown in the later frames in Figure 5.1. The simulation with a moderate initial value of $\beta \approx 10^7$ (H2d128.7) contrasts qualitatively to that with $\beta \approx 10^9$ (H2d128.9).

The major qualitative difference is that magnetic flux bundles, or *filaments*, are present near the end of the linear phase in both simulations, but persist over many dynamical times only in the moderate β case (2×10^5 and 2×10^7). These HBI is stable for that value of β and no dynamics is seen for any grid resolution.

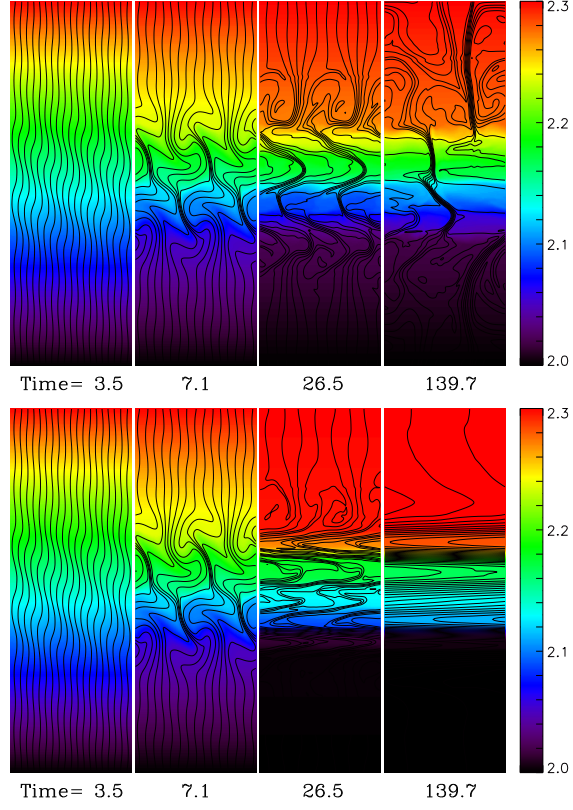


Figure 5.1: (a) H2d128_7 at four times (in units of dynamical times, ω_{dyn}^{-1}). The color bar on the right indicates temperature and magnetic field lines are overlaid. (b) H2d128_9 at identical times as (a). Note the clear distinction between the two after many dynamical times, shown in the last frames.

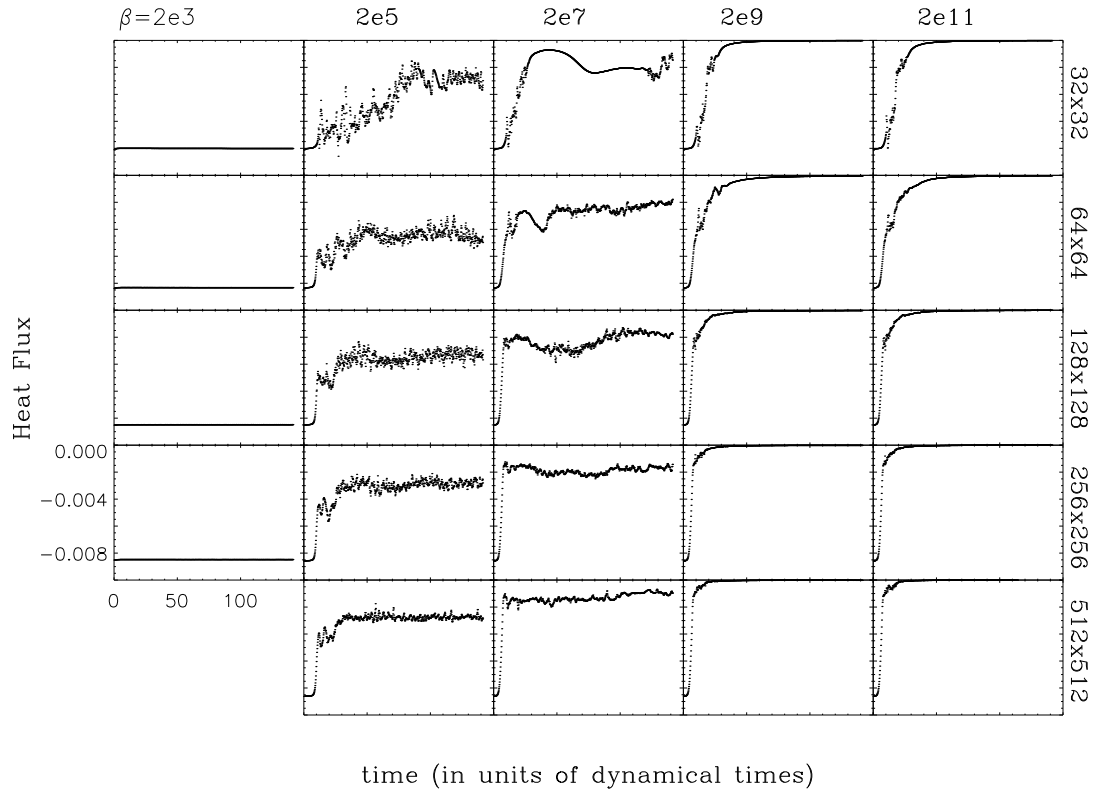


Figure 5.2: Horizontally averaged vertical heat flux as a function of time for 24 simulations described in the text. Each panel in the plot has identically scaled axes.

filaments have been seen before as the seeds of the horizontal bands of magnetic field lines which develop in high β simulations. Horizontal motion, free from any restoring force (see [McCourt et al., 2011](#), for discussion), wraps the magnetic field lines thereby insulating temperature layers from one another and continuously growing in magnetic field strength. However, for the moderate values of β these filaments persist against horizontal bulk motion and reach an entirely different saturated state.

The most important physical quantity characterizing the system, and an excellent discriminator of the different non-linear states, is the vertical heat flux (VHF),

$$F_z = - \int_S \chi \hat{b}(\hat{b} \cdot \nabla) T \cdot dS,$$

where S is a surface that cuts horizontally across the domain. Figure 5.2 shows the horizontal average of the VHF across the center of the active domain ($z = 1.5$) as a function of time for all simulations in the pure-mode study. The column containing those simulations stable to the HBI shows constant heat flux consistent with the magnetic field remaining vertical and conducting uniformly. The two intermediate β columns show a nonzero heat flux in the saturated state. As shown in Fig. 5.1, the HBI has shut off VHF in most of the plasma, but the filaments remain vertically oriented against the turbulent motion of the plasma and support a sustained VHF. The higher initial magnetic field strength results in a larger magnitude of sustained VHF, which we explain via the physical model for the filaments described in §5.5. Finally, the high β simulations lead to a non-linear state with zero VHF, duplicating the result of previous studies. Thus, one can identify the behavior in Fig. 5.1a with the 2nd and 3rd columns of Figure 5.2, and Fig. 5.1b with the last two.

Another interesting quantity is kinetic energy. In order to study energy equipartition and turbulence in an inherently asymmetric atmosphere we break the kinetic energy scalar into the components contributed by motion in each direction, $KE_z \equiv \frac{1}{2}mv_z^2$ and $KE_x \equiv \frac{1}{2}mv_x^2$. Figure 5.3 shows how $\langle KE_z \rangle$, the vertical kinetic energy contribution spatially averaged across the entire active central region, varies with β . H2d256_9 and H2d256_11 show approximately linear damping of vertical motion, but H2d256_5 and H2d256_7 show an increase in vertical momentum with

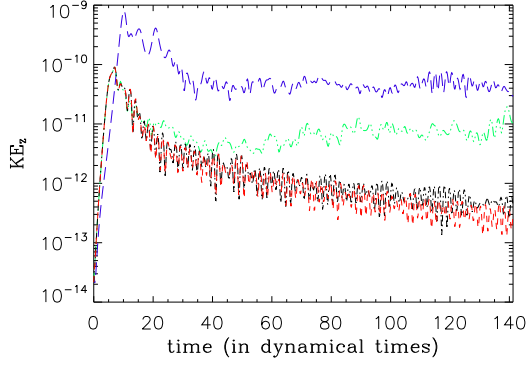


Figure 5.3: The contribution to kinetic energy from vertical motion spatially averaged across the entire anisotropically conducting region is shown as a function of time for simulations H2d256_x, $x \sim [5$ (*blue-long-dash*), 7 (*green-dash-dot-dot-dot*), 9 (*black-dash-dot*), 11 (*red-dash*)].

higher initial magnetic energy density. Both H2d256_5 and H2d256_7 saturate at a value orders of magnitude above the weak field cases, where the vertical momentum does not stop declining up to the end of our simulations.

However, the kinetic energy is not the only energetic discriminant for the non-linear behavior of the plasma. Fig. 5.4 shows the vertical and horizontal contributions to the volume integrated magnetic and kinetic energy within the anisotropically conducting region. For $\beta = 2 \times 10^9$ the kinetic energy completely dominates the dynamics of the plasma early on as horizontal motion wraps the field into layers. It is only at late times when the field wrapping has transferred enough energy into the magnetic field for the horizontal component $B_x^2/8\pi$ to overcome KE_x .

The moderate β columns in Fig. 5.4 show something very different. For sufficient resolution there is approximate equipartition between $B_x^2/8\pi \approx KE_x \approx KE_z$. In fact, for initial $\beta = 2 \times 10^7$, even $B_z^2/8\pi$ reaches equipartition with the other energy components. In general, however, $B_z^2/8\pi$ is subject to a special constraint, namely total vertical magnetic flux through the simulation domain is conserved, and so does not necessarily come into equipartition.

While the simulations start with four different initial field strengths spanning

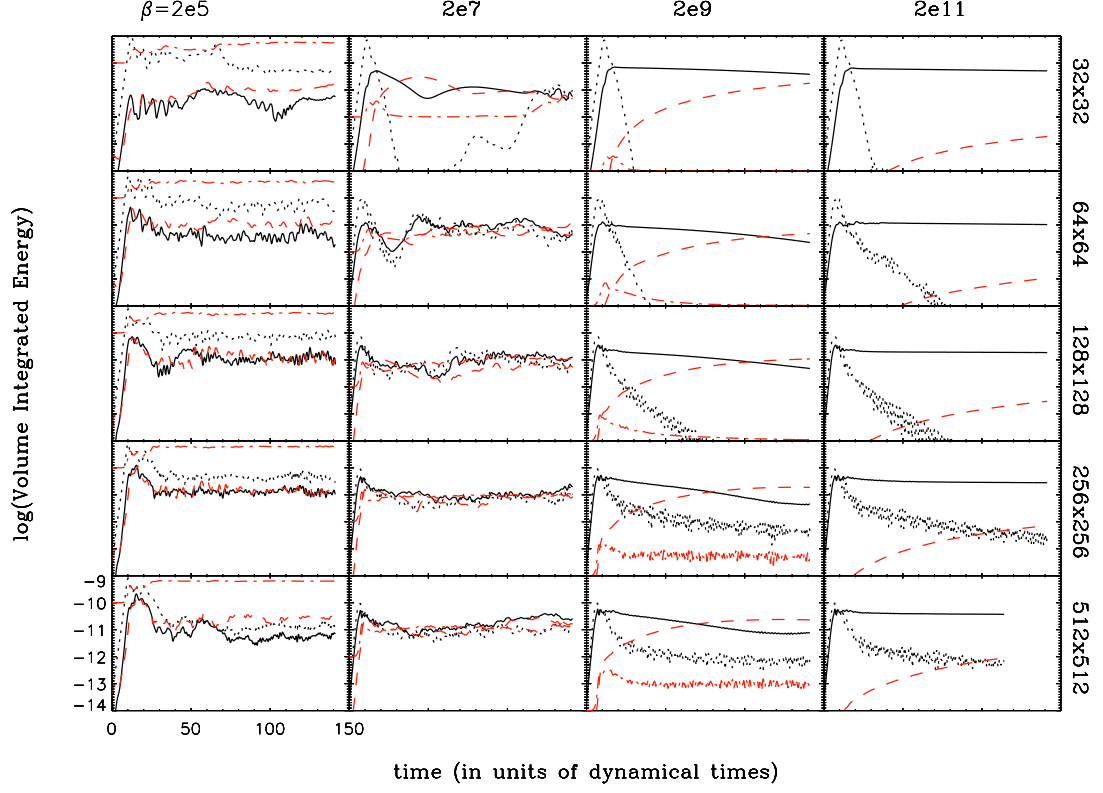


Figure 5.4: Evolution of energy components, in our rationalized units, volume integrated over the active (central) region of the computational domain of dimensions $0.1 \times 0.1 \times 0.001$. The last dimension is the arbitrary skin depth we choose for the compact third dimension. Only results of HBI unstable simulations are shown, namely, those for $\beta = 2 \times 10^3$ are omitted. KE_x kinetic energy (*black-line*), KE_z kinetic energy (*black-dotted*), $B_x^2/8\pi$ magnetic energy (*red-dash*), and $B_z^2/8\pi$ magnetic energy (*red-dash-dot*). Each panel in the plot has identically scaled axes.

four orders of magnitude, the total of all the energy components (excluding $B_z^2/8\pi$) is the same for all simulations with resolution at least 64×192 , whether filaments are sustained or not. This is expected from the linear theory since the linear growth rate of pure-mode perturbations is independent of magnetic field strength (in the weak-field limit) and the linear growth entirely determines the amount of kinetic energy at the time of transition into the non-linear regime. From inspection of Fig. 5.4 it seems that the balance between volume integrated kinetic and magnetic energy soon after transition into the non-linear regime is an indicator of whether or not filaments are sustained. This makes sense as an excess in KE is necessary to overcome the tension within the filaments. Production of sustained filaments is intimately tied to the total kinetic energy, and thus the turbulent state of the plasma.

5.4.2 Grid Resolution

Now we consider the more subtle effect of grid resolution as well as its interplay with β . The amplitude of VHF in the two intermediate β columns of Fig 5.2 decreases with increasing resolution. This is illustrated in Fig. 5.5 where the conduction rate vs. time for the $\beta = 2 \times 10^7$ column at all five grid resolutions is smoothed and plotted in superposition. Inset is the time-averaged value of conduction during the last 18 dynamical periods for each resolution for $\beta = 2 \times 10^5$ and 2×10^7 . One can see that for $\beta \sim 10^5$ there is negligible change in heat flux for the last doubling of resolution. However, for $\beta \sim 10^7$ there is no such sign of convergence. While the data are too sparsely sampled in resolution to conclusively make this distinction, it is consistent with the general physical model of the filaments we propose in the next section.

Dependence on grid resolution is also evident in Fig. 5.4. Firstly, for moderate β , increasing resolution produces less dispersion in the values of the four volume integrated energy components. Secondly, for high β simulations there is an increase in the vertical energy components with increasing resolution. This second effect could be due to the resolution of small scale turbulence.

For high β simulations it also takes less time with increasing resolution for

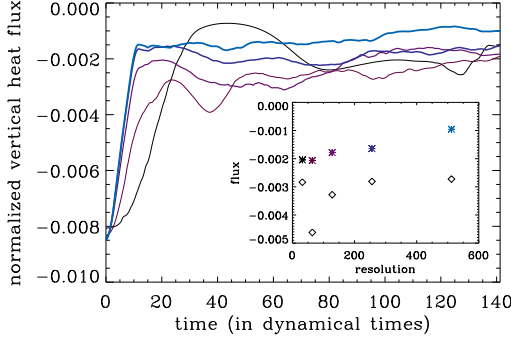


Figure 5.5: Arbitrarily scaled, horizontally averaged vertical heat flux plotted in the $\beta \sim 10^7$ column of Fig. 5.2 versus time in dynamical units. Colors, in order of transition from black to blue, signify increasing resolution. *Inset:* Each data point represents the flux averaged over the last $18\omega_{dyn}^{-1}$ for each grid resolution. Convergence is shown for simulations with initial $\beta \sim 10^5$ (diamonds) but not $\beta \sim 10^7$ (stars).

KE_x and $B_x^2/8\pi$ to switch dominance. This is consistent with a lower level of numerically driven magnetic reconnection in the higher resolution simulations and the regions of highest magnetic field curvature. Finally, in the $\beta = 2 \times 10^5$ column, increasing resolution results in a lower saturated value of KE_z . In these simulations a significant fraction of the vertical motion is bulk flow along the filament, similar to what was seen in the filaments of K2012. We do not elaborate on the flow in this study, but it suffices here to simply say the width of filaments is observed to decrease with increasing resolution. Thus, the volume integrated KE_z as well as the resolution dependence of VHF can be explained by a dependence of filament width on resolution. In the next section we present a physical model for the filaments and explain their dependence on the β -resolution parameter space.

5.5 Dynamics and Persistence of Filaments

Why do filaments form and what sets their field strength and width? We hypothesize that filaments are the result of needing to pass a (conserved) vertical

magnetic flux through a plasma subject to an instability which attempts to remove vertical field. We suggest that the filaments collapse until their internal field strength renders them HBI stable, with further collapse likely prevented by the diffusive process of turbulence.

Without viscosity, a plasma governed by ideal MHD will be driven by turbulent motions toward equipartition of the total kinetic and magnetic energies via field amplification. Therefore, after the filaments are produced, if the kinetic energy density is sufficiently higher than the magnetic energy density, the large scale bulk motions of the plasma (preferentially horizontal since the atmosphere is classically Schwarzschild stable) will wrap up the magnetic field into horizontal layers. If, on the other hand, the magnetic field dominates overall, most magnetic flux is vertical and the filaments are sustained. While the detailed dynamics of filament stability against the turbulent motions of the plasma could be framed in terms of horizontal velocity shear and height of the filaments, the complex magnetic topology and boundary limitations of the simulations suggest more insight may be gleaned from an understanding of filament persistence in terms of globally averaged quantities. Therefore, our model presents a global energetics understanding of filament persistence, and a separate model for filament width and field strength in terms of the HBI. This separation is natural since perturbations of wavelength greater than about twice the width of the filament are better understood geometrically in terms of bending the flux tube than in terms of the linear HBI.

A direct prediction of our model is that simulations should show that filaments lie on the stable side of the threshold between stable and unstable regions of phase space. Fig. 5.6 shows the result of such a measurement, obtained via the method we now describe.

First consider the size of the filaments. Our hypothesized model predicts filaments will have a width corresponding to a wavenumber which just satisfies HBI stability, i.e., the filaments are stabilized when $\omega_A^2 > \omega_{dyn}^2$ for a region inside the filaments of size equivalent to the scale of a random perturbation.

In our analysis for Fig. 5.6, we must be able to define and characterize filaments

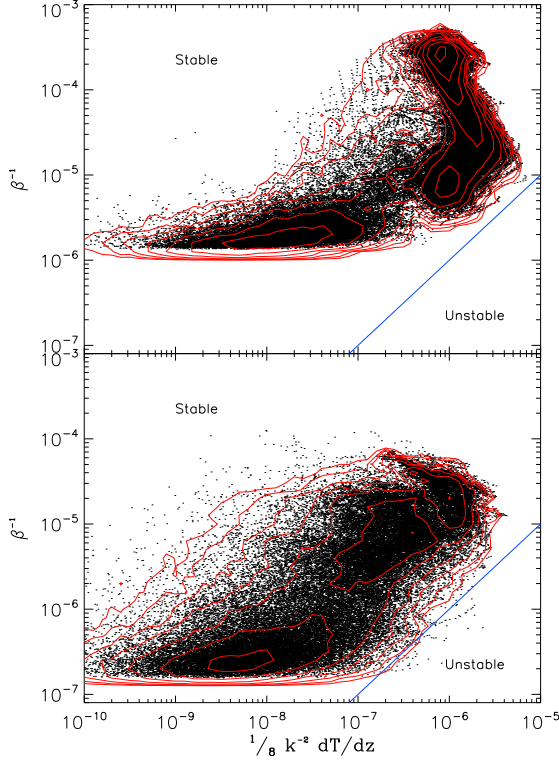


Figure 5.6: H2d512.5 (upper) and H2d512.7 (lower) filaments. Stability of the filaments is demonstrated by plotting the three stability diagnostics of Eqn. (5.19) measured for each filament. Phase space below the solid line is HBI unstable, above is stable. The data points are evenly temporally sampled from the last $35.4\omega_{dyn}^{-1}$. Those plotted are a subset of all extracted, for visual clarity, but the contours represent all the data and enclose $2^{[4,5,\dots,17]}$ points.

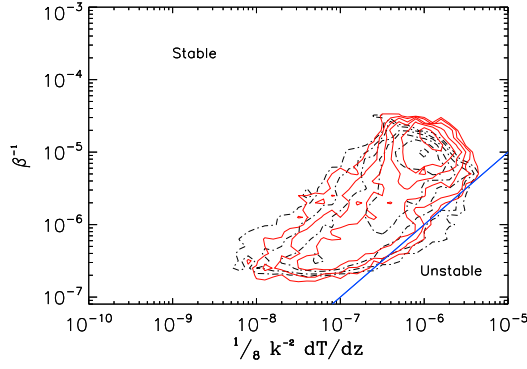


Figure 5.7: Black contours (dash-dot) represent filaments from H2d128_7PS; red (solid) represent those from H2d128.7. Contour levels are set the same as in Fig. 5.6.

in an automated manner. We consider a filament to be located wherever a series of horizontally adjacent grid cells satisfy both $|\hat{b}_z| > 0.7$ and $\beta_{cell} < 0.1\langle\sqrt{\beta}\rangle^2$, a weighted average of β over the active domain. The values of magnetic energy (for which we can use β^{-1} as a proxy since the average thermal pressure varies at most by 2%), the vertical component of the temperature gradient, $\frac{dT}{dz}|_z$, and the filament width, which we identify with wavenumber k_w , are extracted for each such collection of cells for all but the rows of our anisotropically conducting active region directly adjacent to the buffer regions. Each set of values produces a point in Fig. 5.6. In the plot the k_w value used is calculated assuming a wavelength set at twice the measured width of the filament. The values of vertical temperature gradient within the filament and β^{-1} are unweighted horizontal averages across the filament-defining cells.

If we assume b_x is close to zero, which is generally observed to be the case for sustained filaments, then it follows that $K = -k_\perp^2$. If we additionally assume $k_\perp \approx k_\parallel$ for an average perturbation, then $2k_\parallel^2 \approx k^2$, and Eqn. (5.15) simplifies to

$$-\frac{1}{2} \frac{g}{T^2} \frac{dT}{dz} + \frac{1}{\beta} k^2 > 0. \quad (5.18)$$

This provides a general relation giving the boundary of HBI stability in terms of our three diagnostic measures of the filaments. In order to facilitate comparison of the

relation with the data in Fig. 5.6 we further simplify by setting $T = 2$, in our local simulations where temperature does not significantly spatially vary. Also, since the width of the filament is the scale at which it is stabilized to random perturbations under our model, we identify k as the width k_w . We then obtain

$$\beta^{-1} \sim \frac{1}{8} \frac{dT}{dz} k_w^{-2}. \quad (5.19)$$

In Fig. 5.6 data points created in the method just described are extracted from the active region for the last $\sim 35 \omega_{dyn}^{-1}$ of the simulation at 200 evenly spaced times. The magnetic filaments are clearly subject to the boundary provided by the stability relation, thus supporting the theory that the filaments are islands of HBI stability within an otherwise HBI susceptible plasma. Specifically, consider how the filaments in H2d512_7 and H2d512_5 are scattered along the stable side of the curve but generally follow it. While there is a significant vertical spread in β^{-1} above the line, consider that initial values in these simulations were $\beta^{-1} = 5 \times 10^{-8}$ and 5×10^{-6} and the final spread in β^{-1} above the intra-filament value is consistent with the theoretical boundary over nearly three orders of magnitude. Note that some filament values of β^{-1} fall below the initial conditions value. This is consistent with our definition of a filament having significant internal magnetic energy density over the spatial average, and most space in the atmosphere has a very weak field in the saturated state.

Figure 5.7 compares filaments from H2d128_7 and H2d128_7PS showing that they cover roughly the same region in this space. This suggests the pure-mode perturbation recovers most of the physics of a more multi-mode initial condition, and both lie at weaker field strengths than the simulations with higher resolution, suggesting the filaments in the lower resolution simulation are prevented from shrinking to obtain their natural peak field strength. This picture is also consistent with the H2d128_7 data points residing at the higher values of k_w^{-2} on the plot.

This self-consistent model for the internal stability of the filaments is sufficient to explain the width of the filaments and their dependence on magnetic field strength and resolution, as we've shown. However, it also predicts the viability of magnetic

filaments in a plasma of arbitrarily weak magnetic field so long as there is sufficient resolution for the filament to shrink until it becomes internally HBI stable. This would predict that the boundary between our qualitatively different non-linear states would shift to higher β as resolution is increased in Fig. 5.5. While it is likely we inadequately resolve the β -resolution phase space to see such a trend to begin with, the true dissolution of this discrepancy is evident upon closer inspection of the global energetics in our simulations.

Recall that both the two intermediate and two high β columns of Fig. 5.2 are well within the weak-field regime (See §5.2). The growth rate then only depends on the pure-mode perturbation wavelength, which is identical for all simulations in our phase-space suite. Transition to non-linearity happens at the same time in all cases, and the exponential growth in momentum during the linear phase is driven by a conversion of heat into kinetic energy. These facts together imply that the total kinetic energy imprinted on the plasma at the end of the linear regime is the integrated net heat-flux passing into the active region during that time. For these reasons, and evident in Fig. 5.4, the peak in kinetic energy at the end of linear growth is identical in all the simulations. Those with initial $\beta \sim 10^5$ do have a slightly higher transition value, but that is consistent with the additional magnetic tension maintaining a pure-mode magnetic topology for slightly longer, therefore increasing the time over which the energy conversion takes place. Clearly the peaks in KE components for that column occur at later times than in the other columns.

In the second part of our model we suggest that the global persistence of filaments once they’ve formed depends on how the imprinted kinetic energy just described compares to the initial total magnetic energy. We argue that if approximately twice the magnetic energy density is greater than the kinetic energy density imprinted at the transition to non-linearity, then sustained vertical filaments of the form we see will be present. This is effectively a statement that either the magnetic field or the turbulent motion dominates and one or the other wins out early in our simulations, leading to a distinct division in parameter space. The ‘twice’ comes from allowing an x-component of the filaments to grow to equal magnitude

with the vertical z -component. Beyond that, the filament would be more horizontal than vertical, significantly quench vertical heat flux, and effectively be stretched out beyond our definition of a filament.

This scale-invariant method for understanding filament stability is particularly suited to a local study such as ours. Of course, it suggests that a sustained source of turbulence may significantly alter the non-linear state of the plasma. We leave a discussion of this and other implications for the last section.

5.6 3-D Simulation

Some studies suggest ([Parrish et al., 2012](#)) that the filaments formed in 2-d simulations are a result of field lines not being able to slip past one another, that is, a prevention of flux-interchange modes in the plasma. K2012 comments on this in their H3dBrag simulation, where the filaments become more reoriented (horizontally) in the lower part of the atmosphere where the effects of Braginskii viscosity are less pronounced. However, this region of H3dBrag is very close to the simulation boundary, and the effect of the boundary on the detailed field structure is unclear.

Our model explaining the presence of the filaments, presented in the previous section, suggests this existence is rooted in the physics of the HBI and not a feature of dimensionality. K2012 does not provide a complimentary 3-d semi-global simulation of the HBI without viscosity and so in extension of that work, and to confirm the robustness of our results, we performed a 3-d simulation of 128x128x384 resolution and moderate field strength, H3d128_7PS. The simulation was in every way identical to H2d128_7PS save for the added dimension.

Figure [5.8](#) shows the magnetic structure of the non-linear state of H3d128_7PS at late times, with coherent filaments of a qualitatively similar sort to those found in the 2-d analog. Just as is pointed out in K2012, these filaments contain more magnetic flux because it is easier to collect with the additional dimension during linear growth.

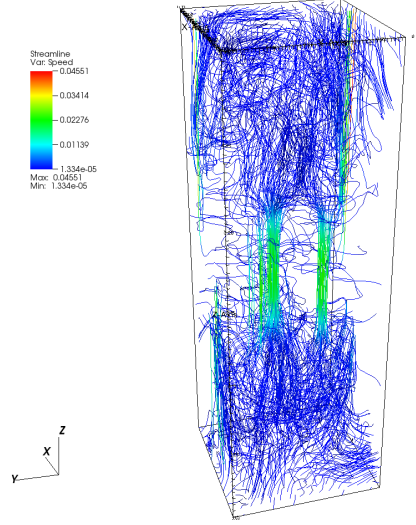


Figure 5.8: Shown is a frame from the saturated state of H3d128_7PS. Color value indicates magnetic field strength and field lines are integrated from grids of points at the top and bottom of the domain. Many of the field lines thread a filament near the center of the anisotropically conducting region.

The VHF measured in the same way as before is shown in Fig. 5.9. H3d128_7PS clearly runs long enough for the VHF to stabilize at a value of $\approx 25\%$ the initial value, just as before. This value is no coincidence. The addition of a third dimension does not change the internally stabilizing β of the filaments, and so the ratio of conducting surface area to non-conducting is still set by the initial plasma β and total vertical flux conservation, assuming that most vertical flux is bundled into the filaments.

5.7 Discussion and Conclusions

In this paper, we present a systematic investigation of the local non-linear behavior of the HBI as a function of initial magnetic field strength and numerical resolution. We identify a previously unrecognized regime of behavior at intermediate field strengths in which magnetic filaments are formed that can resist the horizontal field line wrapping seen in weak-field simulations (Parrish and Quataert,

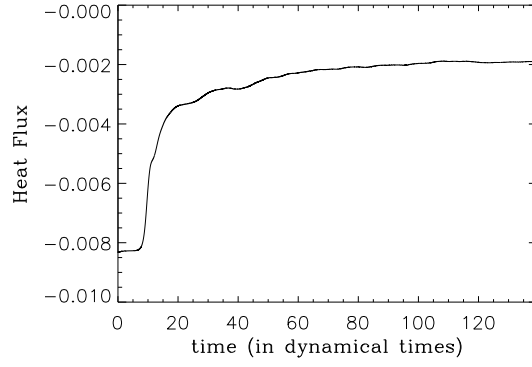


Figure 5.9: Vertical Heat Flux integrated over the horizontal plane slicing through the center of the active domain in H3d128_7PS.

2008; McCourt et al., 2011) and lead to sustained conductive heat flux. We show that the filaments themselves are HBI-stable and provide the main conduit by which (conserved) vertical magnetic flux is passed through the domain. In addition to this model for internal stabilization, we describe how global energetics determine the ultimate qualitative state of the non-linear regime, that is, whether or not filaments persist and there is a resulting significant vertical heat flux.

The robust formation of filamentary structures is tantalizing since we see this type of structure in the cooling cores of galaxy clusters, namely in the form of $H\alpha$ filaments. For instance, HST observations of the Perseus cluster, which has been studied closely for some time (Lynds, 1970), reveal complex braided filaments which can be as narrow as 50 pc but may be kiloparsecs in length (Fabian et al., 2008). More recent observations by McDonald et al. (2010, 2011) have shown that essentially all cool-core clusters exhibit extended $H\alpha$ systems which appear to extend out to almost, but never beyond, the cooling radius of the X-ray emitting ICM. This connection between the cooling radius and the filamentary structure suggests they may condense out of the ICM as a result of thermal instability (Field, 1965).

However, it is the *local* thermal instability which produces cold filaments in simulations, with anisotropic conduction primarily responsible for their filamentary structure. Without a heating source to offset the background global thermal instabil-

ity, namely, when net cooling is purely a function of local density and temperature of the gas, buoyancy effects stabilize the plasma to the local thermal instability (Balbus and Soker, 1989). K2012 shows that for an atmosphere with intermediate magnetic field strength and anisotropic viscosity, viscous heating during formation of the filaments and a sustained vertical heat flux can significantly delay the cooling catastrophe resulting from global thermal instability. This allows local thermal instability to develop and cold filaments to naturally form. Our study supports K2012, firmly establishing the robust formation of filaments over a range in magnetic field strength relevant to cool-core clusters, and exploring in detail the magnitude of vertical heat flux sustained by the atmosphere and its dependence on local magnetic field strength and numerical resolution.

Though our work has not yet shown a definitive connection to the observed $H\alpha$ filaments, in part because we do not include radiative cooling in our simulations, our findings strongly motivate further work in developing physically realistic global simulations of cluster cores, where the ICM is likely HBI unstable. Since filaments provide a mechanism for transporting heat (and possibly cold gas) radially in these atmospheres, an understanding of the magnetic topology from the local to the global scale and how these scales connect will be instrumental in understanding the role of conduction in regulating global thermal stability. Also instrumental is the interplay between the filaments and astrophysical turbulence, since turbulence can ultimately destroy otherwise stable filaments. Our discussion of the presence of filaments as a result of total energy balance provides some insight into the level of turbulence allowed when filaments are present, but more testing, especially on the semi-global and global scales is required.

We find, however, that to fully resolve the physics of the non-linear HBI in the local regime requires a high grid resolution. Thus, feasible global simulations of the ICM may require semi-analytic prescriptions for the dynamics of anisotropic conduction as well as anisotropic viscosity. This study may aid in production of those models since filaments have a key role in the thermodynamics of anisotropically conducting plasma.

Another motivation for this work was to find, if any exist, robust measures for convergence with resolution. Given the intimate connection between the topology of the filaments and more global quantities such as heat conduction, it is not surprising that we find that adequate resolution of the dynamics of the filaments is needed in order to reach convergence in the plasma diagnostics such as VHF and equipartition. The most stringent measure we find is to measure the position of the filaments in HBI stability space presented in Fig. 5.6. However, a much simpler measure that also performs well is to see how much the VHF changes with increasing resolution.

Should the HBI be driving dynamics in relatively large regions of real clusters, numerical studies including this one suggest that it may have a key role in cluster thermodynamics. While there is clearly an interaction between AGN and the ICM (e.g. radio lobes, etc.), it is not known exactly how this feedback may couple effectively to the thermodynamics. This work and K2012 suggest there may still be a potential for conductive solutions to the cooling flow problem. Certainly at this point, the field is still in the exploration stage of the fundamental physical processes which work together to govern the ICM.

M.J.A., C.S.R., and T.B. acknowledge support from the NSF under ARRA grant AST-0908212. Support for T.B. was in part provided by the National Aeronautics and Space Administration through Einstein Postdoctoral Fellowship Award Number PF9-00061 issued by the Chandra X-ray Observatory Center, which is operated by the Smithsonian Astrophysical Observatory for and on behalf of the National Aeronautics and Space Administration under contract NAS8-03060. HPC resources were provided by the Texas Advanced Computing Center (TACC) (Ranger), as well as the UMD OIT (Deepthought) and Dept. of Astronomy (Yorp) clusters. The authors thank Matthew Kunz and Steve Balbus for useful conversations.

Chapter 6: Conclusions and a look forward

The work presented in this dissertation focusing on BH accretion flows around a single BH has addressed several long-standing questions in the field. In the most self-consistent context (i.e. global disk, GRMHD simulation, transport by physical processes rather than added viscosity, etc.) to date we have demonstrated that even a geometrically thin/optically thick disk can accumulate large-scale magnetic flux inward. We have shown that strong poloidal magnetic fields can significantly alter the radiative and total efficiency of the accretion flows. We’ve shown that magnetically arrested disks drive powerful magneto-centrifugal winds. We’ve provided supporting evidence that jets are not truly ‘quenched’ in the high/soft state of XRBs, but that jet power could simply fall below detection limits. Finally, we’ve shown that the MAD state provides a channel, literally, through which super-Eddington radiative flux can escape for potentially arbitrarily high mass accretion rate.

Not only has our work addressed these numerous important questions using state of the art numerical simulations, but more broadly contribute to a much needed understanding of large-scale field effects in accretion systems which may embody a third, primary parameter along with mass accretion rate \dot{M} , black hole mass, and observer viewing angle. This could be crucial to understanding hysteresis in XRBs and jet power in AGN.

However, this work has lead us to pose new problems that necessitate further numerical/analytic and observational considering.

Mass loss and wind

Ongoing analysis of the simulations presented in Chapters 2 and 3 has, in part, focused on the powerful wind. Even at radii of $<50R_g$ the amount of mass flowing

outward in the wind equals the net mass flow inward to the BH. Even though the efficiency of a part of the disk at these larger radii may be smaller, because the available gravitational potential energy is much higher it could contribute significantly to the total radiative efficiency of the system. The efficacy of measuring efficiency of a BH accretion flow by normalizing in terms of mass accretion rate onto the horizon falls into question. While this argument is currently speculative in nature, it strongly motivates further consideration.

The most immediate importance of better quantifying the kinetic and radiative content of the winds is in the context of understanding large-scale feedback. There is an obvious connection between the winds in these simulations, launched from the inner disk at $0.05 - 0.2c$, and ultra-fast outflows (UFOs) (Tombesi et al., 2015; King and Pounds, 2015, and references therein).

Because of the large amount of potential radiative pre-processes by the matter in the wind it may be key to understanding the spectrum of some systems as well, particularly in absorption.

Electro-magnetic spectrum of MAD systems

The truncation of the radiating part of the thin disk at the ISCO and the radiative profile of the NT model is central to BH spin measurements using both the iron line and continuum fitting methodologies. The simplicity of the iron line approach makes it attractive for spectral modeling but its robustness is tightly coupled to how closely the spin-dependence of the ISCO and disk follow the model. If, as we have demonstrated, a thin disk can exist in the MAD state, where the rotation of the flow near the ISCO is very sub-Keplerian and there is no clearly defined ISCO (in fact, magnetic choking of the plunging material may enhance pressure gradients rather than let them fall precipitously as they would free-streaming in the plunging region), then the iron-line method may be unreliable for MAD systems.

Determining spin by fitting the continuum relies on a good understanding of the radial distribution of radiation flux. This also remains poorly understood in thin, MAD systems.

In tidal disruption events, it is still an open question whether the radiation

is primarily reprocessed emission or direct from the disk. In the prior case, both the angular dependence of radiation and optically thick winds can be key to understanding the observations. The fact that some TDEs seem to be jetted suggests that at least some systems could be magnetically dominated at some point in their evolution [Piran et al. \(2015\)](#); [Tchekhovskoy et al. \(2014\)](#).

BH spin / disk misalignment

Coincident with the suit of simulations published in the paper of Chapter 2 was a complimentary set with the same initial conditions and a tilt of the BH spin axis by $\sim 6^\circ$. Preliminary analysis of these simulations suggests a complicated behavior of disk angular momentum that may go through partial alignment episodes, if not sustained alignment or precession. Because of the clumpy and magnetically dominated behavior of these accretion flows, a simple analysis of alignment in the context of traditional studies of the Bardeen-Peterson effect ([Bardeen and Petterson, 1975](#); [Papaloizou and Pringle, 1983](#)) is difficult. An empirical study of these simulations is ongoing and may help to shed light on one of the, most important, but under-studied realms of accretion astrophysics.

Connections to observations

Finally, there has been intriguing recent work connecting the MAD model to observations ([Piran et al., 2015](#); [Zamaninasab et al., 2014](#); [Tchekhovskoy, 2015](#); [Mocz and Guo, 2015](#)). The latter shows that for a sample of AGN across the \dot{M} spectrum, from very sub-Eddington LLAGN to super-Eddington quasars, the simple relation between disk state and magnetic flux threading the horizon could be a powerful probe into AGN population modeling. Now is the time for much more work interweaving theory of magnetically arrested accretion flows and observations.

Building on the foundation of work laid out in this thesis, I plan to continue addressing these open questions in the context of single-BH accretion, with a short-term focus on how our current understanding can be applied to binary BH (BBH) systems. The fundamental processes I’ve studied are present in BBH but with additional complications. For instance, a so-called ‘circum-binary’ disk around two black holes is truncated by tidal interactions with the binary at some radius. In

super massive BBH (SMBBH) systems it could be possible for one or both BHs in binaries to harbor ‘mini’-disks of their own. There are fundamental aspects of these systems that are still not understood and over the next couple years I will use numerical simulations to model the behavior and expected observational signatures of these systems. For SMBBHs these predictions for EM observations are especially important since, at the time this thesis is written, space-based gravitational wave observatories are still years away. Until then, ground-based time-domain observations hold great promise for probing SMBBH systems in conjunction with theoretical developments.

The fields of black hole accretion and multi-messenger astrophysics promise a rich and exciting future, of which I am honored to be a part.

Bibliography

- M. Abramowicz, M. Jaroszynski, and M. Sikora. Title. *A&A*, 63:221–221, 1978.
- M. A. Abramowicz, B. Czerny, J. P. Lasota, and E. Szuszkiewicz. Slim accretion disks. *ApJ*, 332:646–658, September 1988. doi: 10.1086/166683.
- M. A. Abramowicz, X. Chen, S. Kato, J.-P. Lasota, and O. Regev. Thermal equilibria of accretion disks. *ApJ*, 438:L37–L39, January 1995. doi: 10.1086/187709.
- M. J. Avara, C. S. Reynolds, and T. Bogdanović. Role of Magnetic Field Strength and Numerical Resolution in Simulations of the Heat-flux-driven Buoyancy Instability. *ApJ*, 773:171, August 2013. doi: 10.1088/0004-637X/773/2/171.
- M. J. Avara, J. C. McKinney, and C. S. Reynolds. Efficiency of thin magnetically arrested discs around black holes. *MNRAS*, 462:636–648, October 2016. doi: 10.1093/mnras/stw1643.
- X.-N. Bai and J. M. Stone. Local Study of Accretion Disks with a Strong Vertical Magnetic Field: Magnetorotational Instability and Disk Outflow. *ApJ*, 767:30, April 2013. doi: 10.1088/0004-637X/767/1/30.
- S. A. Balbus. Stability, Instability, and “Backward” Transport in Stratified Fluids. *ApJ*, 534:420–427, May 2000. doi: 10.1086/308732.
- S. A. Balbus and J. F. Hawley. A powerful local shear instability in weakly magnetized disks. I - Linear analysis. II - Nonlinear evolution. *ApJ*, 376:214–233, July 1991. doi: 10.1086/170270.
- S. A. Balbus and J. F. Hawley. Instability, turbulence, and enhanced transport in accretion disks. *Reviews of Modern Physics*, 70:1–53, January 1998a. doi: 10.1103/RevModPhys.70.1.
- S. A. Balbus and J. F. Hawley. Instability, turbulence, and enhanced transport in accretion disks. *Rev. Mod. Phys.*, 70:1–53, January 1998b. doi: 10.1103/RevModPhys.70.1.

- S. A. Balbus and C. S. Reynolds. Regulation of Thermal Conductivity in Hot Galaxy Clusters by MHD Turbulence. *ApJ*, 681:L65, July 2008. doi: 10.1086/590554.
- S. A. Balbus and C. S. Reynolds. Radiative and Dynamic Stability of a Dilute Plasma. *ApJ*, 720:L97–L101, September 2010. doi: 10.1088/2041-8205/720/1/L97.
- S. A. Balbus and N. Soker. Theory of local thermal instability in spherical systems. *ApJ*, 341:611–630, June 1989. doi: 10.1086/167521.
- J. M. Bardeen and J. A. Petterson. The Lense-Thirring Effect and Accretion Disks around Kerr Black Holes. *ApJ*, 195:L65, January 1975. doi: 10.1086/181711.
- K. Beckwith, J. F. Hawley, and J. H. Krolik. Estimating the Radiative Efficiency of Magnetized Accretion Disks Around Black Holes. *ArXiv/0605295*, May 2006.
- K. Beckwith, J. F. Hawley, and J. H. Krolik. Transport of Large Scale Poloidal Flux in Black Hole Accretion. *ArXiv e-prints*, June 2009.
- M. C. Begelman. Accreting Black Holes. *ArXiv e-prints*, October 2014.
- M. C. Begelman and P. J. Armitage. A Mechanism for Hysteresis in Black Hole Binary State Transitions. *ApJ*, 782:L18, February 2014. doi: 10.1088/2041-8205/782/2/L18.
- V. S. Beskin, N. L. Zakamska, and H. Sol. Radiation drag effects on magnetically dominated outflows around compact objects. *MNRAS*, 347:587–600, January 2004. doi: 10.1111/j.1365-2966.2004.07229.x.
- R. D. Blandford and D. G. Payne. Hydromagnetic flows from accretion discs and the production of radio jets. *MNRAS*, 199:883–903, June 1982.
- R. D. Blandford and R. L. Znajek. Electromagnetic extraction of energy from Kerr black holes. *MNRAS*, 179:433–456, May 1977.
- J. S. Bloom, D. Giannios, B. D. Metzger, S. B. Cenko, D. A. Perley, N. R. Butler, N. R. Tanvir, A. J. Levan, P. T. O’Brien, L. E. Strubbe, F. De Colle, E. Ramirez-Ruiz, W. H. Lee, S. Nayakshin, E. Quataert, A. R. King, A. Cucchiara, J. Guillochon, G. C. Bower, A. S. Fruchter, A. N. Morgan, and A. J. van der Horst. A Possible Relativistic Jetted Outburst from a Massive Black Hole Fed by a Tidally Disrupted Star. *Science*, 333:203–, July 2011. doi: 10.1126/science.1207150.
- H. Bondi. On spherically symmetrical accretion. *MNRAS*, 112:195, 1952.
- J. R. Buchler and W. R. Yueh. Compton scattering opacities in a partially degenerate electron plasma at high temperatures. *ApJ*, 210:440–446, December 1976. doi: 10.1086/154847.
- J. K. Cannizzo. *The Limit Cycle Instability in Dwarf Nova Accretion Disks*, pages 6–40. World Scientific Publishing Co, 1993. doi: 10.1142/9789814350976_0002.

- S. Chandrasekhar. *Hydrodynamic and hydromagnetic stability*. International Series of Monographs on Physics, Oxford: Clarendon, 1961.
- J.-P. De Villiers and J. F. Hawley. A Numerical Method for General Relativistic Magnetohydrodynamics. *ApJ*, 589:458–480, May 2003. doi: 10.1086/373949.
- J.-P. De Villiers, J. F. Hawley, J. H. Krolik, and S. Hirose. Magnetically Driven Accretion in the Kerr Metric. III. Unbound Outflows. *ApJ*, 620:878–888, February 2005. doi: 10.1086/427142.
- J. Dexter and E. Agol. Quasar Accretion Disks are Strongly Inhomogeneous. *ApJ*, 727:L24, January 2011. doi: 10.1088/2041-8205/727/1/L24.
- J. Dexter and E. Quataert. Inhomogeneous accretion discs and the soft states of black hole X-ray binaries. *MNRAS*, 426:L71–L75, October 2012. doi: 10.1111/j.1745-3933.2012.01328.x.
- J. Dexter, J. C. McKinney, S. Markoff, and A. Tchekhovskoy. Transient jet formation and state transitions from large-scale magnetic reconnection in black hole accretion discs. *MNRAS*, 440:2185–2190, May 2014. doi: 10.1093/mnras/stu581.
- B. T. Draine. *Physics of the Interstellar and Intergalactic Medium*. 2011.
- A. C. Fabian. Cooling Flows in Clusters of Galaxies. *ARA&A*, 32:277–318, 1994. doi: 10.1146/annurev.aa.32.090194.001425.
- A. C. Fabian, R. M. Johnstone, J. S. Sanders, C. J. Conselice, C. S. Crawford, J. S. Gallagher, III, and E. Zweibel. Magnetic support of the optical emission line filaments in NGC 1275. *Nature*, 454:968–970, August 2008. doi: 10.1038/nature07169.
- R. Fender and T. Belloni. GRS 1915+105 and the Disc-Jet Coupling in Accreting Black Hole Systems. *ARA&A*, 42:317–364, September 2004. doi: 10.1146/annurev.astro.42.053102.134031.
- G. B. Field. Thermal Instability. *ApJ*, 142:531, August 1965. doi: 10.1086/148317.
- Jos A. Font. Numerical hydrodynamics and magnetohydrodynamics in general relativity. *Living Reviews in Relativity*, 11(7), 2008. doi: 10.1007/lrr-2008-7. URL <http://www.livingreviews.org/lrr-2008-7>.
- P. C. Fragile, O. M. Blaes, P. Anninos, and J. D. Salmonson. Global General Relativistic Magnetohydrodynamic Simulation of a Tilted Black Hole Accretion Disk. *ApJ*, 668:417–429, October 2007. doi: 10.1086/521092.
- T. Fragos, M. Tremmel, E. Rantsiou, and K. Belczynski. Black Hole Spin-Orbit Misalignment in Galactic X-ray Binaries. *ApJ*, 719:L79–L83, August 2010. doi: 10.1088/2041-8205/719/1/L79.

- C. F. Gammie. Efficiency of Magnetized Thin Accretion Disks in the Kerr Metric. *ApJ*, 522:L57–L60, September 1999. doi: 10.1086/312207.
- C. F. Gammie. The Magnetorotational Instability in the Kerr Metric. *ApJ*, 614: 309–313, October 2004. doi: 10.1086/423443.
- C. F. Gammie, J. C. McKinney, and G. Tóth. HARM: A Numerical Scheme for General Relativistic Magnetohydrodynamics. *ApJ*, 589:444–457, May 2003. doi: 10.1086/374594.
- T. A. Gardiner and J. M. Stone. An unsplit Godunov method for ideal MHD via constrained transport. *Journal of Computational Physics*, 205:509–539, May 2005. doi: 10.1016/j.jcp.2004.11.016.
- A. Harten, P.D. Lax, and B. van Leer. On upstream differencing and godunov-type schemes for hyperbolic conservation laws. *SIAM Rev.*, 25:35–61, 1983.
- J. F. Hawley, C. F. Gammie, and S. A. Balbus. Local Three-dimensional Magnetohydrodynamic Simulations of Accretion Disks. *ApJ*, 440:742, February 1995. doi: 10.1086/175311.
- J. F. Hawley, X. Guan, and J. H. Krolik. Assessing Quantitative Results in Accretion Simulations: From Local to Global. *ApJ*, 738:84, September 2011. doi: 10.1088/0004-637X/738/1/84.
- J. F. Hawley, S. A. Richers, X. Guan, and J. H. Krolik. Testing Convergence for Global Accretion Disks. *ApJ*, 772:102, August 2013. doi: 10.1088/0004-637X/772/2/102.
- I. V. Igumenshchev. Magnetically Arrested Disks and the Origin of Poynting Jets: A Numerical Study. *ApJ*, 677:317–326, April 2008. doi: 10.1086/529025.
- I. V. Igumenshchev. Magnetic Inversion as a Mechanism for the Spectral Transition of Black Hole Binaries. *ApJ*, 702:L72–L76, September 2009. doi: 10.1088/0004-637X/702/1/L72.
- I. V. Igumenshchev, R. Narayan, and M. A. Abramowicz. Three-dimensional Magnetohydrodynamic Simulations of Radiatively Inefficient Accretion Flows. *ApJ*, 592:1042–1059, August 2003. doi: 10.1086/375769.
- K. Inayoshi, Z. Haiman, and J. P. Ostriker. Hyper-Eddington accretion flows on to massive black holes. *MNRAS*, 459:3738–3755, July 2016. doi: 10.1093/mnras/stw836.
- Y.-F. Jiang, J. M. Stone, and S. W. Davis. A Godunov Method for Multidimensional Radiation Magnetohydrodynamics Based on a Variable Eddington Tensor. *ApJS*, 199:14, March 2012. doi: 10.1088/0067-0049/199/1/14.

- Y.-F. Jiang, J. M. Stone, and S. W. Davis. A Global Three-dimensional Radiation Magneto-hydrodynamic Simulation of Super-Eddington Accretion Disks. *ApJ*, 796:106, December 2014. doi: 10.1088/0004-637X/796/2/106.
- R. P. Kerr and A. Schild. Republication of: A new class of vacuum solutions of the Einstein field equations. *General Relativity and Gravitation*, 41:2485–2499, October 2009. doi: 10.1007/s10714-009-0857-z.
- A. King and K. Pounds. Powerful Outflows and Feedback from Active Galactic Nuclei. *ARA&A*, 53:115–154, August 2015. doi: 10.1146/annurev-astro-082214-122316.
- S. S. Komissarov and J. C. McKinney. The ‘Meissner effect’ and the Blandford-Znajek mechanism in conductive black hole magnetospheres. *MNRAS*, 377:L49–L53, May 2007. doi: 10.1111/j.1745-3933.2007.00301.x.
- J. H. Krolik. Magnetized Accretion inside the Marginally Stable Orbit around a Black Hole. *ApJ*, 515:L73–L76, April 1999. doi: 10.1086/311979.
- A. K. Kulkarni, R. F. Penna, R. V. Shcherbakov, J. F. Steiner, R. Narayan, A. Sądowski, Y. Zhu, J. E. McClintock, S. W. Davis, and J. C. McKinney. Measuring black hole spin by the continuum-fitting method: effect of deviations from the Novikov-Thorne disc model. *MNRAS*, 414:1183–1194, June 2011. doi: 10.1111/j.1365-2966.2011.18446.x.
- M. W. Kunz, A. A. Schekochihin, S. C. Cowley, J. J. Binney, and J. S. Sanders. A thermally stable heating mechanism for the intracluster medium: turbulence, magnetic fields and plasma instabilities. *MNRAS*, 410:2446–2457, February 2011. doi: 10.1111/j.1365-2966.2010.17621.x.
- M. W. Kunz, T. Bogdanović, C. S. Reynolds, and J. M. Stone. Buoyancy Instabilities in a Weakly Collisional Intracluster Medium. *ApJ*, 754:122, August 2012. doi: 10.1088/0004-637X/754/2/122.
- P.D. Lax and B. Wendroff. Systems of conservation laws. *Commun. Pure Appl. Math.*, 13:217–237, 1960.
- R.J. LeVeque. *Nonlinear Conservation Laws and Finite Volume Methods*, pages 1–159. Springer, Berlin, Germany, 1998.
- C. D. Levermore. Relating Eddington factors to flux limiters. *J. Quant. Spec. Radiat. Transf.*, 31:149–160, February 1984. doi: 10.1016/0022-4073(84)90112-2.
- R. Lynds. Improved Photographs of the NGC 1275 Phenomenon. *ApJ*, 159, March 1970. doi: 10.1086/180500.
- B. Margon, H. C. Ford, J. I. Katz, K. B. Kwitter, R. K. Ulrich, R. P. S. Stone, and A. Klemola. The bizarre spectrum of SS 433. *ApJ*, 230:L41–L45, May 1979. doi: 10.1086/182958.

- J. E. McClintock, R. Narayan, and J. F. Steiner. Black Hole Spin via Continuum Fitting and the Role of Spin in Powering Transient Jets. *Space Sci. Rev.*, 183: 295–322, September 2014. doi: 10.1007/s11214-013-0003-9.
- J. E. McClintock et al. Measuring the spins of accreting black holes. *Classical and Quantum Gravity*, 28(11):114009, June 2011. doi: 10.1088/0264-9381/28/11/114009.
- M. McCourt, I. J. Parrish, P. Sharma, and E. Quataert. Can conduction induce convection? On the non-linear saturation of buoyancy instabilities in dilute plasmas. *MNRAS*, 413:1295–1310, May 2011. doi: 10.1111/j.1365-2966.2011.18216.x.
- M. McDonald, S. Veilleux, D. S. N. Rupke, and R. Mushotzky. On the Origin of the Extended H α Filaments in Cooling Flow Clusters. *ApJ*, 721:1262–1283, October 2010. doi: 10.1088/0004-637X/721/2/1262.
- M. McDonald, S. Veilleux, D. S. N. Rupke, R. Mushotzky, and C. Reynolds. Star Formation Efficiency in the Cool Cores of Galaxy Clusters. *ApJ*, 734:95, June 2011. doi: 10.1088/0004-637X/734/2/95.
- J. C. McKinney. Total and Jet Blandford-Znajek Power in the Presence of an Accretion Disk. *ApJ*, 630:L5–L8, September 2005. doi: 10.1086/468184.
- J. C. McKinney. General relativistic magnetohydrodynamic simulations of the jet formation and large-scale propagation from black hole accretion systems. *MNRAS*, 368:1561–1582, June 2006. doi: 10.1111/j.1365-2966.2006.10256.x.
- J. C. McKinney and R. D. Blandford. Stability of relativistic jets from rotating, accreting black holes via fully three-dimensional magnetohydrodynamic simulations. *MNRAS*, 394:L126–L130, March 2009. doi: 10.1111/j.1745-3933.2009.00625.x.
- J. C. McKinney and C. F. Gammie. A Measurement of the Electromagnetic Luminosity of a Kerr Black Hole. *ApJ*, 611:977–995, August 2004. doi: 10.1086/422244.
- J. C. McKinney and R. Narayan. Disc-jet coupling in black hole accretion systems - I. General relativistic magnetohydrodynamical models. *MNRAS*, 375:513–530, February 2007. doi: 10.1111/j.1365-2966.2006.11301.x.
- J. C. McKinney, A. Tchekhovskoy, and R. D. Blandford. General relativistic magnetohydrodynamic simulations of magnetically choked accretion flows around black holes. *MNRAS*, 423:3083–3117, July 2012. doi: 10.1111/j.1365-2966.2012.21074.x.
- J. C. McKinney, A. Tchekhovskoy, and R. D. Blandford. Alignment of Magnetized Accretion Disks and Relativistic Jets with Spinning Black Holes. *Science*, 339: 49–, January 2013. doi: 10.1126/science.1230811.
- J. C. McKinney, A. Tchekhovskoy, A. Sadowski, and R. Narayan. Three-dimensional general relativistic radiation magnetohydrodynamical simulation of super-Eddington accretion, using a new code HARMRAD with M1 closure. *MNRAS*, 441:3177–3208, July 2014. doi: 10.1093/mnras/stu762.

- J. C. McKinney, L. Dai, and M. Avara. Efficiency of Super-Eddington Magnetically-Arrested Accretion. *ArXiv/1508.02433*, August 2015a.
- J. C. McKinney, L. Dai, and M. J. Avara. Efficiency of super-Eddington magnetically-arrested accretion. *MNRAS*, 454:L6–L10, November 2015b. doi: 10.1093/mnras/slv115.
- D. L. Meier. The Association of Jet Production with Geometrically Thick Accretion Flows and Black Hole Rotation. *ApJ*, 548:L9–L12, February 2001. doi: 10.1086/318921.
- M. C. Miller and E. J. M. Colbert. Title. 2004. *Int. J. Mod. Phys. and D*13, 1.
- B. Mishra, P. C. Fragile, L. C. Johnson, and W. Kluźniak. Three-dimensional, global, radiative GRMHD simulations of a thermally unstable disc. *MNRAS*, 463:3437–3448, December 2016. doi: 10.1093/mnras/stw2245.
- P. Mocz and X. Guo. Interpreting MAD within multiple accretion regimes. *MNRAS*, 447:1498–1503, February 2015. doi: 10.1093/mnras/stu2555.
- D. Morales Teixeira, P. C. Fragile, V. V. Zhuravlev, and P. B. Ivanov. Conservative GRMHD Simulations of Moderately Thin, Tilted Accretion Disks. *ApJ*, 796:103, December 2014. doi: 10.1088/0004-637X/796/2/103.
- R. Narayan and I. Yi. Advection-dominated accretion: A self-similar solution. *ApJ*, 428:L13–L16, June 1994. doi: 10.1086/187381.
- R. Narayan and I. Yi. Advection-dominated Accretion: Underfed Black Holes and Neutron Stars. *ApJ*, 452:710, October 1995. doi: 10.1086/176343.
- R. Narayan, I. V. Igumenshchev, and M. A. Abramowicz. Magnetically Arrested Disk: an Energetically Efficient Accretion Flow. *PASJ*, 55:L69–L72, December 2003. URL <http://adsabs.harvard.edu/abs/2003PASJ...55L..69N>.
- R. Narayan, A. Sądowski, R. F. Penna, and A. K. Kulkarni. GRMHD simulations of magnetized advection-dominated accretion on a non-spinning black hole: role of outflows. *MNRAS*, 426:3241–3259, November 2012. doi: 10.1111/j.1365-2966.2012.22002.x.
- R. Narayan, Y. Zhu, D. Psaltis, and A. Sądowski. HEROIC: 3D general relativistic radiative post-processor with comptonization for black hole accretion discs. *MNRAS*, 457:608–628, March 2016. doi: 10.1093/mnras/stv2979.
- S. C. Noble, J. H. Krolik, and J. F. Hawley. Direct Calculation of the Radiative Efficiency of an Accretion Disk Around a Black Hole. *ApJ*, 692:411–421, February 2009. doi: 10.1088/0004-637X/692/1/411.
- S. C. Noble, J. H. Krolik, and J. F. Hawley. Dependence of Inner Accretion Disk Stress on Parameters: The Schwarzschild Case. *ApJ*, 711:959–973, March 2010. doi: 10.1088/0004-637X/711/2/959.

- S. C. Noble, J. H. Krolik, J. D. Schnittman, and J. F. Hawley. Radiative Efficiency and Thermal Spectrum of Accretion onto Schwarzschild Black Holes. *ApJ*, 743: 115, December 2011. doi: 10.1088/0004-637X/743/2/115.
- M.L. Norman and K.-H.A. Winkler. Why ultrarelativistic hydrodynamics is difficult. In M.L. Norman and K.-H.A. Winkler, editors, *Astrophysical Radiation Hydrodynamics: Proceedings of the NATO Advanced Workshop held in Garching, August 2-13, 1982*, volume 188 of *NATO ASI Series C*, pages 449–476, Dordrecht, Netherlands, 1986. Reidel.
- I. D. Novikov and K. S. Thorne. Astrophysics of black holes. In C. Dewitt and B. S. Dewitt, editors, *Black Holes (Les Astres Occlus)*, pages 343–450, 1973a.
- I. D. Novikov and K. S. Thorne. *In Black Holes-Les Astres Occlus, ed. C. De Witt & B. S. De Witt*. New York: Gordon & Breach, 1973b. URL <http://adsabs.harvard.edu/abs/1973blho.conf..343N>.
- K. Ohsuga and S. Mineshige. Global Structure of Three Distinct Accretion Flows and Outflows around Black Holes from Two-dimensional Radiation-magnetohydrodynamic Simulations. *ApJ*, 736:2, July 2011. doi: 10.1088/0004-637X/736/1/2.
- K. Ohsuga, M. Mori, T. Nakamoto, and S. Mineshige. Supercritical Accretion Flows around Black Holes: Two-dimensional, Radiation Pressure-dominated Disks with Photon Trapping. *ApJ*, 628:368–381, July 2005. doi: 10.1086/430728.
- J. C. B. Papaloizou and J. E. Pringle. The time-dependence of non-planar accretion discs. *MNRAS*, 202:1181–1194, March 1983. doi: 10.1093/mnras/202.4.1181.
- I. J. Parrish and E. Quataert. Nonlinear Simulations of the Heat-Flux-driven Buoyancy Instability and Its Implications for Galaxy Clusters. *ApJ*, 677:L9, April 2008. doi: 10.1086/587937.
- I. J. Parrish, E. Quataert, and P. Sharma. Turbulence in Galaxy Cluster Cores: A Key To Cluster Bimodality? *ApJ*, 712:L194–L198, April 2010. doi: 10.1088/2041-8205/712/2/L194.
- I. J. Parrish, M. McCourt, E. Quataert, and P. Sharma. The effects of anisotropic viscosity on turbulence and heat transport in the intracluster medium. *MNRAS*, 422:704–718, May 2012. doi: 10.1111/j.1365-2966.2012.20650.x.
- R. F. Penna, J. C. McKinney, R. Narayan, A. Tchekhovskoy, R. Shafee, and J. E. McClintock. Simulations of magnetized discs around black holes: effects of black hole spin, disc thickness and magnetic field geometry. *MNRAS*, 408:752–782, October 2010a. doi: 10.1111/j.1365-2966.2010.17170.x.
- R. F. Penna, J. C. McKinney, R. Narayan, A. Tchekhovskoy, R. Shafee, and J. E. McClintock. Simulations of magnetized discs around black holes: effects of black

- hole spin, disc thickness and magnetic field geometry. *MNRAS*, 408:752–782, October 2010b. doi: 10.1111/j.1365-2966.2010.17170.x.
- R. F. Penna, A. Sądowski, and J. C. McKinney. Thin-disc theory with a non-zero-torque boundary condition and comparisons with simulations. *MNRAS*, 420: 684–698, February 2012. doi: 10.1111/j.1365-2966.2011.20084.x.
- M. E. Pessah, C.-k. Chan, and D. Psaltis. Angular Momentum Transport in Accretion Disks: Scaling Laws in MRI-driven Turbulence. *ApJ*, 668:L51–L54, October 2007. doi: 10.1086/522585.
- T. Piran, A. Sądowski, and A. Tchekhovskoy. Jet and disc luminosities in tidal disruption events. *MNRAS*, 453:157–165, October 2015. doi: 10.1093/mnras/stv1547.
- P. Polko and J. C. McKinney. Electromagnetic vs. Lense-Thirring alignment of black hole accretion discs. *ArXiv e-prints*, December 2015.
- E. Quataert. Buoyancy Instabilities in Weakly Magnetized Low-Collisionality Plasmas. *ApJ*, 673:758–762, February 2008. doi: 10.1086/525248.
- R. A. Remillard and J. E. McClintock. X-Ray Properties of Black-Hole Binaries. *ARA&A*, 44:49–92, September 2006. doi: 10.1146/annurev.astro.44.051905.092532.
- C. S. Reynolds et al. Trapping of Magnetic Flux by the Plunge Region of a Black Hole Accretion Disk. *ApJ*, 651:1023–1030, November 2006. doi: 10.1086/507691.
- D. M. Rothstein and R. V. E. Lovelace. Advection of Magnetic Fields in Accretion Disks: Not So Difficult After All. *ApJ*, 677:1221–1232, April 2008. doi: 10.1086/529128.
- D. M. Russell, J. C. A. Miller-Jones, T. J. Maccarone, et al. Testing the Jet Quenching Paradigm with an Ultradeep Observation of a Steadily Soft State Black Hole. *ApJ*, 739:L19, September 2011. doi: 10.1088/2041-8205/739/1/L19.
- M. Ruszkowski, H.-Y. K. Yang, and E. Zweibel. Global simulations of galactic winds including cosmic ray streaming. *ArXiv e-prints*, February 2016.
- G. B. Rybicki and A. P. Lightman. *Radiative Processes in Astrophysics*. June 1986.
- A. Sądowski and R. Narayan. Powerful radiative jets in super-critical accretion disks around non-spinning black holes. *arxiv: 1503.00654*, March 2015.
- Y. Sakurai, K. Inayoshi, and Z. Haiman. Hyper-Eddington mass accretion on to a black hole with super-Eddington luminosity. *MNRAS*, 461:4496–4504, October 2016. doi: 10.1093/mnras/stw1652.

- G. Salvesen, J. B. Simon, P. J. Armitage, and M. C. Begelman. Accretion disc dynamo activity in local simulations spanning weak-to-strong net vertical magnetic flux regimes. *MNRAS*, 457:857–874, March 2016. doi: 10.1093/mnras/stw029.
- A. Sądowski, R. Narayan, J. C. McKinney, and A. Tchekhovskoy. Numerical simulations of super-critical black hole accretion flows in general relativity. *MNRAS*, 439:503–520, March 2014. doi: 10.1093/mnras/stt2479.
- A. Sądowski, R. Narayan, A. Tchekhovskoy, D. Abarca, Y. Zhu, and J. C. McKinney. Global simulations of axisymmetric radiative black hole accretion discs in general relativity with a mean-field magnetic dynamo. *MNRAS*, 447:49–71, February 2015. doi: 10.1093/mnras/stu2387.
- A. Sądowski, J.-P. Lasota, and R. Abramowicz, M. A. and Narayan. Energy flows in thick accretion discs and their consequences for black hole feedback. *MNRAS*, 456:3915–3928, March 2016. doi: 10.1093/mnras/stv2854.
- K. Schwarzschild. ber das Gravitationsfeld eines Massenpunktes nach der Einsteinschen Theorie. *Sitzungsberichte der Kniglich Preussischen Akademie der Wissenschaften*, 1:189–196, 1916.
- C. K. Seyfert. Nuclear Emission in Spiral Nebulae. *ApJ*, 97:28, January 1943. doi: 10.1086/144488.
- R. Shafee, J. C. McKinney, R. Narayan, A. Tchekhovskoy, C. F. Gammie, and J. E. McClintock. Three-Dimensional Simulations of Magnetized Thin Accretion Disks around Black Holes: Stress in the Plunging Region. *ApJ*, 687:L25–L28, November 2008. doi: 10.1086/593148.
- N. I. Shakura and R. A. Sunyaev. Black holes in binary systems. Observational appearance. *A&A*, 24:337–355, 1973. URL <http://adsabs.harvard.edu/abs/1973A%26A...24..337S>.
- S. L. Shapiro. Spin, Accretion, and the Cosmological Growth of Supermassive Black Holes. *ApJ*, 620:59–68, February 2005. doi: 10.1086/427065.
- P. Sharma and G. W. Hammett. Preserving monotonicity in anisotropic diffusion. *Journal of Computational Physics*, 227:123–142, November 2007. doi: 10.1016/j.jcp.2007.07.026.
- P. Sharma, B. D. G. Chandran, E. Quataert, and I. J. Parrish. Buoyancy Instabilities in Galaxy Clusters: Convection Due to Adiabatic Cosmic Rays and Anisotropic Thermal Conduction. *ApJ*, 699:348–361, July 2009. doi: 10.1088/0004-637X/699/1/348.
- K. Shibata and Y. Uchida. A magnetodynamic mechanism for the formation of astrophysical jets. I - Dynamical effects of the relaxation of nonlinear magnetic twists. *PASJ*, 37:31–46, 1985.

- K. Shibata and Y. Uchida. A magnetodynamic mechanism for the formation of astrophysical jets. II - Dynamical processes in the accretion of magnetized mass in rotation. *PASJ*, 38:631–660, 1986.
- H. Shiokawa, J. C. Dolence, C. F. Gammie, and S. C. Noble. Global General Relativistic Magnetohydrodynamic Simulations of Black Hole Accretion Flows: A Convergence Study. *ApJ*, 744:187, January 2012. doi: 10.1088/0004-637X/744/2/187.
- F. H. Shu. *The physics of astrophysics. Volume 1: Radiation*. 1991.
- A. Soltan. Masses of quasars. *MNRAS*, 200:115–122, July 1982.
- K. A. Sorathia, C. S. Reynolds, and P. J. Armitage. Connections Between Local and Global Turbulence in Accretion Disks. *ApJ*, 712:1241–1247, April 2010. doi: 10.1088/0004-637X/712/2/1241.
- K. A. Sorathia, C. S. Reynolds, J. M. Stone, and K. Beckwith. Global Simulations of Accretion Disks. I. Convergence and Comparisons with Local Models. *ApJ*, 749:189, April 2012. doi: 10.1088/0004-637X/749/2/189.
- L. Spitzer. *Physics of Fully Ionized Gases*. 1962.
- J. M. Stone and M. L. Norman. ZEUS-2D: A radiation magnetohydrodynamics code for astrophysical flows in two space dimensions. I - The hydrodynamic algorithms and tests. *ApJS*, 80:753–790, June 1992.
- J. M. Stone, J. F. Hawley, C. F. Gammie, and S. A. Balbus. Three-dimensional Magnetohydrodynamical Simulations of Vertically Stratified Accretion Disks. *ApJ*, 463:656, June 1996. doi: 10.1086/177280.
- J. M. Stone, T. A. Gardiner, P. Teuben, J. F. Hawley, and J. B. Simon. Athena: A New Code for Astrophysical MHD. *ApJS*, 178:137–177, September 2008. doi: 10.1086/588755.
- H. R. Takahashi and K. Ohsuga. Radiation drag effects in black hole outflows from super-critical accretion disks via special relativistic radiation magnetohydrodynamics simulations. *PASJ*, February 2015. doi: 10.1093/pasj/psu145.
- S. Takeuchi, K. Ohsuga, and S. Mineshige. A Novel Jet Model: Magnetically Collimated, Radiation-Pressure Driven Jet. *PASJ*, 62:L43, October 2010.
- A. Tchekhovskoy. Launching of Active Galactic Nuclei Jets. In I. Contopoulos, D. Gabuzda, and N. Kylafis, editors, *The Formation and Disruption of Black Hole Jets*, volume 414 of *Astrophysics and Space Science Library*, page 45, 2015. doi: 10.1007/978-3-319-10356-3_3.
- A. Tchekhovskoy and J. C. McKinney. Prograde and retrograde black holes: whose jet is more powerful? *MNRAS*, 423:L55–L59, June 2012. doi: 10.1111/j.1745-3933.2012.01256.x.

- A. Tchekhovskoy, R. Narayan, and J. C. McKinney. Efficient generation of jets from magnetically arrested accretion on a rapidly spinning black hole. *MNRAS*, 418:L79–L83, November 2011. doi: 10.1111/j.1745-3933.2011.01147.x.
- A. Tchekhovskoy, J. C. McKinney, and R. Narayan. General Relativistic Modeling of Magnetized Jets from Accreting Black Holes. *Journal of Physics Conference Series*, 372(1):012040, July 2012. doi: 10.1088/1742-6596/372/1/012040.
- A. Tchekhovskoy, B. D. Metzger, D. Giannios, and L. Z. Kelley. Swift J1644+57 gone MAD: the case for dynamically important magnetic flux threading the black hole in a jetted tidal disruption event. *MNRAS*, 437:2744–2760, January 2014. doi: 10.1093/mnras/stt2085.
- R. Teyssier. Grid-Based Hydrodynamics in Astrophysical Fluid Flows. *ARA&A*, 53:325–364, August 2015. doi: 10.1146/annurev-astro-082214-122309.
- F. Tombesi, M. Meléndez, S. Veilleux, J. N. Reeves, E. González-Alfonso, and C. S. Reynolds. Wind from the black-hole accretion disk driving a molecular outflow in an active galaxy. *Nature*, 519:436–438, March 2015. doi: 10.1038/nature14261.
- E. P. Velikhov. Stability of an ideally conducting liquid flowing between rotating cylinders in a magnetic field. *J. Exper. Theor. Phys.*, 36:1398–1404, 1959.
- K. Watarai, T. Mizuno, and S. Mineshige. Title. *ApJ*, 549, 2001. L77–L77.
- J. R. Wilson. Magnetohydrodynamics near a black hole. In R. Ruffini, editor, *1st Marcel Grossmann Meeting on General Relativity*, pages 393–413, 1977.
- L. Woltjer. Emission Nuclei in Galaxies. *ApJ*, 130:38, July 1959. doi: 10.1086/146694.
- H.-Y. K. Yang and C. S. Reynolds. How AGN Jets Heat the Intracluster Medium - Insights from Hydrodynamic Simulations. *ApJ*, 829:90, October 2016. doi: 10.3847/0004-637X/829/2/90.
- N. L. Zakamska and R. Narayan. Models of Galaxy Clusters with Thermal Conduction. *ApJ*, 582:162–169, January 2003. doi: 10.1086/344641.
- M. Zamaninasab, E. Clausen-Brown, T. Savolainen, and A. Tchekhovskoy. Dynamically important magnetic fields near accreting supermassive black holes. *Nature*, 510:126–128, June 2014. doi: 10.1038/nature13399.
- Ya. B. Zeldovich. The Fate of a Star and the Evolution of Gravitational Energy upon Accretion. *Soviet Physics Doklady*, 9:195, 1964.
- Y. Zhu, S. W. Davis, R. Narayan, A. K. Kulkarni, R. F. Penna, and J. E. McClintock. The eye of the storm: light from the inner plunging region of black hole accretion discs. *MNRAS*, 424:2504–2521, August 2012. doi: 10.1111/j.1365-2966.2012.21181.x.

Y. Zhu, R. Narayan, A. Sadowski, and D. Psaltis. HERO - A 3D general relativistic radiative post-processor for accretion discs around black holes. *MNRAS*, 451: 1661–1681, August 2015. doi: 10.1093/mnras/stv1046.